



Department of Electronics and Telecommunications

Master Thesis

Experimental Setup for Inductive and Capacitive Characterization of Colloids featuring Pyroelectric and Ferromagnetic Effects

Supervisor:

Prof. Carlo Ricciardi

Tutor:

Prof. Alessandro Chiolerio

Co-Tutor:

Erik Garofalo

Author:

Matteo Bevione



December 2019

Contents

1	Introduction	3
1.1	Earth Change and Global Effects	4
1.2	A world of Energy	10
1.3	Waste Heat Recovery: Toward a Cleaner World	11
1.4	Ferrofluid	13
2	Physical Basis	17
2.1	Thermodynamic Effects	17
2.1.1	Fundamentals	17
2.1.2	Thermodynamic Potentials	20
2.1.3	Material Properties	22
2.1.4	Thermodiffusion in Ferrofluids: Soret Effect	24
2.1.5	Pyroelectric Effect	28
2.2	Magnetic Effects	32
2.2.1	Magnetism	32
2.2.2	Magnetization	34
2.2.3	Magnetic Force	41
2.2.4	Magnetophoresis	44
2.3	Thermal and Magnetic Influence on Physical Properties	46
2.3.1	Stability Requirements	46
2.3.2	Thermal Conductivity	49
2.3.3	Surface Tension	50
2.4	Thermomagnetic Convection	52
3	Governing Equations	55
3.1	Continuity Equation for Mixture	56
3.2	Momentum equation for the mixture	57
3.3	Volume Fraction Equation for Particles	59
3.3.1	Buoyancy and Froude–Krylov force	61
3.3.2	Drag Forces	62
3.3.3	Unsteady forces	63
3.4	Energy Equation For Mixture	65
4	Experimental Setup	67

4.1	Prototypes	67
4.1.1	CERES 1.0	68
4.1.2	CERES 2.0	69
4.1.3	Chamber for Tests	69
4.2	Peltier Modules	72
4.3	Magnets	74
4.4	Sonicator	75
4.5	Apparatus	76
5	Results And Discussion	81
5.1	Circuit Analysis	81
5.2	Current and Voltage Measurements	87
5.2.1	Pyroelectric Coefficient Evaluation	95
5.3	Generated Power	104
6	Conclusions	111

List of Figures

1	Trend of CO ₂ level in atmosphere during history.	4
2	Trend of CO ₂ level in atmosphere in recent years.	5
3	Mean level of methane and nitrous oxide concentration per year.	7
4	Global Warming Power of some important GHG in term of the reference value of CO ₂	7
5	Temperature Trend since 1880.	8
6	Extension of Artic Sea since 1979.	8
7	Antarctica and Greenland mass trend.	9
8	Sea level increase due to melting glaciers.	9
9	Global energy consumption trend during the last 140 years.	10
10	Schematic representation of the nano-particle structure after the coating.	14
11	Heckmann diagram.	29
12	Scheme of pyroelectric effect working principle.	29
13	Temperature dependence of Langevin's function for different kinds of FFs.	36
14	Comparison among Langevin's and modified mean field model.	39
15	Magnetization curve obtained at different ferrofluid concentrations.	40
16	Comparison among the kelvin (Eq. 69) and the modified (Eq. 71) forces with the experimental data.	43
17	Thermal conductivity as a function of magnetic field.	49
18	Thermo-magnetic driving mechanism.	53
19	C.E.R.E.S. system prototype 1.0.	68
20	Second prototype of C.E.R.E.S. system (2.0).	70
21	Schematic representation of a Perovskite structure of the form ABX ₃	71
22	Cell for visual observation of thermo-magnetic motion and pyro/tribo-electric characterization of colloidal mixture.	71
23	Peltier modulus with dimensions 15 × 30 × 3 mm	73
24	Aluminium (Al), Nickel (Ni), Cobalt (Co) alloy (ALNICO) permanent magnet with dimension 15 × 30 × 3mm.	74
25	Cup horn sonicator (CHS) schematic representation.	75

26	Schematic representation of the experimental apparatus obtained by ©SolidWorks.	76
27	Peristaltic pump needed to force the fluid motion.	77
28	Digital magnetic stirrer with thermal plate.	77
29	Electrode in the tube fixed with hot glue to avoid motion and fluid losses.	78
30	Measurements systems for inductive and capacitive analysis.	78
31	Picture of the real experimental setup created in laboratory.	79
32	Scheme of the magnet position in the real apparatus	79
33	Magnetic field distribution measured by the gaussmeter and plotted with ©MATLAB.	80
34	Titanium electrodes impedance modulus in air conditions as a function of frequency.	82
35	Equivalent circuit of the titanium electrodes.	82
36	Bode plot of titanium electrodes coming from the impedance measurements performed with LCR-meter.	83
37	Coil of wire impedance modulus in air conditions as a function of frequency.	84
38	Bode plot of coil used for electromotive force harvesting.	84
39	Equivalent circuit of the coil of wire.	86
40	Baseline of the figure of merit acquired with only kerosene filling the system.	88
41	Trend of the figure of merits of the system filled with only kerosene at different flowing rates. The baseline acquired in no motion condition has been subtracted to the data.	89
42	Baseline of the figure of merit acquired with ferrofluid at 2% of magnetite concentration filling the system.	90
43	Trend of the figure of merits of the system filled with ferrofluid, having 2% of volume concentration of magnetite, at different flow rates.	90
44	Trend of the figures of merit of the system filled with ferrofluid, having 2%vol of volume concentration of magnetite and 0.5%vol of barium titanate, at different flowing rates.	93

45	Trend of the figure of merits of the system filled with ferrofluid, having 2%vol of volume concentration of magnetite and 0.5%vol of barium titanate, heated up to 60°C at different flowing rates.	93
46	Power output computed for the different fluid fluxed in the system.	94
47	Scheme of the experimental apparatus under analysis with quotes obtained by ®SolidWorks	96
48	Particle deformation during the contact with the electrode. . .	98
49	Barium Titanate pyroelectric coefficient as a function of temperature.	101
50	Bode plot of titanium electrodes, used for electrostatic charge recovery, figure of merits. The legend report the pump rate velocity for each curve.	104
51	Detail of Fig. 50. The image is zoomed in order to appreciate the differences among the curves obtained for different pump rates.	105
52	Resistance and Reactance plot of titanium electrodes with hot fluid flowing at different rates	106
53	Detail of Fig. 52. The image is zoomed in order to appreciate the differences among the curves obtained for different pump rates.	107
54	Bode plot of inductive coil of wire as a function of different flow velocity. The legend reports the pump rate for each curve.	108
55	Detail of Fig. 54. The image is zoomed in order to appreciate the differences among the curves obtained for different pump rates.	108
56	Bode plot of inductive coil of wire as a function of different flow velocity. The legend reports the pump rate for each curve.	109
57	Detail of Fig. 56. The image is zoomed in order to appreciate the differences among the curves obtained for different pump rates when the fluid is heated up to $T = 60^{\circ}\text{C}$	110

List of Tables

1	Main properties of the ferrofluids employed.	15
2	Soret coefficient for maghemite uncoated nano-particles as a function of pH.	26
3	Soret coefficient for maghemite nano-particles as a function of pH.	26
4	Static magnetic Hamaker constant calculated for the most used materials, suspended in different fluids.	48
5	Dimensions of CERES prototype 1.0.	69
6	Temperatures of Becher, first and second electrodes with only stirrer as heating source.	92
7	Temperatures of Becher, first and second electrodes with stirrer and heating plate as heating sources.	92
8	Mean values of current and voltage obtained by fit operator in MATLAB software. The errors have been computed using the standard deviation method.	94
9	Primary Pyroelectric coefficients calculated when the magnetic stirrer is the only heating source (label <i>c</i>) and also when the sample is heated at 60°C (label <i>h</i>)	100
10	Resistance and Capacitance at different flow rate velocities of the capacitive titanium electrodes.	105
11	Resistance and Capacitance at different flow rate velocities of the capacitive titanium electrodes. The measurements are performed fluxing the fluid at $T = 60^{\circ}\text{C}$	107
12	Resistance and Capacitance at different flow rate velocities of the coil of wires. The measurements are performed fluxing the fluid at RT.	109
13	Resistance and Capacitance at different flow rate velocities of the inductive coil. The measurements are performed fluxing the fluid at $T = 60^{\circ}\text{C}$	110

Acronyms

BT Barium Titanate.

FF Ferrofluid.

FoM Figure of Merit.

GHG GreenHouse Gases.

GISS Goddard Institute for Space Studies.

GWP Global Warming Potential.

HG High Grade.

IFF Ionic Ferrofluid.

IPCC Intergovernmental Panel on Climate Change.

LG Low Grade.

MG Medium Grade.

NCEI National Centers for Environmental Information.

NOAA National Oceanic and Atmospheric Administration.

NP Nano-Particles.

PE PyroElectric.

SFF Surfacted Ferrofluid.

WH Waste Heat.

Abstract

Since the beginning of the industrial revolution the human contribution to pollution has played an important role. Even though carbon dioxide is neither the 'worst' nor the most abundant greenhouse gas, it is always kept under control because of its long lifetime in atmosphere and, according to the national center for environment information, its level is nowadays the highest never observed in history. Its increase provokes an increase in temperature with dangerous consequences in many field like agriculture. Moreover, this phenomenon is worsened by the increasing world power consumption which, being the renewable sources not able to satisfy the entire requirement, force to produce more energy and thus more pollutants in the air. To solve this issue, the efficiency of energy production, storage, transport and delivery processes needs to be enhanced. In order to do that, the energy wasted and introduced in the environment can be recovered and used to produce reusable energy. This field is called energy recovery or, when the energy is wasted under the form of heat, waste heat recovery. The aim is to store the heat produced during a process and to convert it in useful energy enhancing the performance of the system. Several solid-state devices have already been proposed for the high grade and medium grade wasted heat particularly in industrial and automotive application where the gas are emitted at high temperature. However, since these devices have low performances when used to recover low temperature or low grade waste heat, the C.E.R.E.S. system has been proposed. This is not a solid-state device since uses a magnetic colloid, moving under the action of the magnetic and thermal field coupling, to generate electromotive force and extract power. In previous works of thesis, the performances of this device have been investigated and here, I present a method to introduce pyroelectricity in the system in order to enhance its performances. In fact, the reasoning is to used many different physical effects to extract the largest amount of power. For this goal, a mixture of barium titanate and ferrofluid has been created and characterized to observe the contribution to current and voltage production brought by the introduction of barium titanate. Finally, the cell that will be used to perform visual observation of the thermomagnetic motion and more reliable measurements on this mixture has been designed. This will also allow to investigate different magnets and thermal gradient configuration to find the best coupling.

1 Introduction

In the first part of this thesis, I present some data collected from different agency monitoring the climate change and its consequences. This will show the importance of such phenomenon and the need to reduce the always larger energy production coming from polluting sources. In particular, the attention will be focused on the possibility to recover the waste heat (WH) and to use it in order to produce further energy reducing the heat introduced in atmosphere. This field has been already investigated in the last decades and many solution have been proposed to recover the so called *high* grade (HG) or *medium* grade (MG) WH especially in industrial applications. However, no reliable solution is present concerning the low grade (LG) waste heat. Its importance lies in the fact that the largest amount of heat belong to this category since $\approx 60\%$ of the overall WH belong to this category. This summed to the fact that solid state devices developed in industrial or automotive applications are not able to provide good efficiency for LG harvesting, have pushed to investigate other possibilities, like liquid devices. Here, a reactor using a magnetic fluid, i.e. ferrofluid (FF), has been created to provide a solution to this issue.

In the second part, the physical phenomena occurring in FF when subjected to a temperature gradient coupled with a magnetic field are investigated. Moreover, its thermodynamic and magnetic properties are shown in detail in order to provide an overview on their link and mutual influence. Furthermore, a description of the pyroelectric effect is provided since the aim is to introduce this effect in the working principle of the system to improve its energy production.

Successively, the prototypes of the reactors designed for LGWH harvesting and the study of these phenomena are reported. These have been studied and simulated in previous work of thesis [1, 2] where the possibility to enhance the system efficiency resulted evident. Thus, a new experimental setup to study the contribution of pyroelectric effect (PE) on the energy recovered is proposed (see subsection 4.5) as well as a new colloidal mixture formed by ferrofluid and barium titanate (BT).

Finally, the results obtained from this apparatus have been reported and discussed to effectively verify the contribution to current generation by BT.

1.1 Earth Change and Global Effects

At the beginning of 19th century the first industrial revolution provoked the passage from hand production methods to machines. From then on, the processes automation has played an increasingly important role in industry and agriculture, but also in everyday life where the comfort and velocity have become fundamental requirements. To accomplish this, new forms of energy have been developed and their production, extraction, transformation and distribution have brought many climate issues. This topic is well-known nowadays and has been analyzed under so many points of view and by so many different people that a bit of confusion results in today's public opinion. The evidence of this fact is in the declaration made by figures like the president of United States of America, Donald Trump, who arrived to deny even the existence of such phenomenon (video of his conference is present on YouTube and many newspapers have reported it) or also by the so-called climate change deniers which argue that the rising of global temperatures has stopped in the last decade and that the temperature variation is just a cyclic phenomenon.

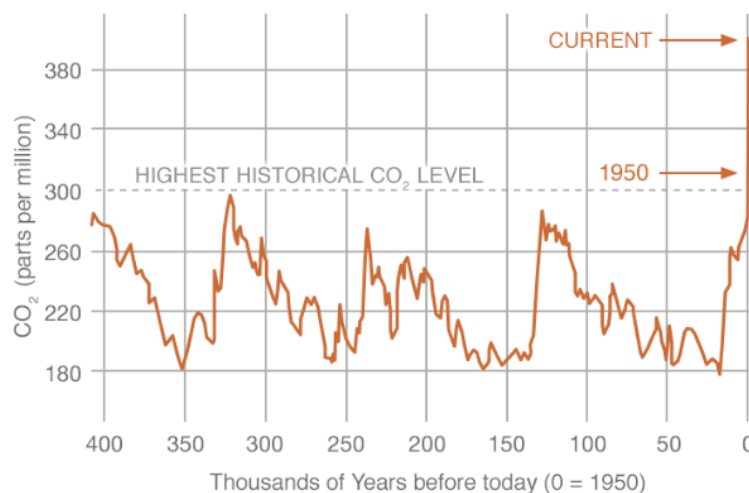


Figure 1: Trend of CO₂ level in atmosphere. The data are public and come from coring. This graph has been obtained from the data published on NOAA NCEI Paleoclimatology Program website from [3].

However, these claims have been refused in many articles like [4] published on the Science journal in 2015, where the monotonic increase of temperatures is evident. Moreover, one of the “proofs” brought by them to sustain their theory, regards the fact that CO₂ level varies in a cyclical fashion, thus the increase we are registering in this period is nothing but a fluctuation which will reenter in next years, but this statement is only partially true. In fact, as we can see from Fig. 1, which represents

the data of EPICA Dome C provided by NOAA NCEI Paleoclimatology Program, the cyclical variation is not indicative of the climate changing since it is due to the alternance of glacial and interglacial period and, by similarity with previous cycles, it can be noticed that a decrease should be occurring in these years, which is in contrast with the data collected since the beginning of the industrial revolution. A further indicator of the human activity influence and the consequent climatic issues is the CO₂ level, which have never been so high: in 2019 the average level lied around ≈ 415 ppm, i.e. more than 100ppm above the previous highest level never registered. The recent trend is shown in detail in Fig. 2 provided by NASA.[5] Nevertheless, every climatologist knows that carbon dioxide is not the only driver of climate changes, even if it is the main indicator of the climate issues, as we will see later.

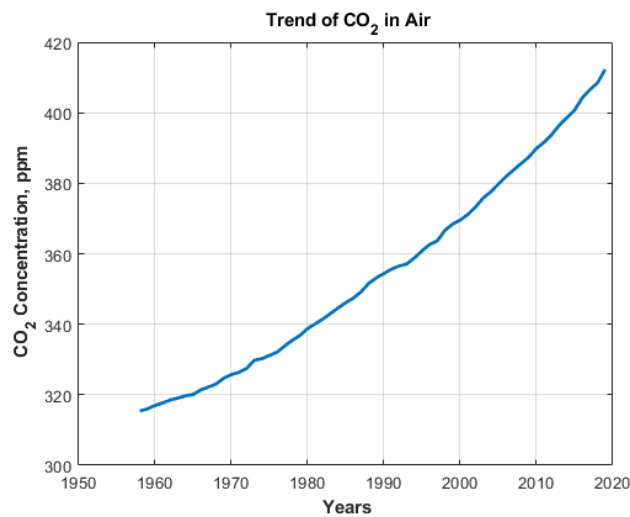


Figure 2: Trend of CO₂ level in atmosphere in recent years. The data are published and provided by NOAA ESRL[6].

These are just two examples of the ignorance and confusion about climate change which is not only real but perceptible and evident in many fields like agriculture, where the temperature rise is reducing quality and yield of productions because of, e.g, increasing rainfalls, or forest fires, which are more frequent recently.[7, 8] The gravity of the situation has pushed, above all, the new generations to mobilize in awareness campaigns and research to find new technologies and methods to reduce the amount of pollutants. In order to clarify the actual climate situation, some data collected by several institutes will be summarized here, mainly those provided by NASA's Goddard Institute for Space Studies (GISS)[9]. The first parameter typically analyzed when dealing with global warming regard the amount of pollutants in the air, which provoke the so-called greenhouse effect. Focusing on the main greenhouse

gases (GHG) and listing them in order of importance, according to Intergovernmental Panel on Climate Change (IPCC) [10, 11, 12] there are:

- **Water Vapour:** it is the major contributor among all since it provokes [13, 14] from ≈ 30 to 70% of the overall greenhouse effect. The reason of its power is not intrinsic of the water capability to retain heat but to the large amount present in the atmosphere. To better explain why the water plays such a fundamental role, assume that the increase of carbon dioxide level provokes the temperature rise of 1°C . Consequently, the presence of water vapor in atmosphere increases and a further rise in temperature verifies which again increase the presence of H_2O molecules. This loop is called *positive feedback loop*;
- **Carbon Dioxide:** it is the most famous and the principal gas monitored because, even if it absorbs less heat per molecule than others, it's more abundant and has longer lifetime in air (thousands of years with respect to the tens of methane). Furthermore, it plays an important role in pH of the oceans, since these represent the main CO_2 "container", and its increase provokes acidification. Moreover, the same positive feedback encountered before can be found here. In fact, a temperature increase provokes the oceans to release CO_2 in atmosphere because a decreasing in solubility. This gas occurs naturally in the atmosphere, but human activity, particularly through the burning of fossil fuels, contributes to its concentration inflation in the atmosphere; [15, 16]
- **Methane:** it is produced typically by natural processes but also from man-made ones. The impact of this gas on greenhouse effect is ≈ 60 times the one of CO_2 and a monotonic increase in the last decades has been registered, as can be observed in the Fig. 3a. However, its level and lifetime are low enough to make its contribution still under control;
- **Nitrous Oxide:** its capability to absorb heat is ≈ 300 times the CO_2 one and around 40% of total N_2O emissions are caused by human activity. Moreover, its lifetime in atmosphere is above 110 years making it one of the most persistent GHG. Luckily, it is rare in atmosphere but $\approx 6\%$ of GH emission in 2017 was N_2O and, due to its high permanence, the amount will rapidly increase in time [17]. Its trend is reported in Fig. 3b;
- **Ozone:** it's one of the most known due to the problem of the ozone hole. It is naturally present in the upper level of the atmosphere and, in contrast with the previously analyzed gases, it absorbs mainly the radiations coming from the sun instead of the ones reflected by the Earth surface.

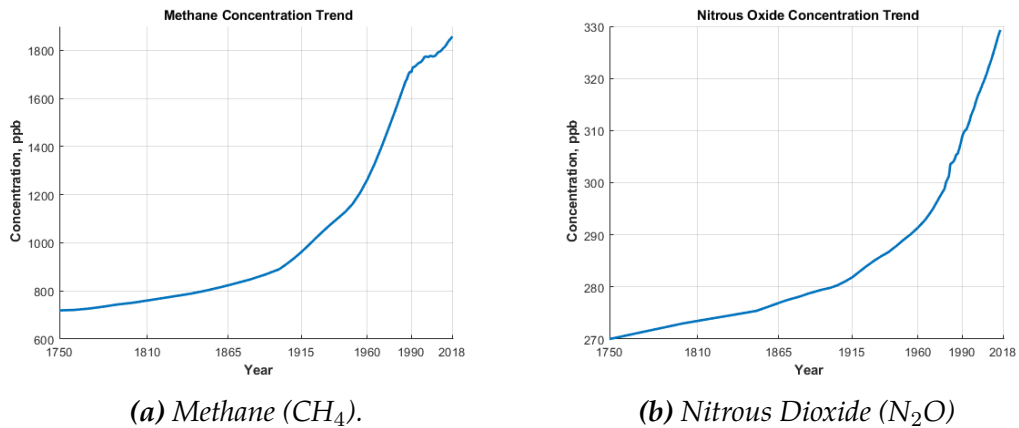


Figure 3: Mean level of methane and nitrous oxide concentration per year, given in part per billions (ppb). The data have been published by European Environment Agency (EEA) National Oceanic and Atmospheric Administration (NOAA)[18, 19].

In order to give an idea of the global warming potential (GWP) factors of the different gases, i.e. a measure of how much heat is retained by each gas compared to CO_2 , the data provided by IPCC [20] calculated in a time period of 100 years are reported in Fig. 4. The consequence of these trends an overall increase in the average temperature

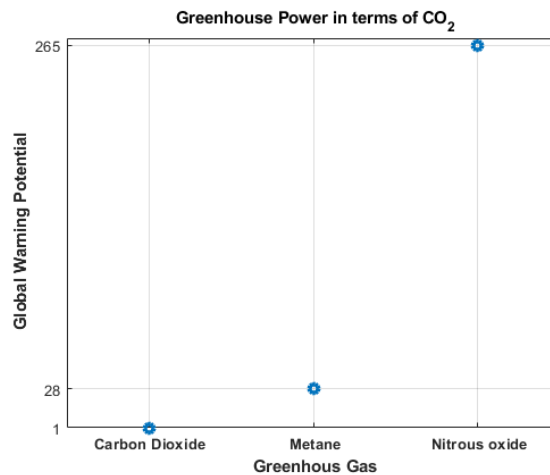


Figure 4: Global Warming Power of some important GHG in term of the reference value of CO_2 . The data are provided by IPCC[20].

since the 1880 is occurring, as can be noticed from Fig. 5 where, taking as reference the 1951-1980 period, the trend before and after the third industrial revolution is presented.

This is not the only worrying factor but a further idea of the importance of these phenomena are given by:

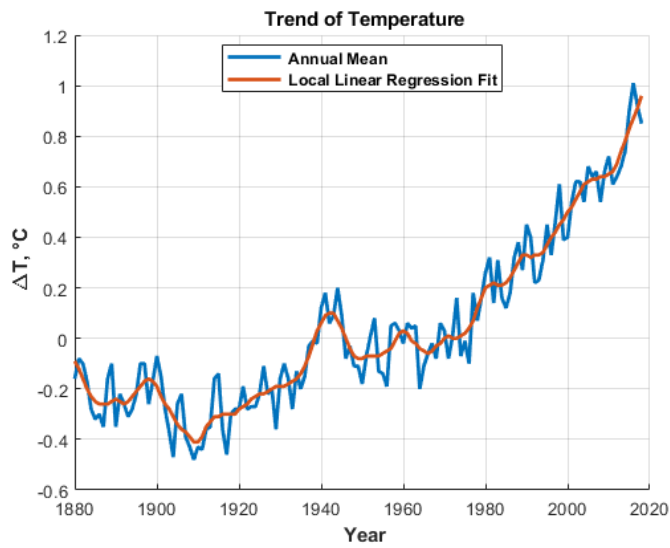


Figure 5: This graph has been extracted from data provided by NASA/GISS. It has to be noticed that the year 2016 has been registered as the warmest in last two centuries.[9]

1. The observation of Arctic sea ice, whose extension (area) is now declining at a rate of 12.85% per decade. In Fig. 6 is reported a graph representing the ice extent for each September since 1979 where 2012 has represented the absolute minimum.

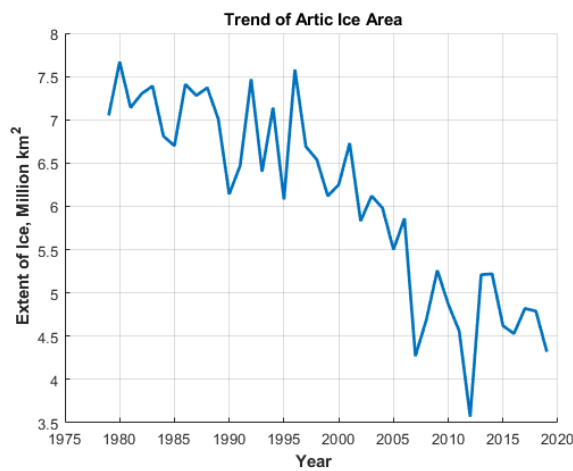


Figure 6: Extension of Artic Sea since 1979. The data have been extracted from NASA website[5]

2. The observation of Antarctica and Greenland mass variation since 2002 from NASA's GRACE satellites shown in Fig. 7 where a reduction (indicated with black arrows on the picture) of 127 and 286 gigatonnes per year, respectively, is shown. It has to be noticed that data arrive only until 2017 when the GRACE

mission concluded science operations. To have further information about the data generation refer to [21]

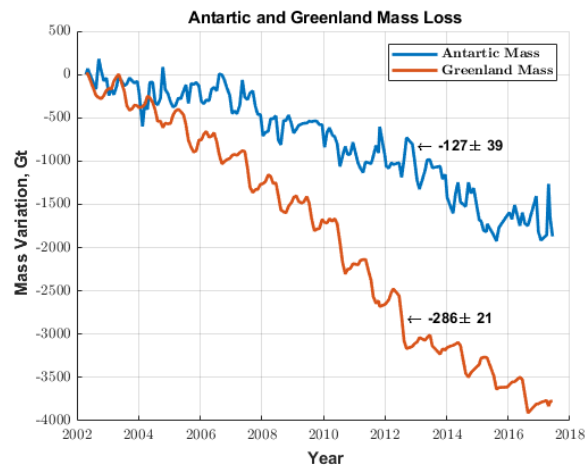


Figure 7: Antarctica and Greenland mass trend obtained by GRACE observation. These data are provided by the work of Watkins et al.[21]

3. The observation of sea level variation due to melting glaciers from 1993 up to now, reported in Fig. 8. Slight difference is present with the data presented by NASA since the data reported here are those of Global Mean Sea Level (GMSL) where the Global Isostatic Adjustment (GIA), i.e. the movement of the Earth's crust, is not taken into account. Moreover, the zero corresponds to the sea level in 1993 for us. Nowadays, the increase is estimated to be around 3.3mm per year. For information about the data generation refer to [22]

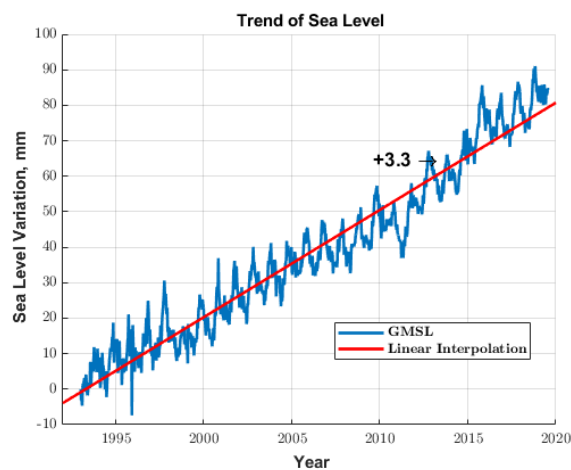


Figure 8: Sea level increase due to melting glaciers. The data are provided by the Integrated Multi-Mission Ocean Altimeters project of NASA[22]

These observations explain why the governments of the different Nations have allocated an increasing amount of funds to find sustainable solution for energy distribution and, moreover, manners to recover the energy wasted into the environment have become an interesting field of research. To cite two out of many relevant examples, we may recall the International Energy Outlook 2019[23] delivered by the US Energy Information Administration [24] and the independent assessment issued by the UK Committee on Climate Change under the request of the UK Government.

1.2 A world of Energy

The technological innovation and the need for energy is a matter of fact in the actual world. To highlight the critical aspect of energy issues, we may recall that the world energy consumption in 2040 is expected to surpass 200,000 TWh/year where the industry sector (expected to increase by an 18% from 2015 to 2040) would play for more than 50% of that amount. In regards of UK, the national target defined by the Government is the achievement of more than 20% increase in industrial energy efficiency by 2030. Action plans are therefore required by UK and other virtuous Governments, to support innovation and make it easier to access financial resources. To make an example, the important role of the industrial sector on the overall energy consumption is evident in America thanks to the data provided by the online archive U.S. Energy Information Administration (EIA) [25].

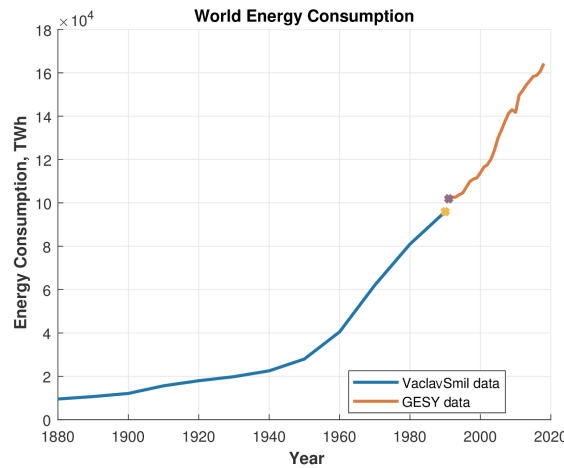


Figure 9: Global energy consumption trend during the last 140 years. The energy sources that have been taken into account are: coal, crude oil, natural gas, hydroelectricity, nuclear electricity and biofuels for data until 1990. Data provided by the Global Energy Statistical Yearbook (red) are more precise and complete, for this reason the two curves are slightly mismatched at 1990 entry.[26, 27]

From the data provided by the Global Energy Statistical Yearbooks (GESY)[27] and the work of Vaclav Smil[26] (data until 1990), it has been recovered the Fig. 9, where the world energy consumption, from whatever source either renewable or not, follows a monotonic increase. This means that also the amount of energy wasted in atmosphere is increasing in time since, because of the efficiency of production processes, for each unit of, e.g., electrical energy almost 2 are wasted.[28] This is one of the reason that has brought to the development of techniques able to reduce the impact and recover the energy wasted into the environment under the form of heat, thus augmenting the efficiency of several processes like production, storage and delivery.

1.3 Waste Heat Recovery: Toward a Cleaner World

As previously mentioned the wasted energy is mainly disperse under the form of **wasted heat**. For this reason, the focus of the research is on its conversion into other favorable forms like electricity. This field is known as **waste heat recovery** where the term groups all those techniques able to exploit heat at high temperatures to generate other forms of energies. Typically, the goal is to increase the efficiency of the machinery and when the dispersed energy is employed to generate power with no combustion and emission, the process is named **waste heat to power**. However, it is necessary to discriminate among different kinds of wasted heat. In fact, their temperature plays a very important role since the efficiency (η) of a thermodynamic process is strongly coupled with the temperature difference (ΔT) between the hot (T_H) and cold (T_C) source (typically environment) according to Carnot efficiency:

$$\eta = 1 - \frac{T_C}{T_H} \quad (1)$$

where the temperature are expressed in kelvin [K]. Even if in literature is not present a clear distinction, we can introduce the following categories:[29]

- **High-Grade (HG)**: this is the wasted heat mainly emitted by iron and steel, glass, nonferrous metals, bricks and ceramics industries. It is the highest quality heat and can be easily recovered with a good improvement of efficiency. Its temperature is typically above 500°C ;
- **Medium-Grade (MG)**: is most widely found in the chemicals, food and drink, and other process industries. Its temperature lies around $200 \div 400^\circ\text{C}$.
- **Low-Grade (LG)**: it is present in every areas of industry but also the flux emitted by our body is considered to belong to such category. Extensive

literature is present on solid state devices realized to recovered LG wasted heat (LGWH), in many different situation and particularly interesting concerning wearable devices are the work performed by Torfs and Leonov[30, 31, 32, 33]. It is the most difficult to recover since its quality is very low and the devices proposed so far do not show a very good recovering efficiency.

With the term **quality** it is indicated the usability of the waste heat, i.e. the amount of energy it can actually be extracted from the overall **heat content** or **quantity** of energy contained in a waste heat stream. We can express this latter according to:[28]

$$\dot{E} = \dot{m} \cdot h(T) \quad (2)$$

where \dot{E} [$J s^{-1}$] is the waste heat loss per unit time, \dot{m} [$Kg s^{-1}$] is the amount of mass flowing in a stream in unit time and $h(T)$ [$J Kg^{-1}$] is enthalpy per unit mass. The amount of heat available can be estimated using the simple formula:

$$\dot{Q} = S\vec{u}\rho c_p\Delta T \quad (3)$$

where S [m^2] is the cross sectional area perpendicular to the heat flux, \dot{Q} [$J s^{-1}$] and \vec{u} [ms^{-1}] represents the energy flow rate and the flow velocity of the heat in the fluid with density ρ [$Kg m^{-3}$] and specific heat capacity c_p [$J Kg^{-1} K^{-1}$].

1.4 Ferrofluid

Currently, a large number of Waste Heat Recovery (WHR) methods can be found in literature and have already been implemented. They can be divided into thermodynamic approaches through closed cycles and process fluids on one side, and exploitation of cross-thermal effects on the other side. In the first category can be recognized some known cycles which found space mainly in industry, automotive or thermochemical applications, like *Steam Rankine* (SRC), *Stirling* (SC), *Organic Rankine* (ORC) and *Kalina* (KC) Cycles. [34, 29, 35, 36] Concerning the mixed effects, several examples have been proposed mainly in the wearable field, as previously mentioned, where low power generation is needed to supply devices. However, it is difficult to extract a considerable amount of energy because of a trade off with the user comfort. For this reason, the idea to exploit nanoscale materials in this frame comes in order to enhance the devices efficiency since the material properties introduced at this scale are both less studied and very promising.[37] It can be noticed that the cited studies refer to solid state devices and the performances are not that satisfactory in low grade frame. In fact, these devices need a big area of application to produce enough power which is not always affordable, especially in wearable case. One way that seems to be the most auspicious nowadays to combine the nanoscale properties of solid material and the advantages of fluids, lies in the colloids, i.e. fluids having a solid phase dispersed in it. The investigation of these fluids in waste heat recovery application is a new topic which has raised considerable interest only in last decades because of, among else, the possibility to couple magnetic and fluid properties which has never been done in the past. This is due also to the fact that, until the 50s, all known ferromagnetic materials have a Curie temperature lower than their melting point. This means that it was impossible to create a liquid having magnetic susceptibility since the behavior in this phase became completely paramagnetic. The breakthrough was made by Solomon Stephen Papell [38] with the production of a stable suspension of magnetic nano-particles (NPs) in a carrier fluid.

The main motivating factor for the rapid development of this research area is a wide range of applications including: vibration damping, magnetic sealing, species separation and use in various sensors, laser radiation actuator modulators and cancer treatment to name a few. Moreover, the capability to influence a liquid by means of an external field introduces the possibility to control its flow and since the magnetic field enters in the Navier-Stokes equation (as we will see in the next sections) the motion of the overall fluid can be externally controlled.

A ferromagnetic liquid, or **ferrofluid** (FF), is a colloidal suspension of magnetizable nano-particles in a carrier fluid whose magnetic moment is much larger ($10^3 \div 10^4$ times) than ions one in paramagnetic materials. This makes the substance highly susceptible to the presence of an external magnetic field. However, once the external magnetic field is removed, the magnetisation is completely lost because of Brownian motion and Neel's relaxation¹, thus the FFs are classified as **superparamagnetic** substances (see subsection 2.2.1). This motion derives from thermal agitation which has the further task of holding suspended the NPs in the carrier fluid. To achieve this, the diameter of such spherical particles has to be kept small enough to make the thermal agitation competitive with gravitational sedimentation. So, their typical dimension is $\approx 10\text{nm}$, which makes them single-domain magnetic NPs. Moreover, to prevent the agglomeration they are coated with a surfactant, i.e. amphiphilic molecules having a hydrophobic and hydrophilic part, which act as stabilizing agents making the Van der Waals forces of repulsion sufficient to prevent coagulation due to dipole-dipole interaction. In contrast, this layer makes the overall fluid not electrically conductive. To give a better interpretation of the final structure of the NPs, I report in Fig. 10 the schematic representation given by S. Odenbach in [39].

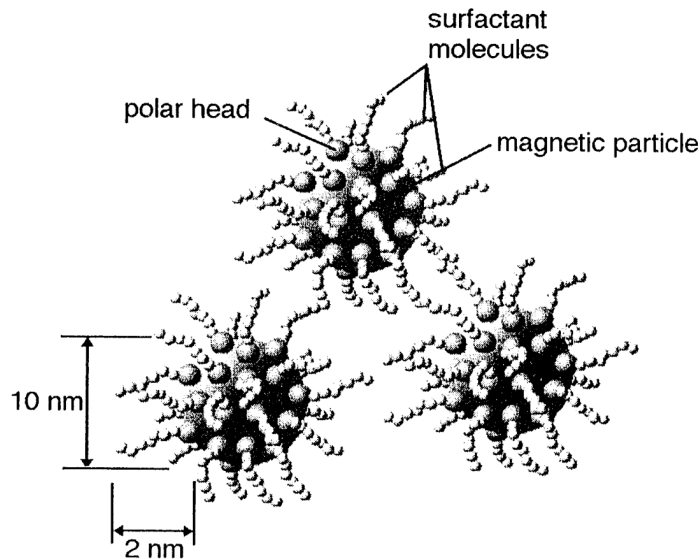


Figure 10: Schematic representation of the nano-particle structure after the coating.[39]

The ionic ferrofluids most commonly employed nowadays use NPs of maghemite ($\gamma\text{-Fe}_2\text{O}_3$ cubic lattice), hematite (Fe_2O_3 trigonal lattice), magnetite (Fe_3O_4 cubic

¹The Brownian motion dominates the de-magnetisation for large particles whereas Neel's relaxation, i.e. the magnetization flipping, mainly dominates in small particles. Because of the multi-scales we are dealing with both effects at the same time.

lattice) and other ferrites (MFe_2O_4 with M identifies a transition metal) which are electrically charged for stability reasons. Numerous are the solvents which have been adopted in the last years to suspend them but the main one can be grouped in two categories:

1. **Organic Solvents:** are type of volatile compound that has the drawback to vaporize at room temperature and to react in direct contact with sunlight producing pollutant. In this category have to be mentioned:
 - Hexane;
 - Benzene;
 - Toluene;
 - Kerosene;
 - Nitrated and Halogenated Hydrocarbons.
2. **Water:** the main difference with previous category is that they are polar molecules so the interaction among particles is avoided because of the repulsive forces provoke by H_2O molecules themselves. Moreover, because of this characteristic, when NPs are dispersed in water and a coating is added, a *double-layer* builds up instead of the *single-layer* in organic solvent.

When the water is used as carrier liquid, the pH plays an important role since acid FFs, i.e. having $pH > 7$, the particles are positively charged whereas for alkaline FFs they are negatively charged and its amount lies in the range of $1 \div 10 \mu C/cm^2$. This strongly influences the **Soret Effect** analysis in detail in subsection 2.1.4.

The ferrofluids employed in our tests present a solid phase of magnetite (Fe_3O_4 cubic lattice), selected because it remains ferromagnetic in a large range of temperatures, coated with oleic acid dispersed in kerosene and their characteristics have been reported in Tab. 1. Data have been kept from the datasheet provided by the manufacturing company (Ferrotec). Lets remember that the Curie point of magnetite NPs lies around $T_c \approx 948$ K.

	d [nm]	φ_s [% vol]	M_{sat} [mT]	ν @ 27°C [Pa s]	ρ [kg/m ³]
EMG 911	10	2.0	11	5×10^{-3}	0.89×10^3
EFH1	10	7.9	44	6×10^{-3}	1.21×10^3
EFH3	10	12.0	65	18×10^{-3}	1.42×10^3

Table 1: Main properties of the ferrofluids employed. The data are provided by Ferrotec.[40]

One of the main problem in the colloidal suspensions is the presence of aggregates that deeply modify the FFs properties. Their formation probability is affected by some parameters like:

- **Particles shape:** this parameter is indirectly linked to the statistics since it acts on the Néel relaxation time, given by[41]

$$\tau_N = \tau_0 \exp\left(\frac{KV}{k_B T}\right)$$

Here τ_0 [s] is a constant in the nanosecond order, V [m³] the volume of magnetic particle and K is a magnetic anisotropy constant linked to the shape and crystallography. Increasing the relaxation time the probability of interaction increases.

- **Particles concentration:** since the magnetization and, consequently, the magnetic force are both dependent on the amount of solid phase present in the carrier fluid[42], the probability of interaction varies accordingly;
- **Particles size:** as it will be seen in next section, one of the first relation among aggregates formation and size has been discovered by Pshenichnikov *et al.*[43] and can be appreciated in Eq. 65 where the role of the particle size results clear.
- **Coating:** when it is *complete* the particle is more inclined to repel the other but when we are in presence of *partial* coating, due to a non-zero probability of coating detachment, the aggregation probability increases. Straightforwardly, the presence of some coating molecules in the carrier fluid makes the overall liquid a multi-phase system.

By properly setting these parameters this problem can be mitigated but not completely removed.

2 Physical Basis

In this section the aim is to provide a description of the phenomena occurring in a magnetic fluid under the combination of an external magnetic and thermal field. Mainly, these phenomena are the thermo-magnetic and gravitational forces for what concerns the fluid motion. However, a particular attention is given to those mechanisms contributing both to increase the effect of magneto-convection or natural convection and also the energy generation/conversion. Naturally, the thermodynamic aspect is particularly important since the major contribution to the convective particles motion is due to the heat flux.

2.1 Thermodynamic Effects

The first aspect analysed is the thermodynamic one: the aim is to provide an overview about the major figure of merit (FoM) used to characterize the thermodynamic state of the system. From them, the properties of the material will be derived and organized in a Hessian matrix. Finally, the effect of thermodiffusion and pyroelectricity, along with an idea of its implementation in the system, are provided.

2.1.1 Fundamentals

Studying the behaviour of a system, composed by many constituents like particles or molecules, a limit in the classic theory has to be faced off. Thermodynamic is able to predict with good precision the properties of a system and their evolution in time but only from a macroscopic standpoint. The reason comes out evident thinking to the fact that, to predict the behaviour of each single particle in a structure having an Avogadro's number of them, means to solve a system composed by at least² one equation for each of them. Clearly, a system like that is not solvable in a reasonable time even for a computer. This is why a new formalism is introduced for the study of micro-systems: **statistical mechanics**. The main difference among this two approaches is the concept of micro-state which is defined as the specific configuration the system can assume in a specific instant due to thermal fluctuation. It is characterized by a probability distribution that identifies the possibility of

²Typically there are more than that since the degrees of freedom of a free particle are six, three for rotation and three for translation.

evolution from an event A to an event B following any possible path having equal probability to take place. Thus it can be concluded that the thermodynamics is nothing but an average behaviour of the system of the ensemble of all the possible evolution.

The proof of the connection among these two theories is easily demonstrated remembering that the most fundamental assumption of statistical mechanics is the *equal a priori probability*. This assumption with an isolated system makes possible to describe it with a micro-canonical ensemble³. Further, for this ensemble the ergodic hypothesis is assumed to be valid and its distribution function is:

$$\rho(q, p) = \begin{cases} 1, & E < H(q, p) < E + \Delta \\ 0, & \text{otherwise} \end{cases} \quad (4)$$

This description is possible because the total energy E is known with an uncertainty Δ which is very small compared to E ⁴. The term $H(q, p)$ is the Hamiltonian of the system described from a macroscopic point of view and (q, p) is a compact notation to indicate, taking N particles, with $(\{q\}) = (q_1, \dots, q_N)$ the Cartesian coordinates and with $\{p\} = (p_1, \dots, p_N)$ the momentum. Moreover, the condition $H(q, p) = E$ determines a hyper-surface and its integral on the volume is zero. Thus the distribution function becomes:

$$\rho(q, p) = C\delta(E - H(q, p)) \quad (5)$$

where $\delta(x)$ is the Dirac delta and C is a parameter that satisfies the normalization condition⁵:

$$\frac{1}{C} = \int_{E < H < E + \Delta} d^{3N}q d^{3N}p \quad (6)$$

Introducing the volume of the phase space or **phase extension of the ensemble**

$$\Gamma(E, V, N) = \frac{1}{h^{3N} N!} \int \rho(q, p) d^{3N}q d^{3N}p$$

which represents the volume of quantum states available for the system, the entropy

³The micro-canonical ensemble is defined as a statistical set describing those systems with fixed volume, energy and particles number or, in other words, having constant total energy.

⁴This is not a restrictive assumption when the fluctuation are never so strong to deviate the value from the average energy E

⁵The reason for the superscript $3N$ lies in the degrees of freedom of each particle (3).

can be deduced by:

$$S(E, V, N) = k_B \ln(\Gamma(E, V, N)) \quad (7)$$

where $k_B = 1.380\,649 \times 10^{-23} \text{ JK}^{-1}$ indicates the Boltzmann constant and the expression is representing the link among thermodynamics and statistical mechanics and the fact that the entropy is an additive quantity whereas the volume of each microstate is a multiplicative one and therefore could be represented by the logarithm. A further link among these approaches is given when a *reversible* transformation is considered, i.e. the passage between state A and B occur so slowly that each intermediate state C is considered to be in thermodynamic equilibrium. During the transformation, the ensemble is represented by a set of points distributed in the phase space evolving slowly and deforming under the action of an external factor coupled to the system. This ensemble is said to be microcanonical and the entropy variation in an infinitesimal step C_i to C_{i+1} can be written as:[44]

$$dS(E, V, N) = \left(\frac{\partial S}{\partial E} \right)_{(V, N)} dE + \left(\frac{\partial S}{\partial V} \right)_{(E, N)} dV + \left(\frac{\partial S}{\partial N} \right)_{(E, V)} dN \quad (8)$$

with E [J] energy, N number of particles and V the volume of the system. In order to re-write in a more ordered way above expression, the following concept can be introduced:

- **Thermal Equilibrium:** assuming two completely isolated systems 1 and 2 separated by a wall allowing heat transfer, we can define the overall entropy as:

$$\delta S = \left(\frac{\partial S_1}{\partial E_1} \right) \delta E_1 + \left(\frac{\partial S_2}{\partial E_2} \right) \delta E_2 \quad (9)$$

Since the system is isolated the overall energy exchanged with the environment $\delta E_1 + \delta E_2 = 0$. It is easy, under these conditions, to extract from above formula the relation:

$$\left(\frac{\partial S}{\partial E} \right) = \frac{1}{T} \quad (10)$$

- **Mechanical Equilibrium:** taking the same apparatus analysed so far but adding the possibility for the barrier to displace to allow volume variation of the subsets, it can be written:

$$\delta S = \left(\frac{\partial S_1}{\partial V_1} \right) \delta V_1 + \left(\frac{\partial S_2}{\partial V_2} \right) \delta V_2 \quad (11)$$

In equilibrium condition, being the overall volume fixed, the pressure has to

be equal $p_1 = p_2$ and Eq. 11 can be re-written as:

$$\delta S = \frac{1}{T}(p_1 - p_2)\delta V_1$$

where the definition $p \equiv T \left(\frac{\partial S}{\partial V} \right)_E$ as been used.

- **Particles Equilibrium:** following the same reasoning, i.e. fixing volume and energy, it can be written:

$$\delta S = \left(\frac{\partial S_1}{\partial N_1} - \frac{\partial S_2}{\partial N_2} \right) \delta N_1 = -\frac{1}{T}(\mu_1 - \mu_2)_{E,V} \quad (12)$$

holding the definition of chemical potential $\mu = -T \left(\frac{\partial S}{\partial N} \right)_{E,V}$

Thus, Eq. 8 can be restated as:

$$dS(E, V, N) = \frac{1}{T}dE + \frac{p}{T}dV - \frac{\mu}{T}dN \quad (13)$$

which can be manipulated in order to obtain the **first law of thermodynamics**:

$$dE = TdS - pdV + \mu dN \quad (14)$$

which states that the variation of internal energy $dU = dE - \mu dN$ is equal to the difference between the heat provided $dQ = TdS$, which derives from the second law of thermodynamics stated for reversible processes, and the mechanical work done on it $dL = -pdV$, where the contribution of electric/magnetic field and chemical potential have not been taken into account (see next subsection for their insertion).

2.1.2 Thermodynamic Potentials

The internal energy U [J] of a system is a function of the entropy, volume and chemical potentials, as just obtained, but also on the electric and magnetic field. This is given by Euler Fundamental Equation:[45]

$$U = \underbrace{TS}_{Heat} - pV + \underbrace{\vec{m} \cdot \vec{B} + \vec{P}_e \cdot \vec{D} + \sum_{i=1}^N \mu_i N_i}_{Overall Work} \quad (15)$$

where the first part is the integral form of the first principle of thermodynamic, the third term accounts the magnetic work W_M , the fourth the electrical work W_D with \vec{P}_e representing the polarization vector and the latter the chemical one W_C . Now, in order to define the thermodynamic state of a system we need to introduce the thermodynamic potentials. This can be done starting from the Legendre-Frenchel transform, typically called simply **Legendre transform** (LT), which allows to transform the function of a vectorial space in a dual space. In other words, it allows the passage from a space V , set of vectors, defined on k and not necessarily finite, to a space W having the same domain of definition k . The set of the linear application f is the dual space V^* [44]:

$$V^* = \{f : V \implies W | f \text{ linear application}\}$$

In particular, the LT of a function f can be expressed as:

$$f^*(p) = \max(px - f(x)) = xf'(x) - f(x) = px(p) - f(x(p)) \quad (16)$$

where the first equality holds since, solving for the point x for which we get the maximum of $px - f(x)$, we get $p \equiv \nabla f(x)$. Thus, we have that the function f has been transformed into another function explicitly depending on the derivative f' .

From this definition, the **Helmholtz free energy** can be defined as the opposite of the Legendre transform of internal energy U with respect to entropy:

$$F(T, V, N) = -\frac{\partial U}{\partial S}S + U = U - TS \quad (17)$$

coming from the definition of entropy. It represents the maximum useful work that can be extracted by a isotherm and isochoric transition. Further, the **enthalpy** is another important quantity indicating the amount of energy needed to create the system and to maintain the condition of pressure and volume. It is defined as the opposite of Legendre transform of U with respect to volume V .

$$H(S, p, N) = -\frac{\partial U}{\partial V}V + U = U + pV \quad (18)$$

Finally, most important among the thermodynamic potentials, is the **Gibbs free energy** that can be defined as the Legendre transform of the internal energy U given by Eq. 15. Thus, its differential form, considering M_p [T] the particle magnetization,

P_e [C] the electrical polarization and B [T] magnetic flux as parallel, is given by:

$$dG = -SdT + Vdp + M_p dB + P_e dD + \sum_{i=1}^N \mu_i dN_i \quad (19)$$

with D [C m⁻²] electric displacement field. This equation represents the maximum amount of work performed by a system during a reversible transformation. In other words, it is the work that can be extracted from a closed apparatus during an isobaric and isotherm transformation. From this it follows that if it is negative the transformation will be spontaneous.

The importance of these quantities is given by its link with the internal energy U , where the Gibbs one is given according to the formulation:

$$G = U - TS + pV \quad (20)$$

which allows to recover the link among the thermodynamic variables, under the assumption of closed systems, given by Maxwell relations:

$$\left(\frac{\partial T}{\partial V}\right)_S = -\left(\frac{\partial p}{\partial S}\right)_V = \frac{\partial^2 U}{\partial S \partial V} \quad (21)$$

$$\left(\frac{\partial T}{\partial p}\right)_S = \left(\frac{\partial V}{\partial S}\right)_p = \frac{\partial^2 H}{\partial S \partial p} \quad (22)$$

$$\left(\frac{\partial S}{\partial V}\right)_T = \left(\frac{\partial p}{\partial T}\right)_V = -\frac{\partial^2 F}{\partial T \partial V} \quad (23)$$

$$-\left(\frac{\partial S}{\partial p}\right)_T = \left(\frac{\partial V}{\partial T}\right)_p = \frac{\partial^2 G}{\partial T \partial p} \quad (24)$$

2.1.3 Material Properties

The importance of Gibbs potential, represented by Eq. 19, lies in the information it holds inside regarding the material properties. In fact, performing the second order partial derivatives with respect to every single independent variable it is possible to recover all the information about the physical characteristics of a material. Thus, it makes sense to introduce the concept of **Hessian matrix**, i.e. the squared matrix with

dimension $n \times n$ containing the partial derivatives of a function with n variables:

$$\mathcal{H}(G) = \begin{pmatrix} \frac{\partial^2 G}{\partial T^2} & \frac{\partial^2 G}{\partial T \partial p} & \frac{\partial^2 G}{\partial T \partial B} & \frac{\partial^2 G}{\partial T \partial D} & \frac{\partial^2 G}{\partial T \partial N} \\ \frac{\partial^2 G}{\partial p \partial T} & \frac{\partial^2 G}{\partial p^2} & \frac{\partial^2 G}{\partial p \partial B} & \frac{\partial^2 G}{\partial p \partial D} & \frac{\partial^2 G}{\partial p \partial N} \\ \frac{\partial^2 G}{\partial B \partial T} & \frac{\partial^2 G}{\partial B \partial p} & \frac{\partial^2 G}{\partial B^2} & \frac{\partial^2 G}{\partial B \partial D} & \frac{\partial^2 G}{\partial B \partial N} \\ \frac{\partial^2 G}{\partial D \partial T} & \frac{\partial^2 G}{\partial D \partial p} & \frac{\partial^2 G}{\partial D \partial B} & \frac{\partial^2 G}{\partial D^2} & \frac{\partial^2 G}{\partial D \partial N} \\ \frac{\partial^2 G}{\partial N \partial T} & \frac{\partial^2 G}{\partial N \partial p} & \frac{\partial^2 G}{\partial N \partial B} & \frac{\partial^2 G}{\partial N \partial D} & \frac{\partial^2 G}{\partial N^2} \end{pmatrix} \quad (25)$$

Remembering that the extensive parameter can be described in terms of partial derivative of Gibbs potential the above matrix can be rewritten as:

$$\mathcal{H}(G) = \begin{pmatrix} \frac{\partial S}{\partial T} & \frac{\partial V}{\partial T} & -\frac{\partial m}{\partial T} & -\frac{\partial P_e}{\partial T} & \frac{\partial \mu}{\partial T} \\ \frac{\partial V}{\partial T} & \frac{\partial V}{\partial p} & -\frac{\partial m}{\partial p} & -\frac{\partial P_e}{\partial p} & \frac{\partial \mu}{\partial p} \\ -\frac{\partial m}{\partial T} & -\frac{\partial m}{\partial p} & \frac{\partial m}{\partial B} & -\frac{\partial P_e}{\partial B} & \frac{\partial \mu}{\partial B} \\ -\frac{\partial P_e}{\partial T} & -\frac{\partial P_e}{\partial p} & -\frac{\partial P_e}{\partial B} & \frac{\partial P_e}{\partial D} & \frac{\partial \mu}{\partial D} \\ \frac{\partial \mu}{\partial T} & \frac{\partial \mu}{\partial p} & \frac{\partial \mu}{\partial B} & \frac{\partial \mu}{\partial D} & \frac{\partial \mu}{\partial N} \end{pmatrix} \quad (26)$$

where the following relationships have been introduced:

$$\begin{aligned} \frac{\partial}{\partial D} \left(\frac{\partial G}{\partial D} \right) &= -\frac{\partial P_e}{\partial D} & \frac{\partial}{\partial B} \left(\frac{\partial G}{\partial B} \right) &= -\frac{\partial m}{\partial B} & \frac{\partial}{\partial N} \left(\frac{\partial G}{\partial N} \right) &= -\frac{\partial \mu}{\partial N} \\ \frac{\partial}{\partial p} \left(\frac{\partial G}{\partial p} \right) &= -\frac{\partial V}{\partial p} & \frac{\partial}{\partial T} \left(\frac{\partial G}{\partial T} \right) &= -\frac{\partial S}{\partial T} \end{aligned}$$

In order to extract explicitly some thermodynamic and magnetic properties, a new Hessian matrix can be built:

$$\mathcal{H}(G) = \begin{pmatrix} \frac{c_x}{T} & \alpha_T V & -K_m N & -K_e N & -\frac{S}{N} \\ \alpha_T & \frac{\partial V}{\partial p} & -\rho_m N & -\rho_e N & \frac{V}{N} \\ -K_m N & -\rho_m N & -\chi_m & -\frac{\partial P_e}{\partial B} & \frac{\partial \mu}{\partial B} \\ -K_e N & -\rho_e N & -\frac{\partial P_e}{\partial B} & -\chi_e & \frac{\partial \mu}{\partial D} \\ -\frac{S}{N} & \frac{V}{N} & \frac{\partial \mu}{\partial B} & \frac{\partial \mu}{\partial D} & \frac{\partial \mu}{\partial N} \end{pmatrix} \quad (27)$$

where the following equalities have been used:

$$\chi_m = \left. \frac{\partial M}{\partial H} \right|_T \quad \chi_e = \left. \frac{\partial P_e}{\partial E} \right|_T \quad (28)$$

$$K_m \Big|_{p(V)} = \frac{1}{N} \left. \frac{\partial M}{\partial T} \right|_{p(V), H, N} \quad K_e \Big|_{p(V)} = \frac{1}{N} \left. \frac{\partial P_e}{\partial T} \right|_{p(V), E, N} \quad (29)$$

$$\alpha_T = -\frac{1}{V} \left. \frac{\partial V}{\partial T} \right|_x \quad \frac{c_x}{T} = \left. \frac{\partial S}{\partial T} \right|_x \quad (30)$$

$$\gamma_e = \frac{1}{V} \left. \frac{\partial V}{\partial E} \right|_{T, p, N} \quad \rho_e = \frac{1}{N} \left. \frac{\partial P_e}{\partial p} \right|_{T, E, N} \quad (31)$$

with Eq. 28 representing the magnetic and electric susceptibilities, Eq. 29 the pyromagnetic and pyroelectric coefficients and the subscript $p(V)$ indicate computed at constant pressure or volume, Eq. 30 the thermal expansion coefficient and the heat capacity computed at parameter x constant and finally Eq. 31 indicating the electrostrictive and piezoelectric coefficients.

2.1.4 Thermodiffusion in Ferrofluids: Soret Effect

In 1879 the physicist Charles Soret discovered[46] that if a substance like a colloid is placed in a sealed container having the two ends at different temperatures, then its composition, initially homogeneous at equilibrium temperature, shows a density variation due to particles diffusion. This phenomenon is called **thermodiffusion** (TD) or **Soret effect** or **thermophoresis** in literature.

In order to account the contribution of the conventional diffusion D and the one

given by thermo-diffusion processes D_T , the Soret coefficient is introduced[47, 46]:

$$S_T = \frac{D_T}{D} \quad (32)$$

A more meaningful form describing the relation among temperature and the consequent density gradient it provokes, 32 is:

$$0 = -\nabla\rho - \rho S_T \nabla T \quad (33)$$

with ρ indicates the density and ∇T the temperature gradient.

Thermophoresis can be completely described starting from the Fick's law of diffusion, written in terms of volume fraction φ [% vol], i.e. the ratio between the volume of a single component and the mixture's volume, and adding the TD contribution as follow[48]:

$$j = -\rho D \nabla \varphi - \rho \varphi (1 - \varphi) D_T \nabla T \quad (34)$$

with j indicating the diffusion flux [$\text{Kg m}^{-2} \text{s}^{-1}$]. Under the condition of equilibrium and stationary system, i.e. $j = 0$, this equation holds inside the proportionality constant S_T described in Eq. 32:

$$\frac{\nabla \varphi}{\varphi} = -S_T (1 - \varphi) \nabla T \quad (35)$$

which is referred to as *Soret equilibrium equation*.

Dependences Of Soret Coefficient The capability of a material to repel heat is described by the thermophobicity or by the amount of heat Q_i it is able to transfer from hot to cold side. Recently, it has been proposed to link the Soret effect to this terminology in the following sense: if $S_T > 0$ the substance, like high pH ones as can be observed in Tab. 2, is said to be thermo-phobic, since the particles tend to diffuse far away from the warm region, otherwise if $S_T < 0$, as typically occur for water based mixtures with low pH (see Tab. 3), the particles will tend to increase their concentration in the hot side so they will be said to be thermo-philic.

The Soret coefficient depends on the charge the particles develop on their surfaces. In Tab. 2 are reported several results found in literature obtained studying water-based ferrofluids with solid phase of non-coated maghemite. Unfortunately, it isn't possible to provide the results for the same FF concentration, φ , even though this parameter doesn't affect the analysis.

pH	φ , [%vol]	Surface Charge	S_T
12.87	9.93	-	+
12.56	4.96	-	+
12.4	3.97	-	+
7	6.7	+	-
7	3.3	+	-
2.46	0.32	+	-
2.91	0.32	+	-
3.49	0.32	+	-
3.49	0.32	+	-

Table 2: Soret coefficient for maghemite uncoated nano-particles as a function of pH and, consequently, to surface charge. These are disperse in water for all the present results.[47]

One of the results that can be extracted from this table is the strong link between pH and surface charge. In fact, for $\text{pH} \leq 7$, i.e. for acid solutions, it appears to be always negative while it is positive otherwise. A further distinction that needs to be done is in the repulsion mechanism avoiding agglomeration. The ionic ferrofluids (IFF) are colloids having a suspension of magnetic nano-particles without coating and exploiting Coulomb repulsion to maintain the colloid stability, whereas the surfacted ferrofluids (SFF) use steric repulsion to achieve this goal. These two big categories of FFs behave in the exact opposite way due to the charge developed by the coating which compensate the surface charge. This can be observed in Tab. 3 where the S_T of magnetic fluids with different coating and solvent have been determined.

Coating	Carrier Liquid	pH	φ [%]	SC	S_T
Beycostat	Cyclohexane		6.8	No	+
Beycostat	Cyclohexane		2.5	No	+
Beycostat	Toluene		3.3	No	+
Oleic Acid	Hexane		6.88	No	+
Oleic Acid	Octane		19.6	No	+
Ferrotec	Light Mineral Oil		3.6	No	+
Ferrotec	Water	9÷10	1.8	+	+
Ferrotec	Water	9÷10	0.45	+	+
Ferrotec	Water	8÷9	1.1	-	-
Ferrotec	Water	8÷9	0.45	-	-
Citrate Ion	Water	7	4.65	-	-
Citrate Ion	Water	7	3.3	-	-
Citrate Ion	Water	7.32	0.09	-	-
Citrate Ion	Water	7.3	0.16	-	-
Citrate Ion	Water	7.44	0.47	-	-
Citrate Ion	Water	7.57	0.79	-	-
Tartarate Ion	Water	8.93	7.23	-	-

Table 3: Soret coefficient for maghemite nano-particles as a function of pH and, consequently, to surface charge. These are disperse in water for all the present results. Beycostat and Ferrotec labels refer to the surfactants produced by these companies.[47]

The Soret effect in IFF is also subject to temperature variations since it directly influences the size and a consequently the surface charge developed by the particle itself. Depending on T , the charge can decrease provoking the flocculation phenomenon which bring the particles to sediment ($S_T > 0$) while, if it increases, the Soret coefficient will increase pushing them toward the hot side. This description doesn't holds true any more when dealing with SFF where the repulsion is due to steric interaction of the surfactants and not to Coulomb repulsion. However, it is evident the existence of a temperature dependence due to the modification of surface coating. A complete description of this relation is not still present in literature but a kinetic approach developed by Smoluchowski and Chandrasekhar has been proposed. In the work of E. Bringuier and A. Bourdon[49] a description of Soret mobility μ_S is recovered starting from a description of Brownian motion in non-uniform temperature. The Kramers equation gives the joint distribution $f(\vec{r}, \vec{p}, t)$ of coordinates $\vec{r} = (x, y, z)$ and momentum $\vec{p} = m\vec{v}$ of the particles in the colloid. In other words it describes the correlation among the movements of two particles:

$$\frac{\partial f}{\partial t} + \vec{v} \frac{\partial f}{\partial \vec{r}} + \vec{F} \frac{\partial f}{\partial \vec{p}} = \gamma \frac{\partial}{\partial \vec{p}} \cdot \left(\vec{p} f + mk_B T \frac{\partial f}{\partial \vec{p}} \right) \quad (36)$$

where m [Kg], $F(\vec{r}, t)$ [N], γ [s^{-1}] are the mass of colloidal particle the force acting on it and the frequency of collision with neighbours. An homogeneous and stationary solution of this equation, i.e. assuming the density $\rho(\vec{r}, t) = \rho$ and \vec{F} absent, is given assuming the joint distribution having the form:

$$f(\vec{r}, \vec{p}, t) = \rho (2\pi mk_B T)^{-\frac{3}{2}} \exp\left(-\frac{\vec{p}^2}{2mk_B T}\right) \quad (37)$$

However if the external force is not null ($F = -\nabla U$), the density $\rho \propto \exp(-U(\vec{r}/k_B T))$ which represent the sedimentation due to gravity in equilibrium condition. So the above solution doesn't hold any more in non-equilibrium case.

For this reason, assuming that the particle is in close equilibrium, the scattering frequency γ is very high and can be expanded in power series and the flux of magnetic particle per unit area takes the form of:

$$\begin{aligned} \vec{j} &= \iiint \frac{\vec{p}}{mh^3} f(\vec{r}, \vec{p}, t) d^3 \vec{p} \\ &= \mu [\vec{F} - \nabla(k_B T)] \rho - D \nabla \rho \end{aligned} \quad (38)$$

Assuming now both the NPs concentration and temperature as non homogeneous quantity and referring the potential U to the internal interaction of a particle with its

neighbours, the external force takes the form:

$$\vec{F} = -\nabla U = \left(\frac{\partial U}{\partial \rho} \right)_T \nabla \rho + \left(\frac{\partial U}{\partial T} \right)_\rho \nabla T \quad (39)$$

Thus substituting this result in 38 we get

$$\vec{j} = -\mu_S (\nabla k_B T) \rho - D_e \nabla \rho \quad (40)$$

where D_e represents the effective diffusivity recovered by the Debye-Huckel-Onsager theory where the diffusivity D accounts for the interaction energy E_i according to

$$D_e = D \left[1 + \frac{\rho}{k_B T} \frac{\partial U_c}{\partial \rho} \right]$$

and

$$\mu_S = \mu \left[1 + \left(\frac{1}{k_B} \frac{\partial U}{\partial T} \right)_\rho \right]$$

is the Soret mobility. Unfortunately, in the experiment this result is not directly achievable but its ratio with the effective mobility $\mu_e = D_e/(k_B T)$ can be measured. This is a very important result since the Soret coefficient can be expressed in terms of such ratio as:

$$S_T = \frac{1}{T} \frac{\mu_S}{\mu_e} \quad (41)$$

Finally, the thermophoretic force the particle will experiment can be expressed as:

$$F_S = -S_T k_B T \nabla T \quad (42)$$

2.1.5 Pyroelectric Effect

The scope of this thesis is to find a way to enhance the efficiency of the prototype, here presented in subsection 4.1, simulated by Giuseppe Fortunato in its work of thesis [1]. The phenomena consider there concern the magnetite nanoparticles ability to create a magnetic flux varying in time thanks to the combined effect of thermal and magnetic gradient. This means that the only source of energy we can harvest is tied to the electromotive force recovered by means of external coils. Thus, the idea to introduce other effects to increase the performances comes straightforward: triboelectricity, pyroelectricity or thermo-galvanic effect are just a few of the possible implementation.

Pyro-electricity (PE) is one of the most known physical phenomena of current generation. It was presented for the first time thousands of years ago even though an effective comprehension of the effect had to wait the studies on the thermodynamics of matter in 18-19th century. To better explain the relation among thermal, electrical and mechanical parameters the Heckmann diagram is reported (see Fig. 11).[50] Generally, also the magnetic effect should be accounted to provide a complete scheme but they do not play any relevant role in the PE frame.

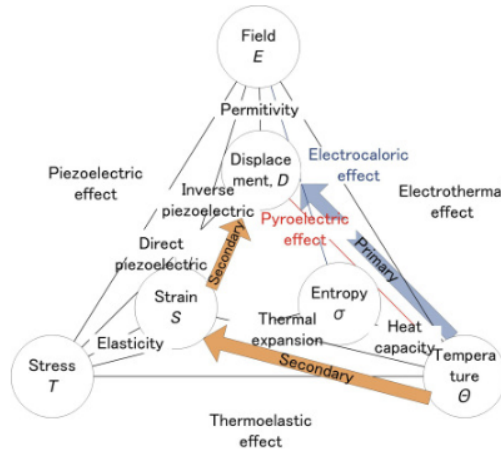


Figure 11: Heckmann diagram.[50]

The working principle of pyroelectricity is reported in Fig. 12 where a spontaneous polarization is shown to occur out of steady temperature conditions. The dipoles reorient according to the thermal gradient like if they were driven by the heat flux.

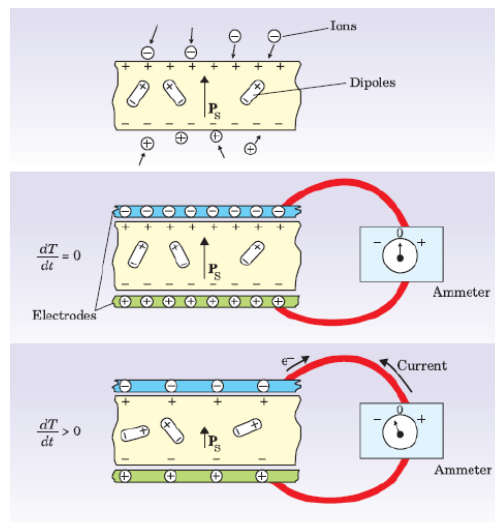


Figure 12: Scheme of pyroelectric effect working principle.[51]

In order to quantify the amount of potential difference developed onto the particles, the pyroelectric coefficient \vec{p} needs to be introduced. In first approximation it can be described purely in electrical and thermal terms by:

$$\vec{p} = \frac{d\vec{D}}{dT} \quad (43)$$

where $\vec{D} = \varepsilon_0 \varepsilon_r \vec{E} + \vec{P}_s$ represents the electric displacement field and P_s the spontaneous polarization. Assuming to not have an external field, the above formula can be restated as:

$$\vec{p} = \frac{d\vec{P}_s}{dT} \quad (44)$$

This expression holds inside the well known definition of PE effect: it is the ability of a material to spontaneously polarize once a temperature variation occur. In other words, it can be said that it represents the changes in surface charge density due to heating or cooling which is in contrast with the typical thermo-electric devices who need a stable temperature gradient to create a charge displacement. It results now evident that the presence of this effect does not depend only on the kind of material employed but also on its crystal structure since an unbalance between the centers of charges needs to be established. Thus, only some configuration, which are the same of piezoelectric effect, are suitable like triclinic, monoclinic or tetragonal.

From the work of SRINIVASAN [52], the polarization change can be expressed in terms of mechanical stress σ_{ij} as:

$$dP_k = \left(\frac{\partial P_k}{\partial T} \right)_{\sigma_{ij}} dT + \left(\frac{\partial P_k}{\partial \sigma_{ij}} \right)_T d\sigma_{ij} \quad (45)$$

where i, j, k identify the Cartesian coordinates. The same reasoning can also be performed for all the other quantities connected in the Heckmann diagram 11. In order to simplify the notation and write the PE coefficient in a more compact and manageable way, let me introduce few quantities:

- **Flexoelectric coefficient** μ_{ijkl} , which is a fourth-order tensor and represents the capability of a material to develop a potential difference under a strain gradient;
- **Piezoelectric coefficient** d_{ijk} which is a third-order tensor representing the ability to create a potential difference according to a uniform stress σ_{ij} applied;
- **Strain tensor** π_{ij} which accounts for the change in position of a point within a body under a mechanical stress.

These allow us to express the PE coefficient in a more complete way. The description is performed in terms of Cartesian components so all the subscripts are supposed to represent x, y, z coordinates:[53]

$$p_l = \frac{\partial P_{S,l}}{\partial T} + \sum_{i,j} \frac{\partial d_{lij} \sigma_{ij}}{\partial T} + \sum_{i,j,k} \frac{\partial}{\partial T} \left(\mu_{lijk} \frac{\partial \pi_{ij}}{\partial r_k} \right) + \sum_{l,i} E_i \frac{\partial \varepsilon_{li}}{\partial T} \quad (46)$$

with r_k indicating the position of the point of interest, E_i the i -th component of the electric field which has been reported for sake of completeness since no field is present in our experimental apparatus.

In Eq. 46 the four terms composing the right-hand side of the equation represents in order (starting form the first at left):

- The pyroelectric effect due to a change in polarization experienced during a temperature variation, typically called *Primary*;
- The pyroelectric charge provoked by thermal expansion and viscous stress applied onto the particle;
- The charge that builds up onto the particle due to a non-uniform stress applied, e.g. non uniform heating;
- The charge provoked by the coupling between the external field imposed and the dielectric properties of the material. In fact, the relative dielectric permittivity of a material can become temperature dependent under the action of an electric field. This is typically called *Field induced* pyroelectric effect.

The product of these three latter coefficients forms the secondary PE coefficient that is strongly connected to the piezoelectric effect.

2.2 Magnetic Effects

2.2.1 Magnetism

In this section we briefly introduce the different responses the material can have to the influence of an external magnetic field (\vec{H}). The capability of certain materials, like mineral magnetite, to attract spontaneously iron is known since the ancient world. However that is just the more evident effect but the magnetization developed within the material can be very different depending on its nature. In general, it depends on the atomic/crystalline structure of the sample, the orbital momentum and spin of the electrons and macroscopic geometry. The magnetic behaviours can be the followings.[54]

Diamagnetism: it is a quantum mechanical effect present in several materials like water, wood and also heavy metals as gold or mercury. This describe the tendency of the particles to develop an induced magnetic field in the direction opposite to the external field caused by the fact that their relative magnetic permeability μ_r is very small and thus the magnetic susceptibility $\chi_r = 1 - \mu_r$ is slightly lower than 1. Typically, this effect is very weak and we don't see any macroscopic consequence. However, when it is the only contribution, i.e. in **diamagnetic** materials, the repulsive force can be so strong to cause levitation. However, a difference arise when dealing with metal since the Langevin's description of diamagnetic susceptibility χ (see Eq. 47 suitable for non-metals) fails due to the presence of *non-localized* electrons. Thus, it has to be adjusted with the Landau's theory of diamagnetism, whose shape takes the form reported in Eq. 48 for low magnetic field intensity. In these equations $\mu_0 = 1.256637 \times 10^{-6} \text{ H m}^{-1}$ is the vacuum magnetic permeability, Z the number of electrons, e the unit charge, m_e [eV] the effective electron mass, $\langle r^2 \rangle$ the mean square distance of electrons from nucleus and E_F is the Fermi energy.

$$\chi = -\frac{\mu_0 e^2 Z n}{6m_e} \langle r^2 \rangle \quad (47)$$

$$\chi = -\frac{\mu_0 e^2}{12\pi^2 m_e \hbar} \sqrt{2m_e E_F} \quad (48)$$

Paramagnetism: it is an effect that builds up whenever we are dealing with a material that is weakly attracted by the external magnetic field, like aluminium, oxygen, titanium and iron oxide just to name a few. Further, the attraction is influ-

enced positively by the induced magnetic field within the sample itself. Physically this effect takes place because of the unbalance of electrons in the more external atomic/molecular orbit. More precisely, they contain just one electron that, thanks to its spin that aligns according to external field, acts like a magnet provoking attraction toward the region with stronger \vec{H} . This phenomenon can be described either in term of permanent magnetic moments of the ions or in term of electron motion in the conductive material. The former takes the name of Curie's law and states that the magnetization (\vec{M}) of a particle descreases with temperature (T) as follows:

$$\vec{M} = \frac{C}{T} \vec{H} \quad (49)$$

where $\chi = C/T$ and C is the Curie constant which, neglecting the mutual magnetic dipole-dipole interaction between paramagnetic ions, takes the form

$$C = \frac{n g_J \mu_B \sqrt{J(J+1)}}{3k_B}$$

with g_J Landé g-factor⁶, $\mu_B = \frac{e\hbar}{2m_e} = 9.274 \times 10^{-24}$ ($[J T^{-1}]$) Bohr magneton and J angular momentum.

For the second instead, we need to refer to Puali's theory of paramagnetism which simply state that the magnetisation can be expressed as:

$$\vec{M} = \mu_B (n_{\downarrow} - n_{\uparrow}) = \mu_0 \mu_B^2 g(E_F) \vec{H} \longrightarrow \chi_P = \frac{\vec{M}}{\vec{H}} \quad (50)$$

where χ_P is the Pauli paramagnetic susceptibility and $g(E_F)$ is the density of states at Fermi energy.

Ferromagnetism: it is certainly the most known effect and also the most powerful one. This term is used to indicate any material which can, in principle, develop a spontaneous magnetization. Contrarily to paramagnets, ferromagnets retain the magnetization once the external perturbation is removed making possible to realize permanent magnets. Such material have all the magnetic dipoles aligned with the external magnetic field. Notice that this effect have not to be confused neither with **Ferrimagnetism**, where the overall magnetisation is partially counteracted by a population of atoms developing a weak opposite magnetic field, nor with **Antiferromagnetism**, where neighbouring electrons have opposite spins developing

⁶The Landé g-factor is a dimensionless number which characterizes the magnetic moment and angular momentum of an atom for weak magnetic fields.

magnetic moment of same intensity and thus no spontaneous magnetization occur.

Superparamagnetism: it is a form of ferromagnetism that occurs in nanoparticles. Here, the magnetization can flip its direction just because of the thermal agitation, according to Neel's relaxation and in absence of external magnetic field, the magnetization results to be null. So in principle we can say that the materials in which this effect is present are ferromagnetic or ferrimagnetic ones but behaving as paramagnetic when the external field is removed. The description of the relation between magnetization and the external field for n NPs is given by Eq. 51 where $L(x) = \frac{1}{\tanh(x)} - \frac{1}{x}$ is the Langevin's function deriving from the analysis of a paramagnetic material in statistical mechanics.

$$\vec{M}(\vec{H}) = n\mu_0\mu_r L\left(\frac{\mu_0^2\mu_r\vec{H}}{k_B T}\right) \quad (51)$$

The slope of the curve given in Eq. 51 represents the magnetic susceptibility:

$$\chi_m = \frac{\partial \vec{M}(\vec{H})}{\partial \vec{H}} = \frac{n\mu_0^3\mu_r}{3k_B T} \quad (52)$$

2.2.2 Magnetization

The term **magnetization**, typically indicated with \vec{M} is defined as the total magnetic moment per unit volume or, in other words, as the vector expressing the density of magnetic dipoles formed spontaneously or because of the external field. Thus, this represents also the ability of the material to re-orient its magnetic dipoles according to \vec{H} direction creating a further contribution to the magnetic flux density which takes the general form of:

$$\vec{B} = \mu_0(\vec{H} + \vec{M})$$

For what just said, a relation among the intensity of the applied field and the NPs magnetization is always present in every material. However, in the particular case of paramagnet and ferromagnet this relation can be expressed as:

$$\vec{M} = \chi\vec{H} \implies \chi = \frac{\vec{M}}{\vec{H}} \quad (53)$$

where a linear dependence clearly exists. As we have already stated in previous sections, for paramagnetic materials the moment, randomly oriented initially, slightly

re-orient in the presence of magnetic field and the susceptibility is positive since the magnetization and magnetic field have the same direction.

Let us assume that the magnetic and electric field vectors form an angle θ between them

$$E = -\mu B \cos(\theta)$$

and that the probability of occupation of a state with energy E_l is given, for sake of simplicity, by Boltzmann statistics⁷:

$$P(E) = \exp\left(-\frac{E}{k_B T}\right) = \exp\left(\frac{\mu B \cos(\theta)}{k_B T}\right) \quad (54)$$

For what concerns superparamagnetic nano-particles, like in our case, we can consider the magnetic moments \vec{m} [$A \cdot m^2$] to re-orient almost immediately with the application of an external field. Moreover, we consider it constant in module for all the NPs and thus like a vector just rotating on a sphere of radius $|\vec{m}|$. This means that the overall probability for magnetization moment to assume a certain direction spanning on the interval $[\theta, \theta + \partial\theta]$ is given by:

$$p(\theta) = \frac{P(E) \sin(\theta) \partial\theta}{\int_0^\pi P(E) \sin(\theta) \partial\theta} \quad (55)$$

that is also dependent on the magnetic field and temperature[54]. Expressing now the magnetization \vec{M} of N particles, or moments since they are assumed to be single-domain, in the direction of \vec{H} the following expression is obtained.

$$M = \int N \mu \cos(\theta) p(\theta) = N \mu \frac{\int_0^\pi P(E) \cos(\theta) \sin(\theta) \partial\theta}{\int_0^\pi P(E) \sin(\theta) \partial\theta} \quad (56)$$

where, the fraction term after integration becomes the well known Langevin's equation:

$$L(\Gamma) = \frac{M}{M_s} = \coth(\Gamma) - \frac{1}{\Gamma} \quad (57)$$

with $\Gamma = \frac{\pi}{6} \frac{M_d H d^3}{k_B T}$ is the Langevin's parameter, d is the particle diameter, M_d and $M_s = \phi M_d$ are the domain⁸ and saturation magnetization, respectively. So finally

⁷In general Fermi statistic is better since is more accurate when we are dealing with *degenerate* materials and in particular for fermions. However, the accuracy of Boltzmann statistic is sufficient in many cases, mostly when the incomplete ionization is assumed.

⁸With the term domain magnetization it is referred to the magnetization value of a magnetic phase at a given temperature.

the magnetization can be rewritten as:

$$M = N\mu L(\Gamma) \quad (58)$$

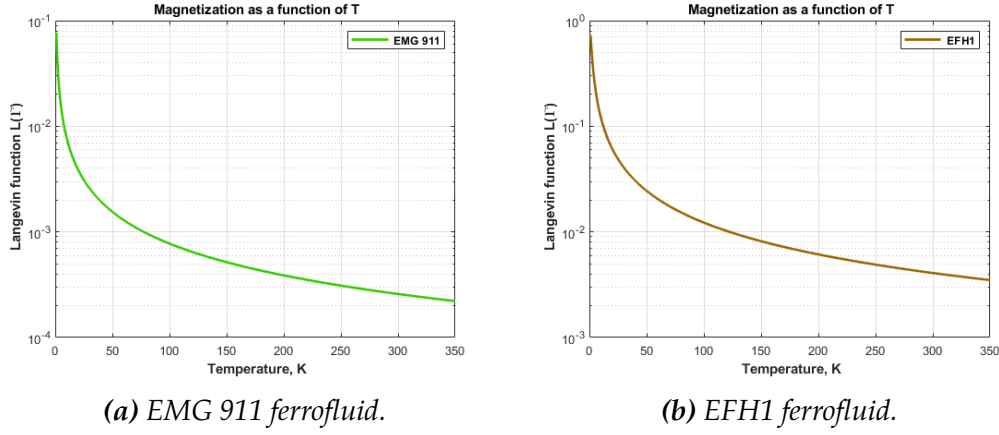


Figure 13: Temperature dependence of Langevin's function for different kinds of FFs.

It is evident that fixing the external field intensity and varying T , $L(\Gamma)$ varies as shown in Fig. 13, which has been created using MATLAB® software assuming $H = 35 \text{ kA m}^{-1}$ and the other parameters according to those of Tab. 1. It is reported the behaviour also for low temperature and the behaviour expected from the $\coth(x) - \frac{1}{x} \approx \frac{x}{3}$ obtained by Taylor expansion is recovered. This equation is particularly valid in case of large magnetic moments which is in good agreement with the assumption of superparamagnetic particles.

Generally, the magnetization of a paramagnetic material can be seen as the sum of the quantized angular momentum (M_J) of each single atom. Expressing the total angular momentum as $\vec{J} = \vec{L} + \vec{S}$ with \vec{L} orbital angular momentum of the electrons and \vec{S} their total spin and the magnetic moment along the component of the field as $\mu = -g_J\mu_B M_J$ with $-J < M_J < J$ we find the magnetization as a sum of all possible M_J :

$$\begin{aligned} M &= Ng_J\mu_B J \left[\frac{2J+1}{2J} \coth\left(\frac{2J+1}{2J}\Omega\right) - \frac{1}{2J} \coth\left(\frac{\Omega}{2J}\right) \right] \\ &= Ng_J\mu_B JB_J(\Omega) \end{aligned} \quad (59)$$

where B_J is the Brillouin function and $\Omega = \frac{g_J\mu_B JB}{k_B T}$ with g_J Landè g-factor and μ_B Bohr magneton. It is interesting to notice that if $J \rightarrow \infty$ the Langevin's equation is recovered. Expanding in Taylor series both the Langevin and Brillouin functions,

the magnetic susceptibility, remembering equation 53, can be expressed as:

$$\chi_c = \frac{\mu_0 N \mu^2}{2k_B T} \quad (60)$$

$$\chi_q = \frac{\mu_0 N g_J^2 \mu_B^2 J(J+1)}{3k_B T} \quad (61)$$

which are both forms of Curie law but the first can be seen as the "classical" derivation while the second is the one for quantum-mechanical magnetic moments. In general it can be written that the susceptibility $\chi = C/T$ is the ratio between the Curie constant C , whose definition depends on the approach and the working temperature. However, this is correct only in the case of non interacting particles, which is pretty much our experimental situation also thanks to surfactants counteraction the attraction.[55]

For the sake of completeness it has to be said that the Curie-Weiss law avoid the problem of magnetization description above the Curie temperature introducing the *Weiss temperature* Θ measuring the interaction between moments. It gives us the magnetization behaviour of a ferromagnetic material after the phase transition has been suffered, i.e. at $T > T_C$. In this region, the correct expression of the susceptibility becomes:

$$\chi = \frac{C}{T - \Theta} \quad (62)$$

This temperature is calculated assuming the overall field sensed by the particle as a superposition between the external and a mean field generated by all the other magnetic moments. These latter fields are called *molecular field* $H_m = \lambda M$, with λ molecular field constant determined empirically, and is like an average field provoked by the particles substituting the interaction among them. For this reason, this theory is called **mean field theory (MFT)**. The Eq. 62 shows a divergence for $T = \Theta$ which underlines phase transition. So this means that at temperature lower that $T_C = \Theta$ we are in ferromagnetic regime while for $T > T_C$ we have a paramagnetic behaviour since the thermal energy dominates.

Assuming to remain under the Curie temperature⁹, the Langeving's magnetization law has shown a sensible divergence with the experimental data [56] due to the previous mentioned non-interacting particles assumption. In fact, for solid phases $\varphi > 0.1$ the mutual influence becomes strong enough to be no longer negligible. For

⁹This is not a restrictive assumption since for EFH1 and EMG 911 it corresponds to a $T_C > T_W$ where T_W indicates the working temperature, i.e. the low-grade wasted heat temperature

this reason, an alternative method, the so called **second order modified mean field** (MMF2), which is an expansion of the Weiss model, has been proposed. In practice, the reason behind this new method is the computation of the effective magnetic field H_e iteratively which accounts for the mean magnetic field developed because of the particles interaction. Thus the Langevin's law is still valid but its parameter becomes

$$\Gamma_e = \frac{\pi}{6} \frac{M_d d^3 H_e}{k_B T}$$

and

$$H_e = H + \frac{1}{3} M(H) \left(1 + \frac{1}{48} \frac{dM(H)}{dH} \right) \quad (63)$$

where $M(H)$ indicated the magnetization computed using Langevin's equation 57. In Fig. 14 are shown the results obtained from magnetic susceptibility χ calculated at T and H , the one (χ_*) at reference parameter T_* and H_* , the pyromagnetic coefficient K and the difference among Langevin and MMF2 model.

Since the total magnetization value of the fluid can be seen, at least in first approximation, as the sum of all the magnetic moment of each single NPs, a dependence on solid phase concentration φ , and thus on the density ρ , is evident. According to Ivanov *et al.*[55, 57] the magnetization $M(H)$ can be rewritten as:

$$M(H) = \rho \left\langle \mu(x) L(\mu_0 \Gamma_e) \right\rangle \quad (64)$$

with $\mu(x) = \frac{\pi}{6} M_d d^3$ represents the particle dipole moment. They proved the validity of such model comparing the theoretical results with other models. Moreover, the experimental results for different ferrofluids concentration have been plotted together with the theoretical one and almost perfect agreement is shown for both low-field (Fig. 15a) and high-field (Fig. 15b) condition.

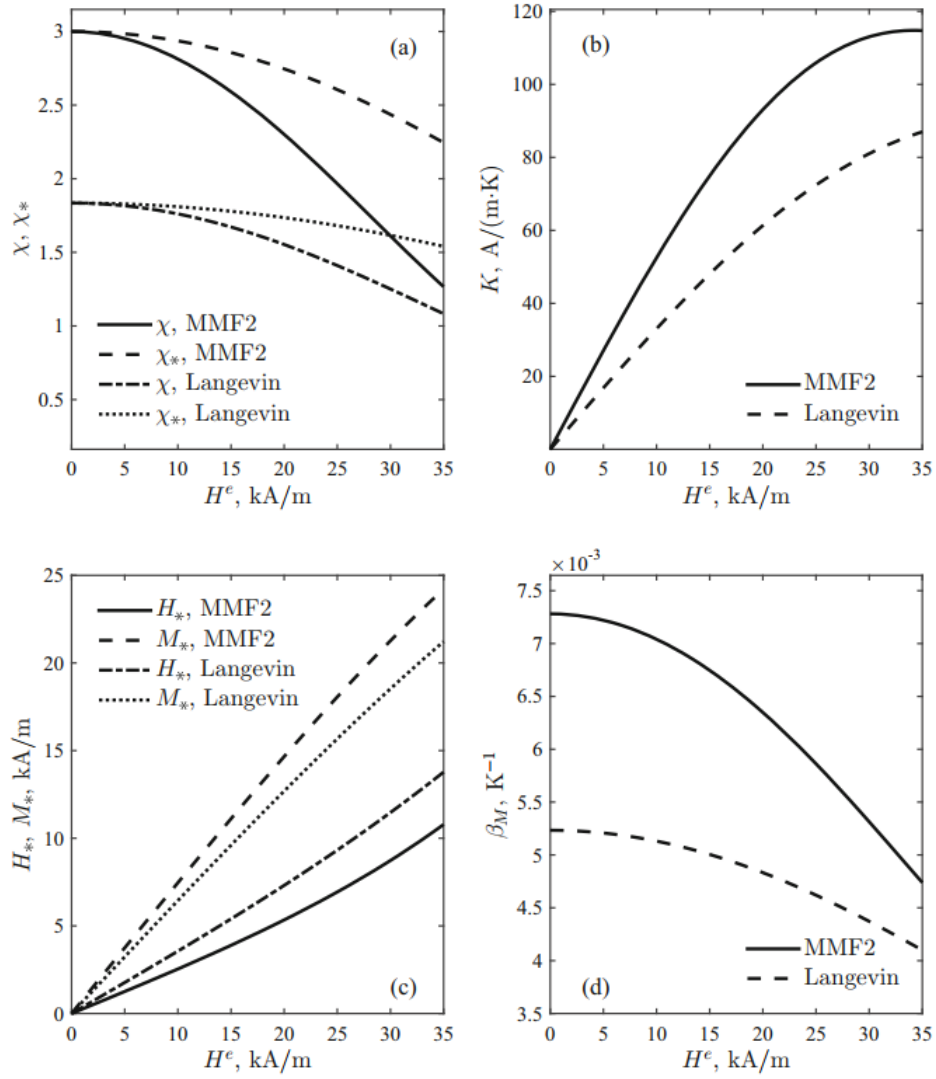


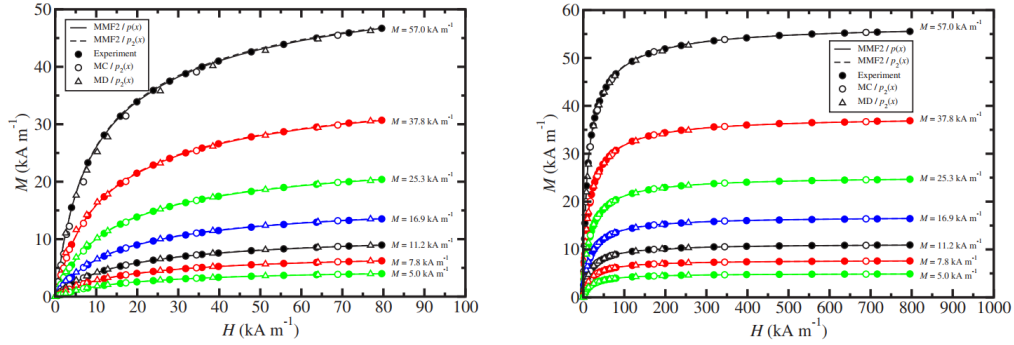
Figure 14: Comparison among Langevin's and modified mean field model. The pyromagnetic and susceptibility coefficient are plotted in the picture (a) and (b) showing the strong disagreement among the two procedures, which can be also appreciated in figure (d), where the relative pyromagnetic coefficient $\beta_M = K/M$ is reported, and in (c) with the effective magnetic field H_e as a function of reference magnetic field H_* and magnetization M_* . This picture has been taken from SUSLOV [56].

This result has been achieved starting from the distribution of magnetic NPs diameter, i.e. studying the probability of aggregates formation and their sizes, obtained by Pshenichnikov *et al.* in 1996 [43]:

$$p(x) = \frac{x^\alpha \exp(-x/x_0)}{x_0^{\alpha+1} \Gamma(\alpha + 1)} \quad (65)$$

where x represents the size, α , x_0 are the unknown and their product represents the

mode¹⁰ of the Γ -distribution¹¹ which has been proved to have very high accuracy in theoretical prediction.



(a) Magnetization curve is low-field conditions.

(b) Complete magnetization curve.

Figure 15: Magnetization curve obtained at different ferrofluid concentrations. The value of saturation magnetization is reported to the side of each curve. The experimental data refer to [43] and different methods have been used to fit the data: molecular dynamics (MD), Monte Carlo method (MC) and 2nd-order Modified Mean Field (MMF2).[55]

¹⁰The mode represents the value occurring with higher frequency.

¹¹The Γ -distribution is the maximum entropy probability distribution of a random variable Y whose expected value is fixed and greater than zero $E[Y] = k\theta$ with k and θ shape and scale parameter respectively.

2.2.3 Magnetic Force

As pointed out in the Subsection 1.4, the presence of superparamagnetic NPs like magnetite provokes a strong response to an external magnetic field which thus give rise to the so called **magneto-convection** effect. In contrast to magneto-hydrodynamics domain, where the main driving mechanism is the Lorentz force acting on the non-uniformly magnetised fluid, in ferro-hydrodynamics it is the ponderomotive Kelvin force. This latter pull the more magnetised part of the fluid to move toward the region where \vec{B} is stronger. However, it has been proven by Odenbach in [58] the invalidity of Kelvin force in ferrofluids where the susceptibility is high enough to play a fundamental role in the force description.

It has to be noticed that a gradient in the magnetic field will be present even if it is uniform across the sample. In fact, by analysing the force acting on the NPs in the apparatuses described in Section 4.1 where the FF layer is non-uniformly heated, the effect of such external perturbation can be summarized qualitatively as follow:

- In case of *non-uniform* field, e.g created by placing a simple bar magnet close to the liquid layer, the $\nabla \vec{H}$ is directly responsible for the fluid motion since a gradient of forces acting on the particles is generated;
- In case of *uniform* field, e.g. created using an electromagnet or a Helmholtz configuration, it is better to decouple the magnetic induction \vec{B} in the sum of Magnetization \vec{M} and Magnetic field \vec{H} . In this way is easy to see that, since the magnetization of the particles changes as a function of temperature, the internal magnetic field \vec{H} of the NPs has to lower where the magnetization is stronger, meaning that a magnetic field gradient presents again.

This heuristic description shows that even if the reasons are different, in both cases the magneto-convection will be observed. In order to find an expression for the force provoked by the externally imposed magnetic field, the treatment is started from the consideration that ferrofluids are dielectric and so no induced current flows across the fluid.[59] Being the particles single-domain because of their dimensions, the magnetization vector adjust its direction instantaneously according to \vec{H} . In order to make simpler the dependence of \vec{M} , discussed earlier, linearity due to slowly varying fields can be assumed by describing the variation from an internal standpoint. This means that the variation of a quantity can be described as the sum of its value in a

precise point and the small contribution due to magnetic field and temperature:

$$\vec{M} = \frac{M_* + \chi(H - H_*) - K(T - T_*)}{H} \vec{H} \quad (66)$$

where $K = -\partial M/\partial T$ and the subscript * indicates the values of parameter at a reference temperature T_* and magnetic field H_* . From this equation, we can deduce the condition leading to the so called thermo-magnetic coupling effect. By substituting it in the Maxwell equations [45] we get:

$$(1 + \chi_*)\nabla \cdot \vec{H} + (\chi - \chi_*)\nabla H \cdot \frac{\vec{H}_*}{H_*} - K\nabla T \cdot \frac{\vec{H}_*}{H_*} = 0 \quad (67)$$

where it is evidenced the scalar product among the components of \vec{H} and ∇T . Thus the components of such vectors shall have the same direction to guarantee such coupling.

Now, considering a neutral and dielectric body, the magnetic field force can be described according to Kelvin relation Eq. 68. In literature it is often found this description in terms of Lorentz force but this is a good description only if we are in presence of very high magnetic fields. [60]

$$F_K = \mu_0\chi(\vec{H} \cdot \nabla)\vec{H} = \mu_0(\vec{M} \cdot \nabla)\vec{H} \quad (68)$$

where the Eq. 53 has been exploited and χ is the magnetic susceptibility of the particles and for FF with concentration higher than 7% can be consider to be ≈ 1 . Using the linearization 66, a new expression for Kelvin force in non-uniform heating and magnetic fluids is obtained:[60, 56]

$$F_K = -\mu_0 K \Delta T \nabla H \quad (69)$$

However, in the work of Odenbach *et al.* of 2019 it has been reported that Kelvin force is not so precise in the FFs description. In fact, such description would hold in case of very small χ [58]. In magnetic colloids, as said previously, this is not the situation and this work shows that the Kelvin force can be represented in its integral form by

$$\begin{aligned} F_K &= \int [P_i \nabla E_i + \mu_0 M_i \nabla H_i] d^3 r \\ &= \int \mu_0 M_i \nabla H_i d^3 r \end{aligned} \quad (70)$$

where i represent the i-th component, the electric field is neglected according to the

experimental situation we are dealing with, compared with another expression where the magnetic intensity is substituted with the magnetic flux density $\vec{B} \equiv \mu_0(\vec{H} + \vec{M})$ to account for the dependency on the magnetic susceptibility of the fluid.

$$\begin{aligned} F_v &= \int \left[\frac{P_i}{\varepsilon_0} \nabla D_i + M_i \nabla B_i \right] d^3r \\ &= \int M_i \nabla B_i d^3r \end{aligned} \quad (71)$$

The better agreement with the set of experimental data is shown in Fig. 16 (on the y-axis is reported the parameter $\lambda \equiv 2\beta l / (mg)$, with $\beta = \frac{1}{k_B T}$, which is measured by plotting $\Delta z = \frac{\beta l}{mg} \nabla H_0^2 = \lambda H_0 \nabla H_0$ over $H_0 \nabla H_0$).

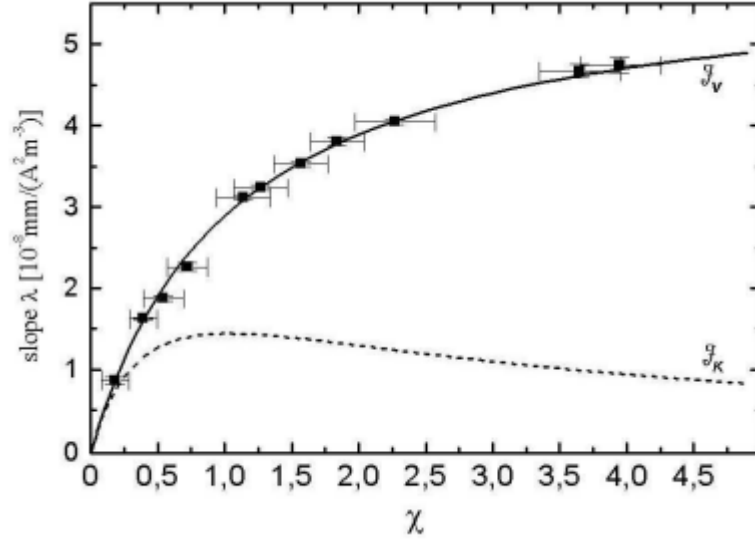


Figure 16: $\lambda = \Delta z / (H_0 \nabla H_0)$ as a function of χ . The dashed line is the Kelvin force F_K while the solid line is its variant form F_v . [58]

The result obtained in Eq. 71 can be written in differential form as

$$\vec{F}_v = (\vec{M} \cdot \nabla) \vec{B} \quad (72)$$

which will directly enter in the momentum continuity for mixtures reported in subsection 3.2.

2.2.4 Magnetophoresis

Having analysed the effect of the temperature gradient onto the particle motion, another aspect that should be analyzed when dealing with magnetic fields is the effect they produce on the concentration within a certain volume of interest. This is called **magnetophoretic** (MPH) effect and, in complete analogy with the *electrophoretic effect*, it is a magnetokinetic process for which the magnetizable particles suffer a magnetic force which drives their motion in the viscous medium[61].

Magnetophoresis has aroused increasing interest in the last decades in several fields of research, like nanoparticles synthesis or cell separation in biology, thanks to its ability to separate cells in a highly specific and sensitive way and to the relative low-cost of the apparatus. Initially, this term was referred to DC magnetic field only because of the fact that the effect was much more easy to see and the treatment is simplified due to the independence on time of the magnetic field. Nowadays, also AC magnetic field, which alternate a pulling and pushing force on the particle making it swing, are considered in the category of MPH effect and, e.g., it can be used to compute the local viscosity of the medium. Effects like Lorentz force due to interaction of magnetic field with a charged particle or other \vec{H} -matter interaction due to electrical nature of the carrier liquid or the solid phase are not considered as MPH effects[61]. For this reason and referring to our experimental setup, the treatment will be done from a general point of view and then the particular situation considering rapidly varying magnetic fields and superparamagnetic particle is discussed. An important aspect that has to be analysed is the influence of particles dimensions on this effect. In fact, in bigger particles the magnetization is higher so the MPH force will play an important role in the diffusion constant. In 1996, V. M. Buzmakov and A. F. Pshenichnikov [62] provided a method to express mathematically the dependence of the diffusion coefficient on the dimension of the particles but the magnetic force acting on the particles wasn't accounted. However, the dependence on the dimensions can be limited only to the medium and large size ones, which are the volume fraction of the i -th component ($\varphi_i = \frac{V_i}{V_T}$) considered, since for small NPs the contribution to magnetization is approximately negligible. In literature, a lot of descriptions are present regarding the mass transfer in magnetic fluid [63, 64, 65] that account at different levels of sedimentation, diffusion and interaction among particles, just to name a few. Starting from the most complete of this expression provided by Pshenichnikov *et al.*[65] the volume fraction equation, discussed in detail in the governing equation subsection 3.3, under the assumption of absence of

convective flow can be rewritten as:

$$\frac{\partial \varphi}{\partial t} = -\nabla \cdot \left\{ D_0 K(\varphi) \left(\varphi L(\Gamma_e) \nabla \Gamma_e + \varphi \vec{g} - \left[1 + \frac{2\varphi(4-\varphi)}{(1-\varphi)^4} - \varphi \frac{\partial^2(\varphi^2 G)}{\partial \varphi^2} \right] \nabla \varphi \right) \right\} \quad (73)$$

where $K(\varphi)$ is the ratio among the particle mobility in the magnetic field and carrier fluid, D_0 is the Brownian diffusion coefficient of the particle, $L(\Gamma_e)$ is the Langevin function of the effective Γ_e and $G(\lambda, \varphi)$ represents the contribution of magnetodipole interactions to the free energy, being $\lambda = \frac{\mu_0 m^2}{3k_B T V_p}$ the magnetodipole interaction parameter with m magnetic moment and V_p the NPs volume. By looking at the first term of Eq. 73, we can notice that the MPH effect for an aggregate can be expressed as their diffusion flux:[63]

$$\vec{J}_a = n D_a K(\varphi) L(\Gamma_e) \nabla \Gamma_e \quad (74)$$

where $n = \frac{6\varphi}{\pi d^3}$ is the number of particles in unit volume and D_a is aggregate diffusion coefficient. In complete analogy with this result we can express the same equation but regarding one single particle diffusion:

$$\vec{J}_s = D_s K(\varphi) L(\Gamma_e) \nabla \Gamma_e \quad (75)$$

Assuming equal contribution to the total magnetic moment and superparamagnetic NPs, i.e. \vec{M} and \vec{H} can be considered as parallel, the modulus of the MPH force can be expressed, taking into account Eq. 72 which describe the magnetic body force, as:

$$F_{MPH} = M_d V_p \nabla B \quad (76)$$

with M_d representing the magnetization value of a single domain, and the trajectory in time of magnetophoresis is traced by the well known diffusion equation:

$$\frac{\partial \varphi}{\partial t} = -\nabla \cdot (\vec{J}_a + \vec{J}_s) \quad (77)$$

To conclude, since the Langevin's function is not so suitable for these type of experiments, it is substituted with the second order modified mean field expression for the effective field given by Eq. 14 in Eq. 74. Calling D the diffusion coefficient of the NPs and defining it as the terms with the squared brackets of Eq. 73, the effective coefficient of particle diffusion in magnetic fluids can be defined as[65]:

$$\Delta D = D_0 K(\varphi) \left[1 + \frac{2\varphi(4-\varphi)}{(1-\varphi)^4} - \frac{8\lambda^2 \varphi}{3(1+1.25\lambda\varphi)^2} \right] \quad (78)$$

which is valid in weak fields. It is interesting to notice that, in colloids like ferrofluids, MPH causes stratification, i.e. region of different concentration are formed, because of the NPs drift toward region with higher magnetic field. The application of a temperature gradient, however, is able to equalize the density in the whole fluid thank to the competitive thermal perturbations.

2.3 Thermal and Magnetic Influence on Physical Properties

2.3.1 Stability Requirements

In the introduction it has been explained the reason why the particles dispersed in the carrier fluid must have a dimension of few nanometers: this allows to keep them suspended and in continuous vigorous Brownian motions. For a NP with an average diameter of $d = 10$ nm, the gravitational force E_g can be calculated, since this is nothing but the difference among its potential energy and the Archimede's force:

$$E_g = \Delta\rho Vgh \quad (79)$$

where $\Delta\rho$ is the density difference among the solvent and the NP, V the NP volume and h the height of the fluid container).

Considering the data in Tab. 1 regarding EFH1 FF, kerosene as carrier fluid and a container's height $h \approx 1$ cm, since typically is not kept higher than that because of the results obtained by Finlayson [45] which show the preponderance of magnetic effect for very thin layers (less than $h = 1$ mm) and their rapid decrease in contribution with the height increase, we have that $E_g \approx 16 \times 10^{-23}$ J. So this means that the thermal energy (E_{th}) at room temperature ($T = 300K$) is sufficient to be competitive with it. In fact, assuming a free particle moving in the fluid (6 degrees of freedom (DOF)) it can be expressed as follows:

$$E_{th} = 3k_B T \quad (80)$$

which results to be one hundred times higher that E_g .

Now, if a moderate field (set in literature at $H \approx 35$ kA/m in experiments with FFs) is applied externally, the magnetic energy (E_{mag}) supplied to the particles is:

$$|E_{mag}| = \mu_0 M_s V H \quad (81)$$

where M_s indicates the spontaneous magnetization of the NPs. Here it has to be noticed that the mutual magnetization¹² has been neglected since the NPs and their saturation magnetization are small and low enough to make this effect not appreciable. However, its presence pushes the bare particles to attract each other because of dipole-dipole interaction energy. Thus, the tendency to coagulate forming agglomerates undermines the colloid's stability. We can express the Van-der Waals interaction using the Hugo C. Hamaker approximation, derived from London's explanation of such forces, where independence among interactions has been assumed¹³:

$$E_{VdW}(z, 2R) = -\frac{A}{6} \left(\frac{2R^2}{z^2 - 4R^2} + \frac{2R^2}{z^2} + \ln \left[\frac{z^2 - 4R^2}{z^2} \right] \right) \quad (82)$$

where the particles radius have been assumed to be equal $R_1 = R_2 = R$. The Hamaker constant A (≈ 0.1 aJ for ferrites) depends on the solid phase φ and on a coefficient of interaction C which depends on the material.

Assume to deal with two different kind of nanoparticles (N_1 and N_2) suspended in a carrying fluids (Sol). The Lifshitz theory approximated under the assumption of analogous dielectric (D) and magnetic (M) properties allow to rewrite:[66]

$$\begin{aligned} A_{N_1, Sol, N_2} &= \frac{3k_B T}{2} \sum_{m=0}^{\infty} \sum_{s=1}^{\infty} \frac{(\Delta_{N_1, Sol} \Delta_{N_2, Sol})^s}{s^3} + \\ &\quad \frac{3k_B T}{2} \sum_{m=0}^{\infty} \sum_{s=1}^{\infty} \frac{(\overline{\Delta}_{N_1, Sol} \overline{\Delta}_{N_2, Sol})^s}{s^3} \\ &= A_{N_1, Sol, N_2}^D + A_{N_1, Sol, N_2}^M \end{aligned}$$

where m is a positive integer, s the surface separation and the possibility to compute separately the two contributions is underlined. The notation at subscript has to be read as: nanoparticle N_1 (N_2) interact across the carrier fluid Sol with N_2 (N_1). The two ad hoc parameters Δ and $\overline{\Delta}$, using k and l to identify the materials and solvent,

¹²The term mutual magnetization refers to the magnetization induced by a nano-particle on its neighbours.

¹³In order to extend this theory we shall account for the mutual interaction as previously said. This can be done using perturbation theory adding a small variation to the Hamiltonian of the system.

take the form:

$$\Delta_{kl} = \frac{\varepsilon_k(i\xi_m) - \varepsilon_l(i\xi_m)}{\varepsilon_k(i\xi_m) + \varepsilon_l(i\xi_m)} \quad (83)$$

$$\overline{\Delta}_{kl} = \frac{\mu_k(i\xi_m) - \mu_l(i\xi_m)}{\mu_k(i\xi_m) + \mu_l(i\xi_m)} \quad (84)$$

with i representing the imaginary unit, ε and μ are the dielectric and magnetic response functions respectively and ξ_m is the Matsubara frequency, i.e. a set sampling frequency taken according to a suitable function, for example depending on temperature: $\xi_m = \frac{4\pi^2 k_B T}{h} m$.

Going back to our experimental situation, the assumption of one single suspended material make possible to consider all the NPs identical and to evaluate the influence on A when suspended in different fluids[66]. Focusing our attention on the magnetic contribution and remembering that kerosene is a non-magnetic fluid we can express it as the static magnetic contribution:

$$A_{N_1, Sol, N_2}^M = \frac{3k_B T}{4} \sum_{s=1}^{\infty} \frac{1}{s^3} \left(1 + \frac{1}{2\pi\chi} \right)^{-2s} \quad (85)$$

with χ magnetic susceptibility. Some results of interest are reported in Tab. 4 where all the values have been reported in zepto-Joule (zJ) corresponding to 10^{-21} J.

	Vacuum [A_{N_1, Vac, N_1}]	Water [A_{N_1, H_2O, N_1}]	Hexane [A_{N_1, Hex, N_1}]	Toluene [A_{N_1, Tol, N_1}]	Hydrocarbons [A_{N_1, HC, N_1}]
Magnetite	43	33	22	9	30 - 400
Maghemite	68	36	26	18	30 - 300
Hematite	92	39	29	29	30 - 300

Table 4: Static magnetic Hamaker constant calculated for the most used materials, suspended in different fluids. The values are all given in z) and the data have been kept from [66] and there in references.

2.3.2 Thermal Conductivity

With the term thermal conductivity (κ , [$\text{W m}^{-1} \text{K}^{-1}$]) it is indicated the ratio among heat flux ($\vec{q}(\vec{r}, t)$) and temperature gradient ($\nabla T(\vec{r}, t)$) it is able to build up because of thermal conduction only, i.e. neglecting convection and radiation. In other words, it can be seen as the attitude of the material pass the heat to another one. Thus, it is expressed generally in the form:

$$\kappa = -\frac{\vec{q}(\vec{r}, t)}{\nabla T(\vec{r}, t)} \quad (86)$$

which is called Fourier's definition of heat conduction. If the solid has anisotropic properties and consequently the heat flux results to be positioned along a different direction with respect to the temperature gradient, κ becomes a tensor with rank 2.

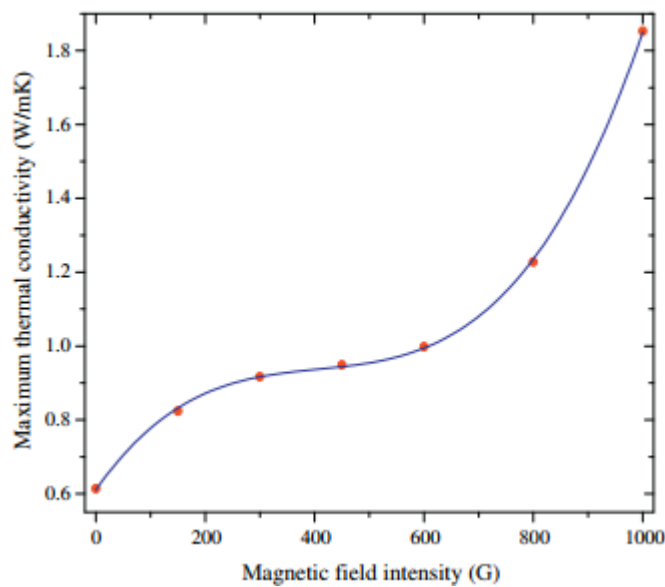


Figure 17: Thermal conductivity as a function of magnetic field[56].

When dealing with colloids, one of the parameters most affecting the thermal conductivity is the solid phase of dispersed particles, i.e. the NPs concentration. In fact, if 10% vol. of magnetite is added to the carrier fluid, κ is enhanced up to 50% with respect to case of solvent alone.[56] However, the study of Gavili *et al.*[67] conducted in the National Center for Laser Science and Technology in Tehran, show that no change in thermal conductivity is present if no external field is applied and then it can be further increased up to two/three times the baseline if other influencing factors are taken into account. The main outcomes are in regards of the magnetic field and

temperature gradient intensity and directions. They influence each other according to the Navier-Stokes equation, adapted to such experimental apparatus (see Eq. 108). In fact, considering a water-based FF at room temperature $T = 20^\circ\text{C}$, κ shows a strong non linear increase with \vec{H} , passing from the typical $\kappa_w(H = 0) = 598.03 \text{ mW m}^{-1} \text{ K}^{-1}$ to $\kappa_w(H = 80 \text{ kA/m}) \approx 1800 \text{ mW m}^{-1} \text{ K}^{-1}$ as shown in Fig. 17.

2.3.3 Surface Tension

Around 1870, Carlo Marangoni [68] described the physical principle according to which a net movement of mass from a region with higher to a region with lower surface tension takes place. In principle, assume to deal with a rectangle parallelepiped volume of colloid and assume to divide this volume in two parts in the middle of its thickness with a perforated sheet. If the two interface have the same surface tension no particle has any reason to move from its position, in absence of any other phenomena. Instead, if the two sides of this interface have a different tension, a force gradient take place and the particles tend to move toward the side with lower tension. This phenomenon is typically tied to a density gradient. In the work of Kemkar *et al.*[69], where a structure similar to the one we designed and shown in Fig. ?? has been simulated, it is shown that splitting the whole volume of FF with a perforated wall a temperature difference between the two portion of fluid is built up. This influences the surface tension and consequently a mass transfer across the interface results. In particular, the part with higher surface tension will pull more strongly thus the fluid will flow away from low surface tension regions. Because of the role played by the temperature, this effect is often referred to as **thermo-capillary** or **Benard-Marangoni** convection. It has to be noticed that also the concentration gradient will influence this net mass flux.[70]

Having discussed previously the thermo-phoretic effect and magnetic force on the single particle, it is known that the particle will tend to move toward warmer or colder regions forming a concentration gradient. This, summed with the different temperature of the fluid portions, makes it evident that the particles have to be chosen appropriately, i.e. their nature (thermophilic or themophobic) has to be carefully investigated since the two effects can be either directed on the same verse or opposite.

Once the concentration gradient ($\nabla\varphi$) rises, the steady concentration can be derived by means of balance of forces, accounting for the Brownian motion and friction force. For sake of simplicity, a one-dimensional treatment considering only x -axis

is presented here and the surface tension σ can be expressed as:

$$\frac{d\sigma}{dx} = \underbrace{\frac{d\sigma}{dT} \frac{dT}{dx}}_{\text{Temperature}} + \underbrace{\frac{d\sigma}{d\varphi} \frac{d\varphi}{dx}}_{\text{Concentration}} \quad (87)$$

where the chain rule has been exploited. For non-magnetic substances, the second term can be neglected as done for the early treatment of this effect by Fedosov in [71]. Here, assuming a very high aspect ratio, which is not a restrictive condition since in our experimental setup the depth h is taken much smaller than its length l , and neglecting the convective flow, which is proven to be dominated by thermocapillary phenomena in these conditions, i.e. whenever the constraint $h^3 \ll \frac{4\nu^2 \rho l}{|d\sigma/dx|}$ is satisfied, the following expression for the surface tension variation along x -component can be stated:

$$\frac{d\sigma}{dT} = \frac{4\mu h u}{\frac{dT}{dx} (3z^2 - 4hz + h^2)} \quad (88)$$

with u representing the x -component of the velocity vector \vec{v} and $\mu = \rho\nu$ the dynamic viscosity.

As stated in the previous sections, the overall magnetization can be assumed to be linearly dependent on NPs concentration. At steady state the diffusion flux will balance the drift flux leading to:

$$\frac{\partial \varphi(\vec{r})}{\partial t} = \nabla \cdot [\vec{J}_{drift} + \vec{J}_{diff}] = \nabla \cdot [\varphi(\vec{r})\vec{v}_p - D\nabla\varphi(\vec{r})] = 0 \quad (89)$$

with v_p representing the relative velocity of a NP with respect to the carrier fluid which can be easily expressed as linearly dependent on the magnetic force and the mobility η of the particle in the liquid. Manipulating previous expression and using the MMF2 theory¹⁴ to express the magnetization, Eq. 89 can be re-stated as:

$$\frac{\nabla\varphi(\vec{r})}{\varphi(\vec{r})[1 - \varphi(\vec{r})]} = L(\xi)\nabla\xi \quad (90)$$

with $\xi = \frac{M_s V_p B_x}{k_B T}$ representing the ratio of local magnetostatic energy. Integrating this expression, a closed form for the NPs concentration is reached:

$$\varphi(\vec{r}) = \left[1 + \left(\frac{1 - \varphi_b}{\varphi_b} \right) \frac{\sinh(\xi_0)\xi}{\sinh(\xi)\xi_0} \right]^{-1} \quad (91)$$

¹⁴Notice that this theory as the very same formal expression of Langevin's equation but remember that the Langevin's coefficient is changed since it accounts for the effective magnetic field.

where ξ_0 is the ratio of magnetostatic energy of the particle with one in the bulk very far away from the local magnetic field sources and φ_b is the bulk concentration.

Taking as null the magnetic field in point $x = 0$ its x-component, simply by geometric considerations, becomes

$$B_x = B \frac{x}{l}$$

and the final expression for the concentration in x direction is obtained:

$$\varphi(x) \approx \left[1 + \left(\frac{1 - \varphi_b}{\varphi_b} \right) \frac{\xi}{\sinh(\xi)} \right]^{-1} \quad (92)$$

Substituting this result in the empirical formula obtained by Dababneh for Fe_3O_4 -based FFs, it comes out that the surface tension gradient due to concentration can be expressed as:

$$\frac{d\sigma}{dx} = - \frac{0.146 M_s V_p B \varphi^{2.4}}{k_B T l} \left(\frac{1 - \varphi_b}{\varphi_b} \right) \left[\frac{\sinh(\xi) - \xi \cosh(\xi)}{\sinh(\xi)^2} \right] \quad (93)$$

Using Eq. 88 and 93 in Eq. 87 a complete description of surface tension variation is provided.

2.4 Thermomagnetic Convection

The convective movement of the particle of a magnetic fluid in presence of a magnetic field and a temperature gradient is called in literature **Thermomagnetic Convection**. The term advection can also be found sometimes but it is a little incorrect since it seems to refer only to mass, heat or momentum transport while also the diffusion as to be taken into account. This motion arises because of the variation in magnetization level achieved by the temperature gradient, being the magnetic susceptibility a function of temperature:[72]

$$\chi_m(T) = \frac{\chi_{m,0}}{1 + \alpha_T(T - T_0)} \quad (94)$$

with $\chi_{m,0}$ representing the susceptibility computed at temperature T_0 . This provokes a variation in the magnetic force exerted on the particle and the convective motion builds up.

In 1970 the first study on this phenomenon was conducted by Finlayson[45] for ferrofluid systems and the importance of Curie's temperature T_C and pyromagnetic coefficient was pointed out. In fact, the maximum possible variation in the particle

magnetization occurs in the neighborhood of phase transition where the particle passes to have null magnetization. However, the effect is still present even if we are far away from it, as specified in Eq. 94. The theoretical description of thermomagnetic convection has many different forms and the one proposed by Odenbach [39] and Suslov [56] studying a vertical layer of ferrofluid contained between a hot and cold plates is interesting for the similarities with our experimental apparatus. The assumption of steady-state gradient and heating from above are taken as valid and the magnetic field H is applied uniformly to the hot plate establishing a gradient within the fluid. The reader is invited to refer to Fig. 18 to better understand the system's structure.[60]

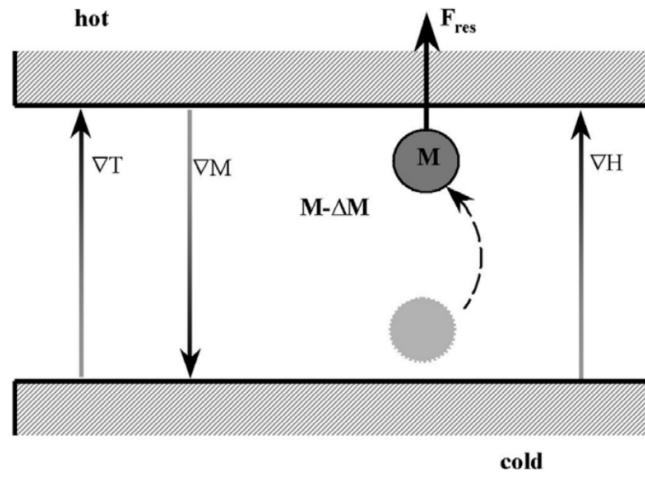


Figure 18: Thermo-magnetic driving mechanism: displacing a portion of volume from a colder to a hotter region, its magnetization will reduce.

It can be written that the force acting on a particle is:

$$\vec{F} = \underbrace{-m_p g \hat{u}_z}_{G \text{ force}} + \underbrace{\mu_0 M \frac{dH}{dz} V \hat{u}_z}_{\text{Magnetic force}} + \underbrace{(\rho - \Delta\rho) V g \hat{u}_z - \mu_0 (M - \Delta M) \frac{dH}{dz} V \hat{u}_z}_{\text{Pressure force}} \quad (95)$$

where the gravitational terms keeps into account the weight of the magnetic particle, the magnetic term the variation of magnetic force due to the gradient of external magnetic field and the pressure term accounts for the density ρ and magnetization intensity M variation due to the thermal gradient. Re-written eliminating the redundant terms, remembering that $m_p = \rho V$, we get:

$$\vec{F} = \left(-\Delta\rho + \mu_0 \Delta M \frac{dH}{dz} \right) V \hat{u}_z \quad (96)$$

It follows from this expression that the particles will experience a displacement

upward only if

$$\mu_0 \Delta M \frac{dH}{dz} > \Delta \rho g$$

meaning that the directions of the magnetic and thermal gradient are very important. Moreover, three observations confirming our previous statements are:

- The intensity of the force strongly depends on ΔM so the higher is the magnetic field the higher the magnetization and consequently the thermomagnetic effect;
- The magnetization needs to be highly dependent on temperature, i.e. the pyromagnetic coefficient needs to be high;
- The buoyancy plays either a destabilizing or a stabilizing role depending on the direction of the temperature gradient. In the treated case it is stabilizing but the opposite occurs if we invert the gradient.

The link between the magnetic field intensity and pyromagnetic coefficient can be proved to be expressed as:[73]

$$H(z) = H_0 + \frac{K}{1+} \frac{\Delta T}{L} z \quad (97)$$

where H_0 is the magnetic field at coordinate $z = 0$.

Furthermore, thermal conduction and viscous forces have always a stabilizing effect since they slow the particle motion. For this reason, the thermomagnetic convection is not always occurring even if we are in presence of micro-gravity. The force applied on the NPs has to be stronger than the stabilizing forces and the dimensionless *Magnetic Rayleigh* number is describing their ratio:

$$Ra_m = \frac{\mu_0 K_m |\nabla H| \Delta T L^3}{\kappa \eta} \quad (98)$$

where K_m in the pyromagnetic coefficient, κ the thermal diffusivity, η the dynamic viscosity and L the thickness of the fluid layer or the distance among the plates.

3 Governing Equations

In this section, a model developed by Giuseppe Fortunato in collaboration with Politecnico di Torino and IIT - Center for Sustainable Future Technologies is presented. Taking into account a large part of the effect described above and adapting some models proposed in literature, he has simulated the main physical quantity of interest in the Colloidal EneRgEtic System (C.E.R.E.S) reactor (presented in subsection 4.1) which are presented in his work of thesis [1]. The first who developed the equation for the ferromagnetic fluid instability, in order to study the critical temperature (T_c)¹⁵ was Finlayson in [45]. Thanks to this model, he was able to determine also that the magnetic force becomes dominant over the natural convection when the thickness of fluid layer is very small ($\approx 1\text{mm}$). The fluid's flow is modeled as multiphase because of its composition. The nano-particles and the solvent can be seen as two systems moving relatively with respect to each other and respect the condition form multiphase system, i.e. two or more phases present in the fluid. Under the condition particles with a finite size ($\approx 10\text{nm}$ in FF), the fluid flow as to be treat as dispersed and not separated. The multiphase treatment can be ran from two different point of view (PoW):

- The observer is in a reference system place outside the flow. By looking at a restrict section of the fluid the streamlines observed and the two phases can be seen as interpenetrating continua. Considering the entire volume divided in several phase streams, we can consider each single unitary volume as occupied by a single phase which takes the name of **volume fraction** α . This allows to obtain a set of continuity equation for each phase describing the fluid flow;
- The observer is in the reference system of a tiny volume of fluid. The single unitary volume considered in this case can exchange energy, mass and momentum with the surrounding fluid. Thus the Navier-Stokes equation averaged in time can provide a good description of the flow under the assumption of homogeneous fluid.

This latter model allows to predict trajectories and it is suitable in all those mixtures having a dominant phase (primary) and secondary phase is negligible. For this

¹⁵The critical temperature is a term used to identify the condition at which the onset of convective motion/instability occur. This has been calculated by Finlayson in two cases: either the magnetic force is the dominant and thus can be considered as the only force acting in the system, or both buoyancy and magnetic force are present

reason, the former approach is preferred. Among the three major models used in literature in the case of Euler-Euler approach, the one adopted in the work is the **mixture model**. Here the phases of the fluid are decoupled at least from speed standpoint since can have different slip velocities and the interpenetrating condition ensures that in each volume fraction their concentration is either 0 or 1.

3.1 Continuity Equation for Mixture

Probably, the most well known properties of the physical systems is that regarding the mass conservation which states that is not possible that a close system varies its overall mass. This law together with previous statement regarding the phase within a volume fraction (only 1 phase present inside the reference volume) makes possible to say that the amount of mass incoming and outgoing the volume is the same. In order to provide a general description, consider the mixture as formed by k phases. The continuity equation is generally expressed in the differential form as

$$\frac{\partial \vec{\rho}}{\partial t} + \nabla \cdot \vec{j} = \sigma$$

where σ typically is null since we have no generation source (i.e. the total mass is conserved). Thus, it is evident that the variation in time of the density is consequent and proportional to the overall flux of substance across the domain's walls. Accounting for all the components of the mixture it can be rewritten as

$$\begin{aligned} \frac{\partial}{\partial t} \sum_{k=1}^n (\alpha_k \vec{\rho}_k) + \nabla \cdot \sum_{k=1}^n (\alpha_k \vec{\rho}_k \vec{v}) &= 0 \\ \frac{\partial \vec{\rho}_m}{\partial t} + \nabla \cdot (\vec{\rho}_m \vec{v}_m) &= 0 \end{aligned} \tag{99}$$

where the notation $\vec{\rho}_m$ and \vec{v}_m has been added for compactness and the subscript m stands for mixtures. The parameter *alpha* identifies the volume concentration¹⁶ which, here, corresponds to the volume fraction.

The same expression can be written also for each single phase of the mixture and strongly simplified under the assumption of constant phase densities and negligible

¹⁶The volume concentration is defined as the ratio among the volume of the constituent of interest (V_i) and the volume of the mixture (V). This differ with volume fraction typically since in this latter we have the sum of all the constituents as denominator. However, by definition, they become equal in ideal solution where $\sum_j V_j = V$.

interphase mass transfer, which are conditions consistent with the hypothesis done so far. To make things clearer, the drift velocity of the k -th phase $\vec{v}_{D,(k)}$ can be written from the center of fraction volume \vec{v}_k standpoint:

$$\vec{v}_{D,(k)} = \vec{v}_k - \vec{j}_m \quad (100)$$

where $\vec{j}_m = \sum_k \vec{j}_k$ represents the volumetric flux of the mixture and, consequently, $\vec{j}_k = \alpha_k \vec{v}_k$. The continuity equation of a single phase thus becomes:

$$\frac{\partial}{\partial t} \alpha_k + \vec{j}_m \cdot \nabla \alpha_k = -\nabla \cdot (\alpha_k \vec{v}_{D,(k)}) \quad (101)$$

where the equality $\nabla \cdot \vec{j}_m = 0$ has been used implying the density ρ is constant in time.

Finally, if only one dispersed phase (1) is present in the mixture, as in the case of FFs, the drift velocity can be rewritten in terms of relative velocities $\vec{v}_1 = \vec{v}_i - \vec{v}_j$ by expanding \vec{j}_m and becomes:

$$\vec{v}_{D,(1)} = (1 - \alpha_1) \vec{v}_1 \quad (102)$$

So the phase continuity equation in this case is:

$$\frac{\partial}{\partial t} \alpha_1 + \vec{j}_m \cdot \nabla \alpha_1 = -\alpha_1 (1 - \alpha_1) \nabla \cdot \vec{v}_1 - (1 - 2\alpha_1) \vec{v}_1 \cdot \nabla \alpha_1 \quad (103)$$

and, for volume fraction α_1 constant, we get

$$\nabla \cdot \vec{v}_1 = 0 \quad (104)$$

This represents the phase continuity equation for multiphase fluids with \vec{v}_1 being a vector with components (u, v, w) representing the three components fluid velocities.

3.2 Momentum equation for the mixture

The momentum is, in general, a conservative quantity, i.e. it doesn't depend on time unless external forces are exerted on the object. In our experimental case, in order to correctly describe the continuity equation for the momentum, we will need to account for both the external and internal forces acting on the control volume, making evident the dependence on time. The former coincides with the volumetric forces present in the system, i.e. external magnetic field applied and gravitation,

which directly impacts on the volume fraction moving across the domain walls, while the second are those forces acting on the volume surface.

In general the rate of change of this quantity in the infinitesimal volume considered is caused by:

- External forces acting on the walls of the volume;
- Unbalance among incoming and outgoing flux of momentum;
- Internal forces acting on the volume

In particular, the main quantity accounted for this treatise are: wave pressure due to magnetic field p , shear and stress due to the slip of the fluid onto the walls. Following Ishii [74] notation, the continuity equation of momentum for the k -th phase can be written, assuming $k = 1$ as:

$$\frac{\partial}{\partial t}(\alpha\rho\vec{v}) + \nabla \cdot (\alpha\rho\vec{v}\vec{v}) = -\alpha\nabla\vec{p} + \nabla \cdot [\alpha(\bar{\tau} + \bar{\tau}_T)] + \alpha\rho g + \vec{M} \quad (105)$$

where $\bar{\tau}$ is the stress tensor in average which accounts for the viscosity of the fluid, g is the gravitational force acting on the particles and the turbulent stress tensor $\bar{\tau}_T$ and the source of momentum \vec{M} are both kept as null because of the system's characteristics. Notice that the quantity $\rho\vec{v}\vec{v}$ is a dyadic product so the output will be a tensor.

According to Eulearian view, the time derivative $\frac{\partial}{\partial t}\alpha\rho\vec{v}$ can be seen as the rate of change with time of a momentum at a fixed point within the reference volume thus, the left side of Eq. 105, represents the rate of change of momentum within the whole volume of fluid which is nothing but the Lagrangian framework. To be clearer, it is about change the point of view from inside the volume, where just the relative motion can be observed, to outside it. This allow us to introduce the Lagrangian time derivative:

$$\frac{D}{Dt} \equiv \frac{\partial}{\partial t} + u\frac{\partial}{\partial x} + v\frac{\partial}{\partial y} + w\frac{\partial}{\partial z} = \frac{\partial}{\partial t} + \vec{v} \cdot \nabla \quad (106)$$

The ferrofluids are considered Newtonian fluids which means that viscous stresses are linearly depend on the local strain rate over time. For this reason, we can express the stress tensor \bar{T} in agreement with [75] where, starting form Cauchy-Poisson

equation, it has been found:

$$\bar{\bar{T}} = -\Pi\bar{\bar{I}} + 2\mu\bar{\bar{\Omega}} - 2\mu\bar{\bar{B}} \quad (107)$$

with $\Pi = p - (\lambda + 2\mu)\nabla \cdot \vec{v}$ represents the isotropic part, $\bar{\bar{\Omega}}$ is the spin tensor, $\bar{\bar{B}} \equiv \nabla \cdot \vec{v}\bar{\bar{I}} - \nabla\vec{v}^T$, $\mu = -(3/2)\lambda$ the molecular viscosity coefficient and λ bulk viscosity coefficient. In this case, neglecting the spin contribution, considering μ as constant, bringing outside the pressure term p and substituting all terms we get

$$\bar{\bar{T}} = \lambda(\nabla \cdot \vec{v})\bar{\bar{I}} + 2\mu\nabla\vec{v}^T$$

Now that we have an expression for the term contained in the momentum equation, we can consider the phase continuity equation $\nabla \cdot \vec{v} = 0$ and five terms can be recognized in the final expression of the Navier-Stokes momentum continuity:

$$\rho \frac{D\vec{v}}{Dt} = -\nabla p + \mu\nabla^2\vec{v} + F_N + F_M \quad (108)$$

where $F_N = -(\Delta\rho)g$ represents the natural convection due to buoyancy and $F_M = F_v$ the magnetic force taken from subsection 2.2.3 and, more precisely, the Kelvin force expressed by Eq. 72. The former can also be expressed in more explicit terms, as did by Suslov in [56], accounting for the thermal expansion in order to make explicit the dependence over temperature T:

$$\rho = \rho_0 - \alpha_T(T - T_0) \quad (109)$$

being ρ_0 the density at $T = T_0$ and α_T the coefficient of thermal expansion.

3.3 Volume Fraction Equation for Particles

In order to provide an explanation to Eq. 73 and give an alternative and clearer form of the flow accounting also for thermophoresis and magnetophoresis, we need start from the general formulation of mass conservation in which the density ρ_s of the solid phase is described in term of volume concentration α_p and its velocity $\vec{v}_s = \vec{v} + \vec{v}_{slip}$ is seen in term of relative motion of the particle \vec{v}_{slip} with respect to the fluid:

$$\left[\frac{\partial\alpha_p}{\partial t} + \nabla \cdot (\alpha_p\vec{v}) \right] = -\nabla \cdot (\alpha_p\vec{v}_{slip}) \quad (110)$$

The inconvenient of this formula is that the solid phase flow (right hand side) is not easily determined. The first who tried to describe the motion of a spherical particle in a uniform and steady flow was Stokes in 1851, under the assumption of low Reynolds numbers (≤ 1). In the following century, Basset, Boussinesq and Oseen (BBO) provided the description for the motion in a inactive fluid and Tchen proposed a treatment for the unsteady and non-uniform flow, but some inconsistencies were found. However, the rigorous description arrived only in 1983 with Maxey and Riley[76] equation. For the sake of order, the typical form, which is nothing but the second Newton's law, is reported here:

$$m \frac{dv_i}{dt} = F_{Buoyancy}^i + F_{FK}^i + F_{ss}^i + F_{AM}^i + F_{Basset}^i + F_{Other}^i \quad (111)$$

with the superscript i indicating the i -th component of a vector, F_{Other} identifies all the other contributions which can be added to the treatment (if needed) and all the other terms are analyzed in the following subsections. In the case represented by our experimental apparatus, the Stokes' number is so low that the particle can be assumed to follow exactly the carrier fluid's streamlines with no inertial effects. Thus, the above expression can be strongly simplified neglecting, without any loss of generality, the *unsteady terms* (see subsection 3.3.3) can be neglected. However, three very important effects in this case, not explicitly accounted in above expression, are *thermophoresis*, *magnetophoresis* and *Brownian motion*. According to the model developed in [1] including these forces in the simplified form of Eq. 111 it can be retrieved:

$$\vec{v} - \vec{u} = \vec{v}_{slip} = \frac{1}{6\pi R\mu_f} [(m_p - m_f)\vec{g} + F_S + F_{MPH} + F_{Brown}] \quad (112)$$

with \vec{v} and \vec{u} the particle and fluid velocity, F_S and F_{MPH} having the form of Eq. 42 and 76, respectively while

$$F_{Brown} = -D\nabla\varphi_p$$

with D diffusion coefficient given by the Einstein formula and φ_p volume concentration of particles. Substituting in the above equation and manipulating it in order to express the volume fraction equation in term of solid phase rate of transfer $\dot{\varphi}$ we get:

$$\left[\frac{\partial\varphi_p}{\partial t} + \nabla \cdot (\varphi_p \vec{v}) \right] = \frac{(m_p - m_f)\vec{g}}{6\pi R\mu} \nabla\varphi_p + S_T D \nabla \cdot (\varphi_p \nabla T) - Q \nabla \cdot (\varphi_p \nabla H) + D \nabla^2 \varphi_p \quad (113)$$

3.3.1 Buoyancy and Froude–Krylov force

Since the left-hand side of above equation is exactly equal to the general formulation of dynamic's second law, the analysis begins from the first term in the right-hand side. Here, the body force acting on all the solid phase suspended is represented by an upward force opposite to the weight of the particles themselves. It corresponds, according to Archimedes' principle, to the net weight difference, i.e. to the difference among the weight of the particle (m_p) and the one of the displaced fluid (m_f). Thus, it can be described by:

$$\vec{F}_{Buoyancy} = V_p (\rho_p - \rho_f) \vec{g} = (m_p - m_f) \vec{g} \quad (114)$$

where V_p is the particle volume and $\rho_{p(f)}$ represents the particle (fluid) density.

The second term in literature is named **undisturbed**, or unperturbed, flow and is an extension of **Froude-Krylov** force present in BBO equation. It represents an hydrodynamic force due to pressure and shear stress fields under the undisturbed flow conditions¹⁷. The pressure wave enforce an acceleration to the particle according to:

$$F_p^i = - \int_{\Sigma} p \hat{n} d\Sigma = - \int_{\Sigma} \frac{\partial p}{\partial x_i} dV_p \quad (115)$$

where the superscript i identify the i -th component of the force, \hat{n} is a unitary vector perpendicular to particle's surface and the divergence theorem has been exploited. Assuming the pressure gradient constant the integral can be easily solved resulting in:

$$F_p^i = -V_p \frac{\partial p}{\partial x_i} \quad (116)$$

A further contribution that has to be accounted for is the one of shear stresses which has similar expression with the pressure and can be easily manipulated to get:

$$F_{\tau}^i = \int_{\Sigma} \tau_{i,j} \hat{n}_j d\Sigma = V_p \frac{\partial \tau_{i,j}}{\partial x_j} \quad (117)$$

in analogy with the previous result, where subscript j spans over the three coordinates and the divergence theorem step is not reported. So we can conclude that this term

¹⁷The condition of unperturbed flow means that the whole particles are assumed to be still in order to avoid the effect of their relative motion on the evaluation of the viscous forces acting on them. In practice we are focusing only on one particle moving because of pressure gradient and the inertia effect is characterized.

will take the form:

$$F_{FK}^i = F_p^i + F_\tau^i = V_p \left(\frac{\partial \tau_{i,j}}{\partial x_j} - \frac{\partial p}{\partial x_i} \right) \quad (118)$$

3.3.2 Drag Forces

As the solid phase dispersed in the carrier fluid moves of relative motion with respect to it, inevitably a resistance which tends to recover steady state equilibrium builds up. This force is opposed to motion and in literature it usually takes the form of Stokes drag force. However, this latter doesn't take into account the presence of the wall or, as in colloids, of the surrounding particles. For this reason, it is more correct for a rigorous description to introduce the *Faxen* force described by:

$$F_{Faxen}^i = \mu_f \pi \frac{d_p^3}{8} \nabla^2 \vec{v}_i \quad (119)$$

with μ_f dynamic viscosity of the fluid, d_p is the particle diameter and the subscript i identifies the i -th component of the velocity vector \vec{v} .

Consequently, a simple sum of this correction and the well known Stokes' law gives us the overall *steady-state* drag force:

$$F_{ss}^i = 3\pi \mu_f d_p (\vec{v}_i - \vec{u}_i) + F_{Faxen}^i \quad (120)$$

where \vec{u} represents Eulerian velocity of the particle while \vec{v} the Lagrangian one¹⁸. Generally, the drag coefficient is a function of both shape and orientation of the particle, even if this latter is not important in the spherical case. As mentioned in the thermodynamic section, many parameters are used in order to characterise the flow. The two most important are:

- **Reynolds number:** it is defined as the ratio among inertial and viscous forces:

$$Re = \frac{\rho_f d_p \langle \vec{v} \rangle}{\mu_f} \quad (121)$$

with ρ_f fluid density and $\langle \vec{v} \rangle$ is the average velocity of the particles. It can be deduced from this definition that whenever Re is small (< 1) the inertia effect

¹⁸With Eulerian velocity it is to be understood the velocity measured from a reference system fixed in a point in space during time while Lagrangian is that measured following a stream (a specific volume of fluid) along its trajectory through space and time.

is negligible and the flow is said to be in *Stokes regime*, leading to some simplification in the Navier-Stokes and in the description of pressure gradient.[74] In our experimental apparatus, from the simulation, the Re number results to be ≈ 220 thus no formulation exists for such relatively high number¹⁹ since the increase of the **drag coefficient** (C_D) after a certain Re value is negligible and it can be fixed at $C_D \approx 0.445$

- **Stokes number:** more significant for such experiments since it is defined as the ratio among a characteristic time of a component and the one the flow:

$$St = \frac{\tau v_0}{D} \quad (122)$$

where τ is the characteristic relaxation time of a particle, i.e. the time constant characterizing the frequency response of a linear dynamic system, v_0 is the modulus of the velocity away from the obstacle and D is the obstacle dimension. Thus it can be seen that when St is small ($\ll 1$) the particles will follow the streamline of the carrier fluid. In our case, $St \approx 8 \times 10^{-12}$ so inertia effect can be neglected.

Thanks to this observation, we can say that the drag forces, as well as the inertia one, are not playing a very important role and can be neglected in our specific system (as we will see later on).

3.3.3 Unsteady forces

The two final terms of the volume fraction equation are both belonging to the group of **unsteady forces** which are temporarily amplitude varying stresses. The two terms belonging to this set are:

Added Mass Effect: imagine a rigid sphere thrown into a fluid. The motion of the particle will provoke the displacement of the fluid surrounding its surface. Thus, the fluid will suffer a relative acceleration in the opposite direction with respect to the sphere lowering the body's kinetic energy. However, since the body and the fluid cannot occupy simultaneously the same volume, the overall displaced fluid will be different than the actual volume of the sphere, which justify the name **added** or **virtual** or **apparent** mass effect typically used in literature. Formally, the kinetic

¹⁹The model proposed by Oseen in 1910 is valid only for Re number up to 5.

energy of the body can be described as:

$$E = \frac{1}{2} \rho_f \int_{V_f} \vec{v}^2 dV \quad (123)$$

where V_f is the fluid volume and \vec{v} is the velocity. This latter, under the assumption of incompressible and non viscous fluid, can be seen as the gradient of a potential function:

$$\vec{v} = \nabla \Phi \quad (124)$$

Φ in these conditions can be expressed as:[74]

$$\Phi = -\frac{v d_p^3}{2r^2} \cos(\theta) \quad (125)$$

where v is the modulus of the velocity, r is the distance to the particle and θ the angle formed between \vec{r} and \vec{v} . By substituting Eq. 124 and 125 in 124 a new form for the kinetic energy is found:

$$E = \frac{\pi \rho_f d_p^3 v^2}{3} \quad (126)$$

Now the rate of work needed to change the kinetic energy, given by

$$v F_{AM} = \frac{dE}{dt}$$

can be expressed as:

$$\vec{F}_{AM} = \frac{2\pi \rho_f d_p^3}{3} \frac{d\vec{v}}{dt} = \frac{M_f}{2} \frac{d\vec{v}}{dt} \quad (127)$$

where M_f is the mass of displaced fluid. Notice that this is the force that the sphere applies on the fluid so lies along the same direction of the body velocity.

Basset Force: this term account the unsteady viscous force provoked by the delay in profile development of the fluid with respect to the relative acceleration of the particle. Practically, in contrast to a particle moving of uniform straight motion, an accelerating particle will have a larger friction with in the boundary liquid. For this reason, this parameter is said to account for the history of the system and is also linked to the inertia of the fluid.

Lets consider a flat plane accelerated to a velocity u_0 impulsively and normally to the free surface of the fluid. The equation describing the motion of the displaced

fluid is:

$$\frac{\partial u}{\partial t} = \nu_f \frac{\partial^2 u}{\partial y^2} \quad (128)$$

with y indicating the direction parallel to the free surface of the fluid, u fluid velocity, and ν_f kinematic viscosity. It can be proved that assuming as boundary condition the suitable

$$\begin{aligned} u(0, y) &= 0 \\ u(t, 0) &= u_0 \\ u(t, \infty) &= 0 \end{aligned}$$

the solution of Eq. 128 is:

$$u = u_0 \operatorname{erf} \left(\frac{y}{2\sqrt{\nu_f t}} \right) \quad (129)$$

and the local shear stress (τ) can be modeled assuming to break the acceleration experienced by the plane in a series of steps of duration Δt associated to the relative velocity variation Δu_i . [74] Since the time interval is arbitrary, we can assume it close to zero and express τ as an infinite sum of instant:

$$\tau = \sqrt{\frac{\rho_f \mu_f}{\pi}} \int_0^t \frac{1}{\sqrt{t-t'}} \frac{du}{dt'} dt' \quad (130)$$

Making the same reasoning for a sphere in a liquid, Basset found that the drag force due to viscous effect is expressed as:

$$F_{Basset}^i = \frac{3}{2} d_p^2 \sqrt{\pi \rho_f \mu_f} \left[\int_0^t \frac{1}{\sqrt{t-t'}} \frac{d}{dt'} (u_i - v_i) dt' + \frac{u_{0,i} - v_{0,i}}{\sqrt{t}} \right] \quad (131)$$

where u_i and v_i are the i -th component of fluid and particle velocity. The last term in the squared brackets has been introduced by Reeks and McKee to take into account also the initial velocity.

3.4 Energy Equation For Mixture

The last equation needed in order to determine the NPs motion is the continuity equation for the heat flux, i.e. a relation among the mass displacement provoked by this latter and the temperature gradient imposed. Thanks to the fact the Stokes number is very low but considering the fact that the imposed gradient can be high enough to make inertia effect not completely negligible, the Boussinesq approximation, stating that the density factor can be ignored in each term except when it is

multiplied by \vec{g} , can be considered valid. Practically, this assumption tells us that the variation in density due to whatever effect are not influencing heavily the inertia of the system but the weight difference among two volumes of fluid is strongly evident. This allows also to assume the specific heat capacity c_p constant and express the heat flux as a function of the thermal conductivity of the particle. In other words, it is assumed that the heat path is a sort of percolation through the particles and thus the heat flux \vec{Y} is equal to the specific rate of heating of the particle:

$$-\nabla \cdot \vec{Y} = \rho_p c_p \frac{DT}{Dt} \quad (132)$$

with ρ_p particle density. Now, expressing explicitly the Lagrangian derivative and remembering that

$$\vec{Y} = -\kappa \nabla T$$

where κ is the thermal conductivity, it can be rewritten the final form for the mixture energy equation:

$$\frac{\partial T}{\partial t} + \vec{v} \cdot \nabla T = \frac{\kappa}{\rho_p c_p} \nabla^2 T \quad (133)$$

where the first term is indicating the temporal variation of the temperature, the second is the so-called **advection** term, with \vec{v} particle velocity, and the right-hand side represents the heat flux carried by the particles.

4 Experimental Setup

The aim of this thesis is the development of a new experimental setup for the characterization of pyroelectric and inductive effect for ferrofluid coupled with a suspension of Barium Titanate (BT) nanoparticles. In the first part, I present the previous prototypes proposed at the beginning of this research followed by the cell (see subsection 4.1.3) designed for this goal. Then, the apparatus used and analysed here to confirm the contribution to current and voltage generation given by BT, is presented in subsection 4.5.

4.1 Prototypes

The core of this project is the **C.E.R.E.S** system. This acronym states for **Colloidal EneRgEtic System** and indicates the reactor created to exploit thermo-magnetic coupling to induce the fluid motion. This will be successively harvested adapting correctly the extraction system (coil or electrodes). The idea comes from the **DOUGHNUT**, i.e. **aDaptive cOlloidal accUmulatinG Harvesting UniT**, a term used to indicate all those systems able to exchange only electromagnetic or thermal energy with the surroundings using as mean a colloid in a container acting also as protection.

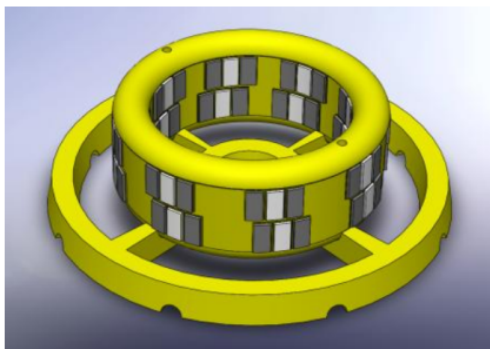
The overall apparatus has been thought to provide a good method for energy harvesting and supply for the **Colloidal Autonomous System (CAS)**, i.e. a colloidal device able to work in an autonomous way typically known as **soft-robot**. In particular, it rises from the challenge proposed by NASA "Surviving Extreme Space Environment"[77] whose goal is to define the most efficient structures and materials for CAS. Moreover, it provides a breakthrough for more common electronic application. In fact, the possibility to harvest energy from every source of heat, even at low temperature, makes evident the possibility to revolution the energy storage of electronic devices.

All the designs, proposed in the following, were produced using a solid modeling computer-aided design and engineering (CAD/CAE) program called **®SolidWorks** and produced by means of *Additive Manufacturing* (AM), a very well known technique nowadays in the field on Industry 4.0. This latter consists in the addition of material in contrast to the most common removal methods which treat to begin from a bulk material and remove part of it.

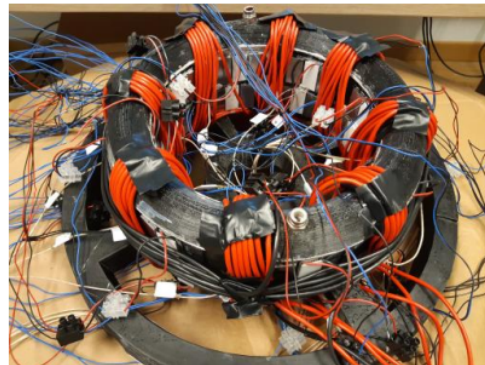
4.1.1 CERES 1.0

The first prototype proposed for the recovery of wasted heat is presented in Fig. 19. It is composed by two parts: the base and the body. This latter is the actual ferrofluid "container" where the thermo-magnetic coupling occur. On the lateral surface are placed the permanent magnets (grey rectangles) and the Peltier modulus (white rectangles), which are needed to simulate the working condition. On the final system, only the magnets will be present since the heating will be provided by other sources. The shape has been chose toroidal-like because of different reasons:

- It allows to easily splice the system onto a pipe;
- It allows to create a smaller cylinder to splice it onto smaller pipes and couple it with some metallic circular sector which provide non-uniform heating to the structure;
- It is a periodic structure, i.e. it is easier to simulate since is sufficient to take into account just one single module (see [1]);
- Such structure allows continuities in the motion along the toroidal axis, thus a preferential direction of motion can be set;
- The lateral walls have been made vertical, differently form the classical toroidal shape, for simplicity of production by AM, in particular by Fused Deposition Modeling (FDM) which gives the possibility to directly create the structure from a CAD design.



(a) Design with ©SolidWorks.



(b) Real prototype with coils of wire.

Figure 19: C.E.R.E.S. system prototype 1.0: the grey rectangles indicate the magnets whereas the white ones the Peltier modulus. Notice that the one reported the configuration of magnets reported in this figure is just one of the possible since they can be displaced on will. The coils of wire in the real prototype are used for electromotive energy harvesting.

The base is a circular support structure provided of lodging both above, to guarantee tightness to the structure, and below, to allow passage of thermocouples and power

cables. The material chosen for both the part composing this apparatus is polylactic acid (PLA) which is suitable for 3D print. The dimensions are reported schematically in Tab. 5.

Parameters	Size [mm]
External Radius	140
Internal Radius	110
Height	85
Width	20
Wall Thickness	5
Lid Curvature	20

Table 5: Dimensions of CERES prototype 1.0.

4.1.2 CERES 2.0

The second prototype, also called **CERES 2.0**, has been produced following the same logic of previous model. The toroidal-like shape has been preserved as well as the dimensions of the chamber. The support have been adapted to the new apparatus in order to provide stability and the prototype has been realized again by means of 3D print but this time *Borosilicate glass* has been used. The PLA has been substituted to gain the transparency provided by Borosilicate glass which allows to perform optical observation. In fact, the idea is to use tracers, like mica powder, to follow the thermomagnetic motion in order to compare them with the simulations. Moreover, the motion observe in several papers [56, 39] could be confirm and visually investigated.

The real prototype is reported in Fig. 20 where it can be noticed that no peltier modulus or magnet has been place on the external wall. The reason lies in the will to make easier the visualization and to create a non-homogeneous magnetic field.

4.1.3 Chamber for Tests

Previous prototypes were designed with the idea to recover electric energy only from the thermo-magnetic motion of the ferrofluid, induced by the coupling among the magnetic field and the thermal gradient, by means of the coils of wire as observed in Fig. 19. In order to enhance the efficiency of current/voltage production, and consequently the device performances, further physical effects need to be exploited.

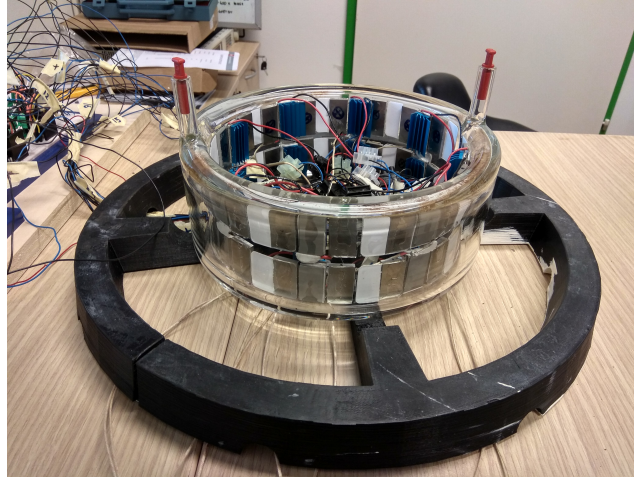


Figure 20: *Second prototype of C.E.R.E.S. system (2.0). The two extensions above the toroid are the pipes used to fill and empty the chamber.*

Since the idea is to work with nanoparticles moving in a carrier fluid and subjected to a thermal gradient, the two most suitable effects to be implemented in the systems are triboelectricity and pyroelectricity. In fact, the former will allow us to extract electric energy by the NPs motion, in particular by their crawling onto a material, whereas the second exploits the temperature variation in time experienced by them to create, and successively harvest by means of electrodes, a pyroelectric charge onto their surface. However, these effects cannot be implemented when the only components of the colloids are kerosene and magnetite since Fe_3O_4 does not develop neither tribo- nor pyro-electric charges. Thus, the approach that will be followed in the future will be to find suitable nanoparticles, like titania and BT, that can be added to the ferrofluid in order to create a colloidal mixture able to exploit many physical effects for current/voltage generation.

The reader is invited to notice that finding nanopowders able to accomplish these tasks and to be easily dispersed in ferrofluid is not an easy task since the interaction with both the carrier fluid and the magnetite needs to be accounted in order to prevent flocculation and agglomeration. Moreover, the Stokes number of all the nanopowder used in the colloidal mixtures needs to be very small in order to ensure that the particles will follow the streamline of the ferrofluid. A further factor that must be taken into account is the need for surfactants to keep them suspended in the carrier fluid. This would reduce strongly the charge transfer and the tribocharging limiting the efficiency of the system. A possible solution could be designed active surfactants able to avoid the reduction of charge transfer.

Barium Titanate has been chosen as pyroelectric material because of its physical

properties. It has a perovskite structure, represented in Fig. 21, i.e. a chemical formula of the form ABX_3 where X represents the oxide (red spheres), B the titanium (white spheres) and A the barium (blue spheres).

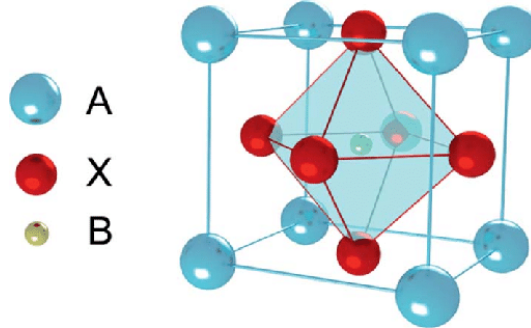


Figure 21: Schematic representation of a Perovskite structure of the form ABX_3 .

In particular, the nanoparticles chosen for these experiments were tetrahedral, quasi spherical and with a diameter $D = 500$ nm. It is a dielectric material with very high relative dielectric constant reaching 15000 for specific temperature ranges. Its biocompatibility makes BT suitable to be used also for wearable applications since it shows no risk for the health. Barium titanate not only allows to introduce a new source of energy recovery but should also bring a contribution to the electromotive force (FEM). In fact, it has been shown in literature that BT has a ferromagnetic effect so the magnetic flux variation, and thus the FEM, should be enhanced allowing higher inductive energy recovery from the coil of wires.[78] However, its contribution is so low that should result negligible with respect to the magnetite one but interactions among these two components of the colloidal mixture have to be taken into account.

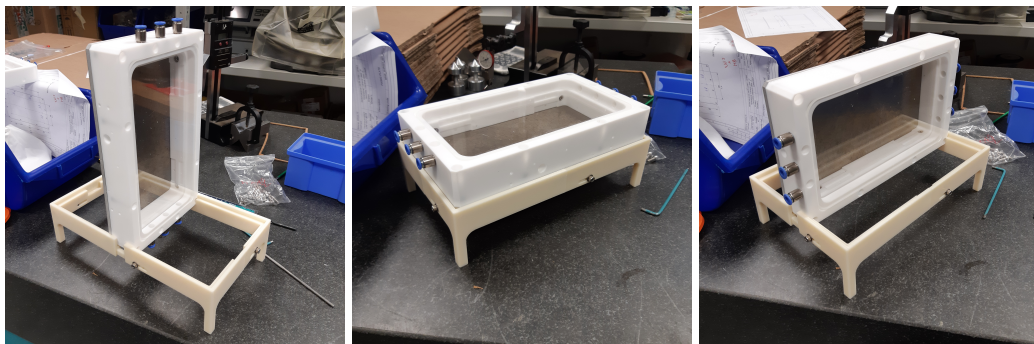


Figure 22: Cell for visual observation of thermo-magnetic motion and pyro/tribo-electric characterization of colloidal mixture.

The cell presented in Fig. 22 has been designed in order to perform visual observation of thermo-magnetic coupling and the consequent NPs motion and to study the effective contribution in energy recovery obtained inserting different powders in

the colloidal mixtures. For these reasons, borosilicate glass has been again adopted for the top and bottom surfaces of the cell, because of its transparency, whereas the lateral frame, confining the mixture, is in teflon. The reason for this choice lies in the triboelectricity it is able to develop with a large range of materials like titania. The three pipes in the upper (and lower even if they are not evident from the pictures) part of the chamber are used to fill and empty the chamber. On the lateral frame instead, several holes can be noticed. Some of them are needed to seal the chamber avoiding losses, thanks to the help of a rubber gasket and some screws. The other instead are apt either to host the thermocouples, which are placed in correspondence of the electrodes, or to host the ultrasonic velocity profiler (UVP) needed to analyse the fluid motion profile.

The possibility to position the chamber in different ways and to change the teflon frame allows both to compare different arrangement of magnetic, thermal and gravity forces and to investigate the influence of the chamber thickness on the fluid motion. Moreover, a further wall, dividing the chamber in two equal regions connected only by two holes in its upper and lower part, will be added to investigate the possibility to exploit the thermophobicity of the nanoparticles to create a tension gradient which contributes to set the convection in a preferential direction. Probably, non uniform heating will be needed in order to accomplish this task.

4.2 Peltier Modules

In order to provide heat to one of the two walls of the chamber and built up a thermal gradient on the fluid, thermoelectric generators can be used. The **Peltier modulus** are all-solid-state devices formed by many p-n junctions, also called *legs*, of antimony telluride (Sb_2Te_3) and bismuth telluride (Bi_2Te_3). These two material have high zT figure of merit, a figure of merit that depends on the electrical σ and thermal κ conductivities of the sample and the Seebeck coefficient S according to the expression:

$$zT = \frac{S^2 \sigma}{\kappa} \quad (134)$$

It is used to indicate efficiency of thermocouples and thermoelectric generators, or in other words, the intensity of Seebeck or Peltier effect, which are opposite phenomenons. In the first case, a conductor having the two ends at different temperatures provokes the electron/hole generation in the hot region and recombination in the cold one with the consequent creation of a potential difference. The second effect instead states that if a potential difference is applied to a material, a temperature

gradient builds up consequently to the carrier motion.

Thus, a high zT value means that, even at low currents, the gradient of temperature they are able to develop among their extremities is quite high. The modulus used in laboratory are 15mm large and 30mm long with an overall thickness (ceramic plates and legs) of 3mm. For sake of completeness they've been reported in Fig. 23



Figure 23: Peltier modulus with dimensions $15 \times 30 \times 3$ mm

The maximum temperature reachable with these modules was around 70°C since the contact between the ceramic plate and the reactor's walls was limited by the shape and higher temperature end to produce melting of the legs junctions. Until now they have been powered by 12 V power generator with two steps of reduction in order to provide a final tension to the modulus around 2.3 V. However, in the future a Peltier Array Controller (PAC) will be used to power them allowing a precise control on the temperature and the heating distribution since it allows to control each module autonomously. It will also allow to acquire data from the thermocouples whose data will be used to continuously monitor the right heating level provided by each Peltier. Thus a real time modification of the voltage applied to each module will make possible to provide a uniform heating as desired.

4.3 Magnets

The magnetic field contributing to the creation of thermo-magnetic motion of the NPs, is create by placing on the outer wall permanent magnets. It is worth notice that to guarantee a long life to the device, in the concept of create an autonomous unit, permanent magnets with good resistance to demagnetization at working temperature.

For this reason, assuming to work in low-grade waste heat range, an alloy of aluminum, nickel and cobalt, known as **ALNICO**, represent the best choice. They are reported in Fig. 24 and the dimension are exactly the same of Peltier modulus ($30 \times 15 \times 3\text{mm}$).

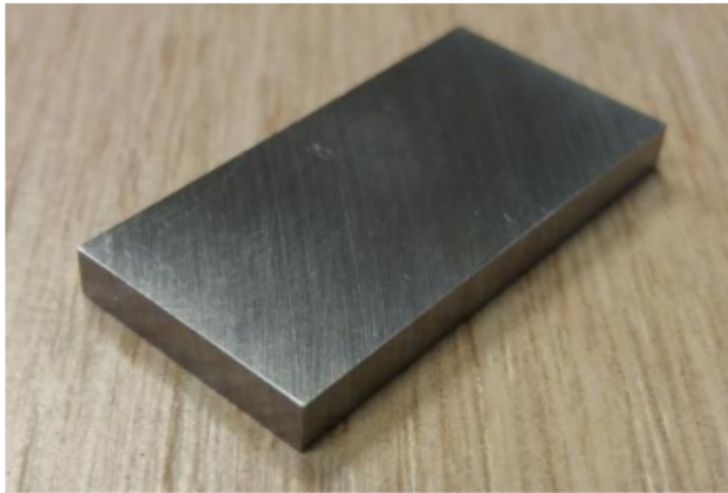


Figure 24: Aluminium (Al), Nickel (Ni), Cobalt (Co) alloy (ALNICO) permanent magnet with dimension $15 \times 30 \times 3\text{mm}$.

Different kinds of magnetization are available in order to test the different configuration among ∇T and \vec{H} .

In particular, in these experiments two layers formed by three rows of magnets have been used. Two of these stacks were placed at the two end of the experimental apparatus presented in section 4.5.

4.4 Sonicator

The **sonicator** is a system composed of three main parts, also reported in Fig. 25:

- The ultrasonic electric **generator** converts the AC current to high frequency electrical energy;
- The **converter** collect the energy coming from the generator and, by means of a piezoelectric element, convert it in mechanical vibrations;
- The probe, also known as **horn**, is the ending part of the instrument. Its aim is to amplify the vibration provided by the converter and transfer them to the sample. It can be of different dimensions and length, according to the need.

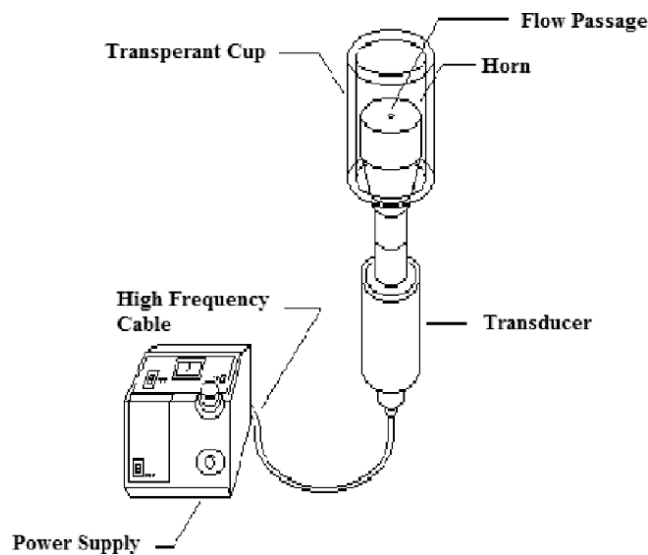


Figure 25: Cup horn sonicator (CHS) schematic representation.[79]

The rapid vibration of the horn provokes the formation of micro-bubbles in the fluid which successively collapse releasing very high energy. This phenomenon is known as **cavitation** and it can be controlled by appropriately setting the power of the generator. The sonication can be either **direct**, meaning that the tip is inserted in the sample, or **indirect**, where the probe is not in contact with the sample since the vibration are transferred to the sample by the water. This latter is also known as **ultrasonic bath**.

In this case, for the dispersion of BaTiO₃ in ferrofluid, the direct kind was used and the power has been set to 40% of its maximum power for an effective working time of 20min. In particular, 10s of activity were followed by 10s of inactivity to ensure good mixing.

4.5 Apparatus

As a conclusion of this overview on the prototypes designed during the project, a schematic representation of the experimental apparatus used to investigate the pyroelectric contribution to the energy recovery is presented in Fig. 26. Here it can be noticed that different pipes were used because of the need to connect the pipe of the peristaltic pump (reported in Fig. 27) whose external diameter is $d_e = 4$ mm to the pipe in teflon whose $d_e = 12$ mm.

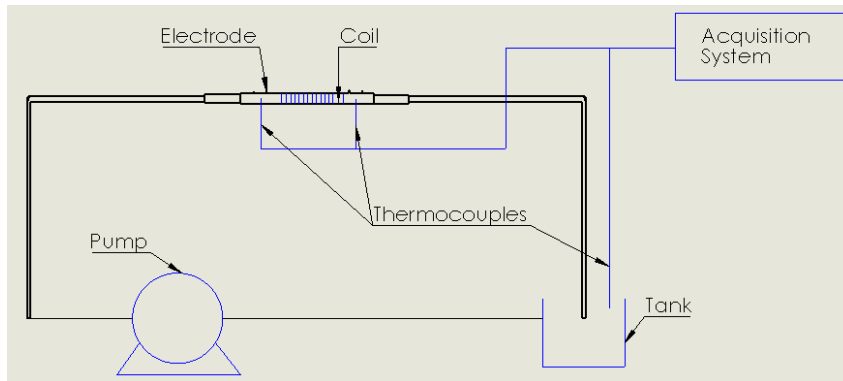


Figure 26: Schematic representation of the experimental apparatus obtained by ©SolidWorks.

To achieve this, different junctions were used as well as other two intermediate pipes with $d_e = 7$ mm and $d_e = 10$ mm, respectively.



Figure 27: Peristaltic pump needed to force the fluid motion.

The tank is a becher filled with a sufficient amount of colloidal mixture to fill all the system. This is placed onto a magnetic stirrer (see Fig. 28), provided of an heating plate, which allows to both maintain the mixture in agitation and heat it on will.



Figure 28: Digital magnetic stirrer with thermal plate.

The thermocouples (TCs) are type N and have been calibrated before starting the acquisition by means of LabView software. This was used to control the Data Acquisition (DAQ) system apt to the collection of data form the three TCs: one monitoring the mixture temperature in the becher and the other two the one of the fluid in correspondence to the electrode.

Concerning the extraction system, i.e. the system apt to the recovery of pyroelectric charges and to the harvesting of electromotive force, two titanium electrodes and a coil of wire have been used. In Fig. 29 the picture of one electrode in the tube is

reported to give an idea of the structure.



Figure 29: Electrode in the tube fixed with hot glue to avoid motion and fluid losses.

The titanium is a very good conductor and, since the system composed by these two plates and the column of dielectric fluid in between, it will probably behave like a capacitor. They have been obtained cutting a titanium foil of thickness 0.25 mm in two stripes 5 cm long and 0.5 cm wide. However, the reader is invited to notice that the part of electrode submerged, i.e. the part in contact with the fluid, is only 3×0.5 cm since the extreme part of each side as been used to fix it. The first electrode, term with which is indicated the electrode closer to the pump, is placed at a distance $l_4 = 2$ cm from the beginning of the central pipe and the second at 15 cm after it. The capacitive analysis performed on them has been achieved by the use of a source meter 2635A by Keithley (see Fig. 30a) and LCR E4980A by Agilent (see Fig. 30b).



(a) Source meter 2635A by Keithley, used to measure current and voltage of the electrodes.



(b) LCR E4980A by Agilent used for impedance measurements of coil and electrodes.

Figure 30: Measurements systems for inductive and capacitive analysis.

Concerning the coil of wire, it is composed by $N = 80$ winding disposed on two layers in order to enhance the electromotive force. Its overall length is 14 cm and the section of the wire used is 3.5 mm which is quite thick meaning that the resistance will be quite low. The inductive measurement where done again by means of the LCR-meter in order to give an estimation of the influence on the inductance of the fluid motion, allowing an estimation of the power produced.

For the sake of completeness, Fig. 31 has been reported in order to show the real experimental apparatus assembled in laboratory. Here the components shown before have been arranged on order to occupy the smallest space possible to reduce the travel performed by the fluid.



Figure 31: Picture of the real experimental setup created in laboratory.

The last component of the circuit are the magnets placed in correspondence of the coil of wire ends as sketch in Fig. 32.

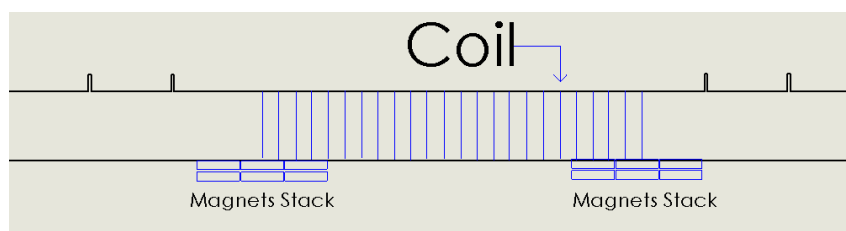


Figure 32: Scheme of the magnet position in the real apparatus

They have been oriented according to the fluid flow, meaning that the southern pole S is the first encountered by the nanoparticles. To better understand the field distribution, the magnetic intensity has been acquired by means of a gaussmeter. The data have been successively exported in MATLAB where the field has been

reconstructed (see Fig. 33). This could be useful in a future to build a model that, accounting the magnetization variation and consequently the magnetic flux, confirm the electromotive force measured during the inductive analysis.

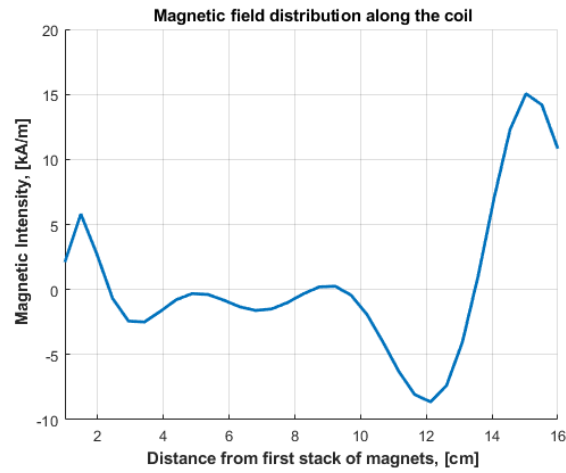


Figure 33: Magnetic field distribution measured by the gaussmeter and plotted with ©MATLAB.

5 Results And Discussion

In this section the results obtained from the experimental apparatus presented in subsection 4.5 are analysed and discussed. The main goal is to experimentally prove the presence of the pyroelectric effect and its effective contribution to the current and voltage generation in a colloid based on ferrofluid and barium titanate. The idea is to successively include this effect in the CERES reactor thus improving its energy harvesting efficiency.

5.1 Circuit Analysis

The first operation is the analysis of resistance (R) and reactance (X), i.e. the real and imaginary part of electrode and coil impedance, in a situation with just air inside the pipe. For this goal, an LCR-meter (see Fig. 30b) controlled remotely by LabView, which allows to perform sweeps in frequency from 20Hz to 2MHz, has been used. This operation is needed to observe the behaviour of these components and associate it to an equivalent circuit.

First test: capacitive analysis of titanium electrodes in air condition

In electronics, different representations can be exploited to characterize a circuit but the most common one is the **Bode Plot**. This is a parametric plot used to describe the response in frequency of a system, i.e. the parameter of interest, converted in dB, are represented as a function of logarithmic frequency. In Fig. 34 the electrode's impedance modulus is reported: it can be observed the presence of a pole and a consequent linear decrease (notice the double logarithmic scale) with an inclination of -20dB/dec which indicates that the component, in that range of frequencies, behave exactly like a capacitor according to the expression

$$X_C = \frac{1}{j\omega C} \quad (135)$$

with ω pulsation and C capacitance.

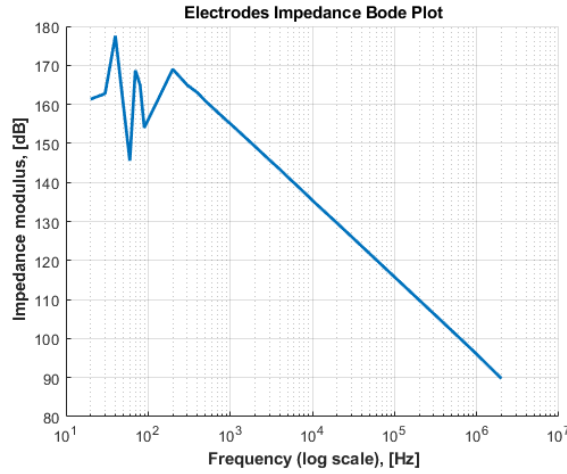


Figure 34: Titanium electrodes impedance modulus in air conditions as a function of frequency.

Moreover, the fact that at low frequencies it doesn't diverge toward infinity indicates the presence of a resistance in parallel with the capacitor. Thus the equivalent circuit will be represented by Fig. 35, having a resistance that can be estimated from previous figure assuming as linear the part before the cutoff frequency $f_c = 200\text{Hz}$.

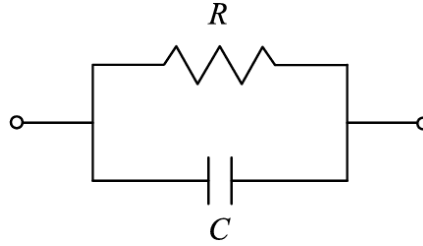


Figure 35: Equivalent circuit of the titanium electrodes.

The total impedance Z_e of the equivalent circuit is given by the expression:

$$Z_e = \frac{R}{1 + j\omega CR} \quad (136)$$

where j indicates the imaginary unit and ω the frequency of interest. Since the root mean square voltage, i.e. the equivalent DC value of an AC signal in a period, used to perform the analysis has been set to $V_{rms} = 1\text{V}$ in this case, the power that is extracted from this circuit can be estimated by:

$$P_e = \frac{V_{rms}^2}{|Z|} = \frac{V_{rms}^2 \sqrt{1 + (\omega CR)^2}}{R} \quad (137)$$

where the subscript e indicates the electrodes. This calculus implies the knowledge

of circuit parameters which can be analyzed observing the two part of the impedance separately. For these reasons, in Fig. 36 the resistance and reactance Bode plots are reported.

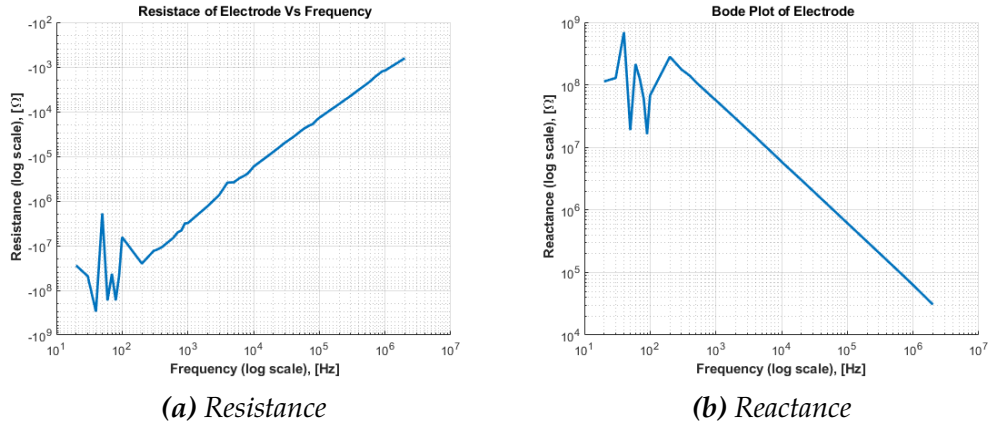


Figure 36: Bode plot of titanium electrodes coming from the impedance measurements performed with LCR-meter.

Concerning the reactance, its value at low frequency can be traced back by fitting the data and then computing it at $\nu = 0$ Hz, obtaining $|X_c| = 55.6 \pm 0.5 \text{ M}\Omega$ ²⁰. By means of the relation for a capacitor stated above the capacitance can be estimated:

$$C = \frac{1}{2\pi\nu|X_c|} \approx 71 \pm 3 \text{ fF} \quad (138)$$

where the error is estimated using the relative errors method.

The last parameter that has to be estimated is the resistance R . By observing the graph 36a and assuming once again linearity at low frequencies, the value obtained is $R = 38.4 \pm 3.9 \text{ M}\Omega$. The reader is invited to notice the negative sign of y -axis. The meaning of a negative resistance as to be re-conducted to the system theory. In fact, we are used to positive resistances when dealing with electrical circuits since the elements under test are mainly passive. In this case instead, the device is active, i.e. it is able to generate power instead of consuming it. In the following, to be as clear as possible, the current and voltage measurement will be reported in modulus in order to avoid the confusion provoked by this change of convention.

²⁰The error has been estimated by the standard deviation method after a filtering of the utility harmonics

Second test: coil of wire inductive analysis in air conditions

For what concerns the coils, the very same graph for impedance as been produced and reported in Fig. 37. Here, the linear increase after the zero is compatible with the relationship

$$X_L = j\omega L$$

where j is representing the imaginary unit, $\omega = 2\pi\nu$ the pulsation of the signal, ν the

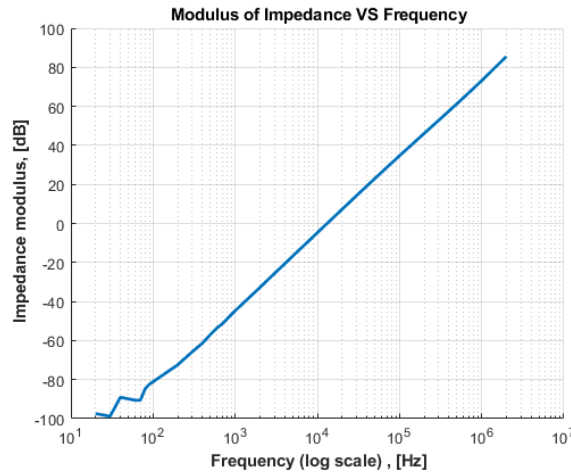
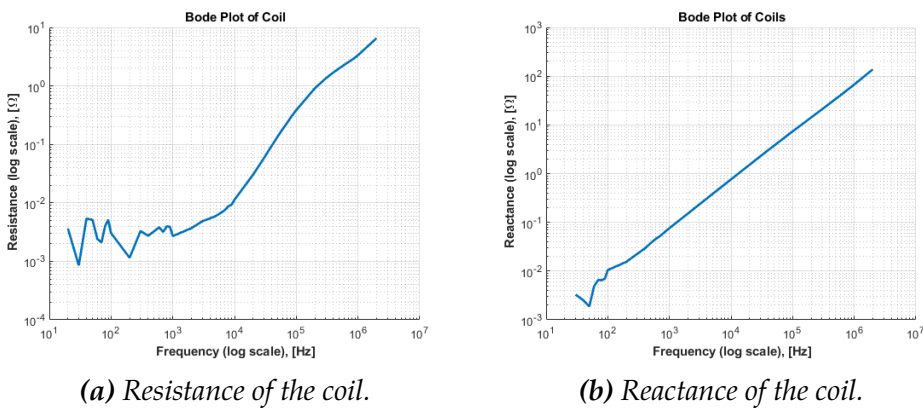


Figure 37: Coil of wire impedance modulus in air conditions as a function of frequency.

frequency and L the inductance, i.e. the property of an electric component for which the passage of an alternating current creates an electromotive force that counteracts the change in the current itself. For a better comprehension of the impedance, its component are reported separately in Fig. 38. Here, the presence of a resistance in series with the inductor is evident, even though the resistance is very low meaning that the wire used to create the coil is a good conductor. In fact its value has been computed and results to be $R = 35.5 \pm 0.5 \text{ m}\Omega$.



(a) Resistance of the coil.

(b) Reactance of the coil.

Figure 38: Bode plot of coil used for electromotive force harvesting.

Thanks to the expression of reactance stated above, it can be estimated from the data resulting in

$$L = \frac{X_L}{2\pi\nu} = 12.4 \pm 1.1\mu\text{H}$$

In order to prove this result, a further analysis can be performed. In the experimental apparatus under analysis, the number of coils is $N = 80$ and the solenoid has a length $l = Nd = 12\text{cm}$ with d indicating the wire diameter. Furthermore, two layers of coils are present having both $N/2$ rounds oriented in the same directions in order to reduce as much as possible the mutual induction. Neglecting such phenomena, considering the two layers as independent with a uniform magnetic field inside (no end effects) and expressing the magnetic field by means of Ampère law

$$\oint_{d\Sigma} \vec{B}d\vec{r} = \mu I \longrightarrow B = \frac{\mu_0 I}{l} \quad (139)$$

where Σ indicates the wire section, the overall magnetic flux through the solenoid can be expressed in a simplified form as:

$$\Phi = NAB = \mu_0\mu_r \frac{NIA}{l} \quad (140)$$

where the I represents the current and A the cross-section area of the solenoid. Having two layers, the different areas have to be accounted but since the cross-talk effects are not modeled, an average area can be used to describe the coils behaviour. Thus the situation is now a solenoid having length l with N turns and a section $A = 1.82\text{cm}^2$ which means an average radius $r = 0.76\text{cm}$. Thanks to the definition of inductance a closed form in the case of solenoids can be recovered using above expressions:

$$L_t = \frac{N\Phi}{I} = \mu_0\mu_r \frac{N^2 A}{l} \quad (141)$$

where $\mu_{0(r)}$ represents the absolute (relative) magnetic permittivity which, having only air in this case, can be taken as equal to the vacuum permittivity ($\mu_r^{Air} = 1.0006$). Substituting the values the theoretical inductance results to be $L_t = 12.16 \pm 0.81 \mu\text{H}$ which is consistent to the result obtained above.

The impedance is computed analysing the RL equivalent circuit, reported in Fig. 39, in series as

$$Z_c = R + j\omega L \quad (142)$$

where the subscript c identifies the coil.

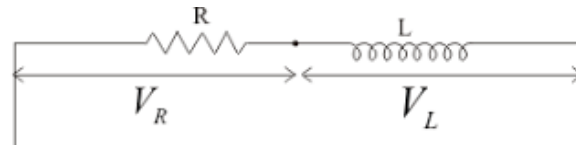


Figure 39: Equivalent circuit of the coil of wire.

The V_{rms} this time has been set to 0.1V and the power can be computed according to the expression:

$$P_c = \frac{V_{rms}^2}{\sqrt{R^2 + (\omega L)^2}} \quad (143)$$

In the next subsection the impedance measurements will be repeated fluxing different fluids (kerosene, ferrofluid and a mixture of ferrofluid and barium titanate) inside the pipe in order to compute once again resistance and reactance and obtain an evaluation of power extracted to verify the compatibility with current/voltage measurement and the equivalent circuit just proposed for the two components. It has to be evidenced that, because of induction phenomena and parasitic contribution on both resistance and capacitance, the equivalent circuit when the fluids are fluxed in the pipe could differ from the one in only air conditions.

5.2 Current and Voltage Measurements

Having analysed the equivalent circuit of the system, we can now focus on the current (I) and voltage (V) measurements in order to provide a quantitative estimation of the phenomena observed in the apparatus and to effectively verify the contribution given by the **pyroelectric** effect.

To perform these measurements, the source-meter (see fig. 30a), having the possibility to measure down to the hundreds of femto-Ampère (fA) for the current and micro-volt μV for the voltage, is connected to the two ends of the electrodes, to perform the capacitive measurements. It has to be pointed out to the reader that, during the post-processing, a soft data filtering has been performed because of the multimeter sensibility. In fact, even an air displacement caused by the operator movement could create a very big variation in the measure. To do so, the tool *isoutlier*, which gives the points in an adjustable range of data lying out of three standard deviation from the mean, and *mvavg*, that performs a moving average that smooth the data, of ©MATLAB have been exploited.

The ferrofluid used in this experiment is, once again, the **EFH3** whose main properties are reported in Tab. 1. The concentration of magnetite has been reduce from 12 to 2%vol to reduce the viscosity, which allows to partially limit some unwanted effects like magnetoviscosity, that influence deeply the fluid motion, the thermal conductivity, which is dependent on the amount of particles present in the colloid, and memory effects referred to the fluid nature since, for large magnetite concentration, the fluid cannot be considered Newtonian anymore.[56]

Since the aim is to effectively evaluate the pyroelectric coefficient, the other contribution to the current/voltage generation need to be removed. Thus, each component of the colloidal mixture of ferrofluid and barium titanate has been analysed separately. Moreover, several flow rate have been studied in order to analyse their effect on the pyroelectricity and to have a panoramic on the performances and investigate other possible effects occurring in the apparatus in different experimental conditions.

Kerosene

As a first step, pure kerosene has been pumped inside the tube in order to fill it paying attention to avoid air bubbles within the pipe which would modify the observation introducing parasitic resistances and capacitances. Successively, the pump has been turned OFF and the system has been left at rest about ten minutes in order to avoid

any influence due to the initial motion inertia. Then, the baseline of the quantity of interest versus time have been acquired three times and averaged resulting in the curve reported in Fig. 40. This operation is necessary to remove this initial value, assumed to be an offset of the instrumentation, from future data setting the starting point to zero.

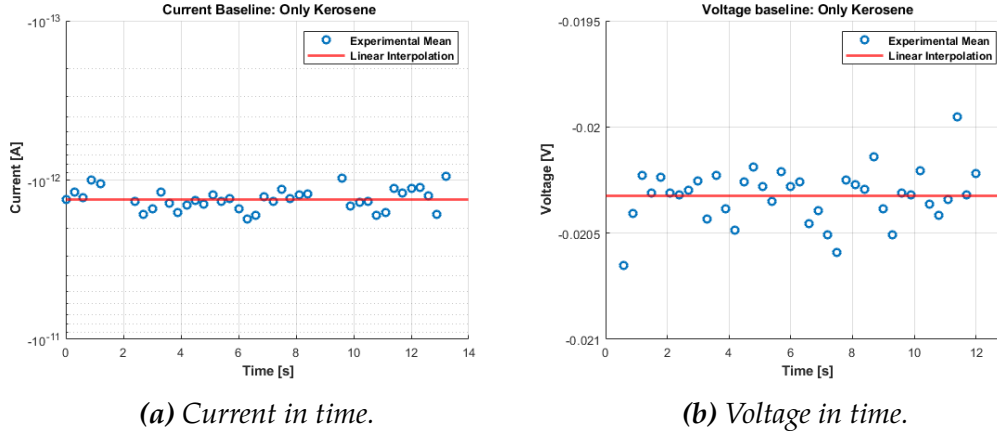


Figure 40: Baseline of the figure of merit acquired with only kerosene filling the system.

To obtain the base values the mean of each data-set has been performed and successively this values have been averaged:

$$V_{Offset,K} = -20.328 \text{ mV}$$

$$I_{Offset,K} = -1.330 \text{ pA}$$

where the subscript K is used to indicate the presence of only kerosene inside the system.

Now that the initial values have been acquired, the pump is turned ON. In order to evaluate the contribution of the kerosene to all the velocities of interest, namely 1, 2, 3, 5 and $10 \frac{cm}{s}$, each flow rate has been successively set on the pump. In other words, the pump has been turned ON to a specific flow rate and, once the transitory is passed and the steady-state(ss) has been reached, turned OFF and a new value is set. This allow to observe the charge and discharge of the electrodes and avoid to modify the measurement condition since there is no necessity to enter in contact with the system. In Fig. 41 the results have been reported.

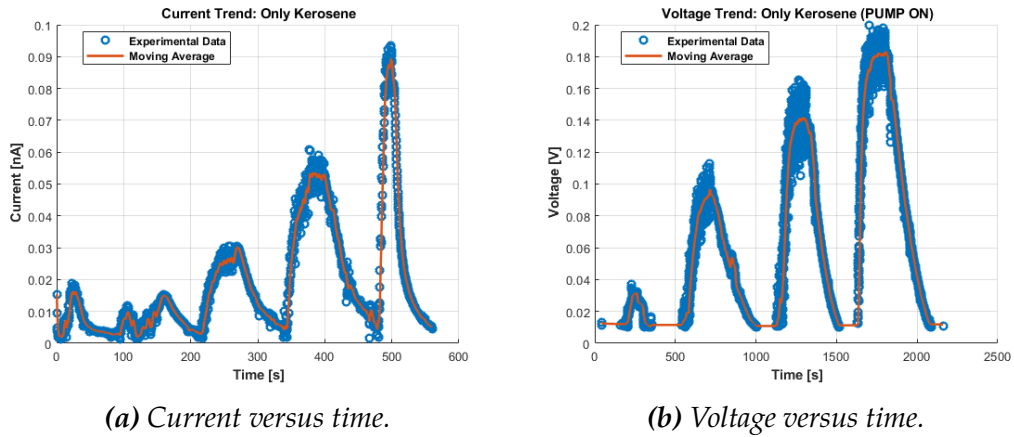


Figure 41: Trend of the figure of merits of the system filled with only kerosene at different flowing rates. The baseline acquired in no motion condition has been subtracted to the data.

As it can be noticed in Fig. 42a the contribution given by the kerosene to the current lies in the range of tens of pico-Ampères. In particular, for first and second velocities it is not possible to distinguish a value since the noise is comparable to the current produced. However, increasing the velocity a relatively small increase in both the current and voltage is found. This indicates that kerosene is able to develop a very little triboelectric effect either with the teflon (material of the tube) or the titanium (material of the electrodes). The voltage reported in Fig. 42b shows a peak also for the second flow rate velocity meaning that a contribution is always present even if negligible.

Ferrofluid

The second step to correctly estimate the contribution to the overall current and voltage of barium titanate is to provide an estimation of the magnetite influence. In fact, the FF used in this frame is a dispersion of magnetite NPs in a liquid hydrocarbon, similar to kerosene, thus the contribution brought by them has to be investigated. To do so, the very same process of previous paragraph is repeated. The baseline of both figure of merits is acquired three times and then averaged in order to obtain the offset value with the system at rest:

$$V_{Offset,FF} = 3.7259 \text{ mV}$$

$$I_{Offset,FF} = 1.6237 \text{ pA}$$

The data have been reported in Fig. 42 where the red line indicates the mean.

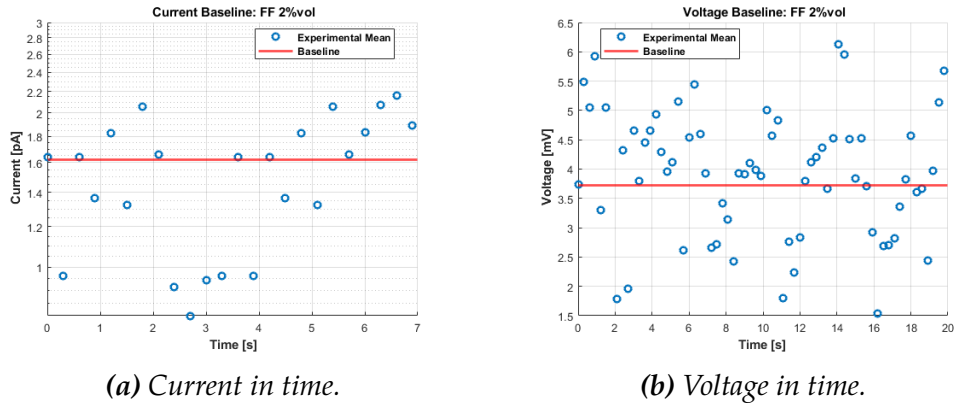


Figure 42: Baseline of the figure of merit acquired with ferrofluid at 2% of magnetite concentration filling the system.

After having removed this shift from the data acquired at the different velocities, i.e. having set to zero the initial point of the $V(t)$ and $I(t)$ graphs, they have been smoothed again removing the outliers and then performing the moving average (MA). In order to avoid loss of information the number of points used for the MA have been kept quite low with respect to the acquisition time (set to 0.3s), like ≈ 30 points. The graphs are reported in Fig. 43 and the moving average will be exploited for the estimation of the current and voltage average value at each velocity.

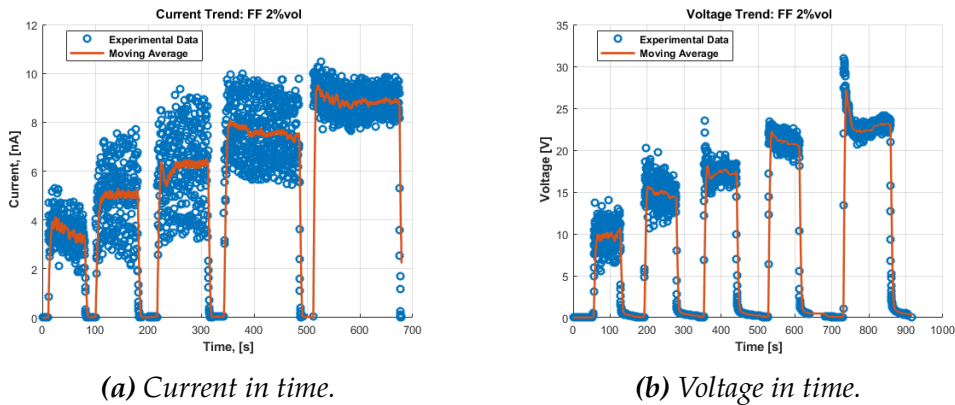


Figure 43: Trend of the figure of merits of the system filled with ferrofluid, having 2% of volume concentration of magnetite, at different flow rates.

As it can be noticed, the values of both figures of merit during the motion is strongly increased. This means that the contribution brought by the FF in the final measurements will be not negligible and it has to be subtracted to obtain the net BaTiO_3 contribution. The reason why there is a current/voltage production is probably linked to the electrostatic separation effect and, in particular, triboelectric charging provoked by magnetite nanoparticles crawling on the pipe's wall.[80] This conclusion

is reached also observing the dependence on the velocity of the effect but it cannot be excluded a priori the contribution of other effects. Further experiments need to be done in order to determine the nature of such phenomenon but this is out of the scope of this thesis.

Ferrofluid and Barium Titanate

Finally, the barium titanate has been added to the ferrofluid in concentration 0.5% vol corresponding to ≈ 2.925 g of BaTiO_3 in 100 ml of mixture.[81] This would allow to evaluate the influence of the concentration on the pyroelectric current. This latter is expected to increase since the introduction of more particles inevitably implies, if homogeneous concentration is assumed²¹, a larger number of particles hitting the electrode and transferring their charge. Moreover, in order to study the temperature influence on the current/voltage produced, the temperature has been measured using three thermocouples type N as mentioned in the description of the experimental apparatus presented in subsection 4.5. These are used to measure the fluid temperature in the becher and in proximity of first and second electrodes. This measurement have been performed in two different ways:

1. Initially the solution has just been kept in agitation using a magnetic stirrer which, besides having the task to maintain the NPs suspended in the fluid, provokes a slight temperature increase, with respect to the laboratory ambient temperature ($RT = 22^\circ\text{C}$), around 2.5°C as can be observed in Tab. 6;
2. Secondly, the solution has been heated up to 60°C before being fluxed in the pipe. The equilibrium temperature reached during the measurements is lower due to the cooling suffered by the fluid during its motion so the reference temperature of the becher reported in Tab. 7 refers to the stable value after the equilibrium is reached.

These two different experimental conditions allow to associate the increase in current to the effective pyroelectric current produced and this latter to the temperature variation in time observed.

²¹This is not a restrictive assumption since a magnetic stirrer has been used to maintain the whole fluid in continuous motion in order to avoid agglomeration and flocculation of BaTiO_3 NPs. Thus the solution can be assumed homogeneous without any loss of consistency.

Temperature	$v_p = 1\text{cm/s}$	$v_p = 2\text{cm/s}$	$v_p = 3\text{cm/s}$	$v_p = 5\text{cm/s}$	$v_p = 10\text{cm/s}$
Becher (T_B)	25.0 ± 0.1	24.8 ± 0.1	24.7 ± 0.1	24.8 ± 0.1	25.0 ± 0.1
Electrode 1 (T_{E_1})	23.9 ± 0.1	23.8 ± 0.1	23.8 ± 0.1	23.7 ± 0.1	23.8 ± 0.1
Electrode 2 (T_{E_2})	23.8 ± 0.1	23.5 ± 0.1	23.6 ± 0.1	23.5 ± 0.1	23.5 ± 0.1
$\Delta T_{B,E_1} = T_B - T_{E_1}$	1.1 ± 0.2	1.0 ± 0.2	0.9 ± 0.2	1.1 ± 0.2	1.2 ± 0.2

Table 6: Temperatures of Becher (T_B), first (T_{E_1}) and second (T_{E_2}) electrodes with only stirrer as heating source. In the last row the temperature difference experienced by the particle flowing from the becher to the first electrode ($\Delta T_{B,E_1}$) has been reported. The flow rate set on the pump refers to the fluid velocity in a tube having internal diameter $d_{in}^1 = 2\text{mm}$.

In Tab. 6 it can be observed that the temperature in the becher increases with the velocity; however, this is just a side effect provoked by the continuous heating provided by the stirrer. The temperature difference among the two electrodes remains quite stable with a $\Delta T_{E_1,E_2} \approx 0.20 \pm 0.05^\circ\text{C}$ while the one among the becher and first electrode is $\Delta T_{B,E_1} = 1.1 \pm 0.2^\circ\text{C}$.

In Tab. 7 instead, the temperature difference among the becher and the first electrode has been observed to decrease with the velocity increasing whereas the temperature difference among electrodes remains constant. This can be associated to the fact that the fluid flows in the tube with internal diameter $d_1 = 2\text{mm}$ approximately until the first electrode²² thus the flow velocity is very high according to the pump flow rate, but then it enters in the tube with $d_4 = 10\text{mm}$ and the velocity, for mass flow conservation, decreases abruptly and it doesn't influences that much the heat loss. These data will be used in the following for the evaluation of primary pyroelectric coefficient.

Temperature	$v_p = 1\text{cm/s}$	$v_p = 2\text{cm/s}$	$v_p = 3\text{cm/s}$	$v_p = 5\text{cm/s}$	$v_p = 10\text{cm/s}$
Becher (T_{Bec})	47.0 ± 0.1	50.6 ± 0.1	49.0 ± 0.3	50.1 ± 0.2	47.8 ± 0.1
Electrode 1 (T_{E_1})	27.2 ± 0.1	29.9 ± 0.1	34.3 ± 0.1	35.2 ± 0.1	36.7 ± 0.3
Electrode 2 (T_{E_2})	24.6 ± 0.1	26.7 ± 0.1	31.4 ± 0.1	32.1 ± 0.1	33.8 ± 0.2
$\Delta T_{B,E_1} = T_B - T_{E_1}$	19.8 ± 0.2	30.7 ± 0.2	14.7 ± 0.2	14.9 ± 0.2	11.1 ± 0.2

Table 7: Temperatures of Becher (T_B), first (T_{E_1}) and second (T_{E_2}) electrodes with stirrer and heating plate as heating sources. In the last row the temperature difference experienced by the particle flowing from the becher to the first electrode ($\Delta T_{B,E_1}$) has been reported. The flow rate set on the pump refers to the fluid velocity in a tube having internal diameter $d_{in}^1 = 2\text{mm}$.

²²It has to be noticed that the first electrode is placed at the very beginning of tube with internal diameter $d_4 = 10\text{mm}$, approximately 2 cm after the junction with the precedent pipe. Further details on the structure are in the following of this treatise.

The temperature measurements have been performed during the acquisition of current and voltage from the capacitive electrodes following the same procedure of previous paragraphs. The baseline is the very same observed in only ferrofluid case so the graphs are not reported for the sake of simplicity. The measurements are reported in Fig. 44 and the smoothing is performed eliminating the outliers and then using the moving average.

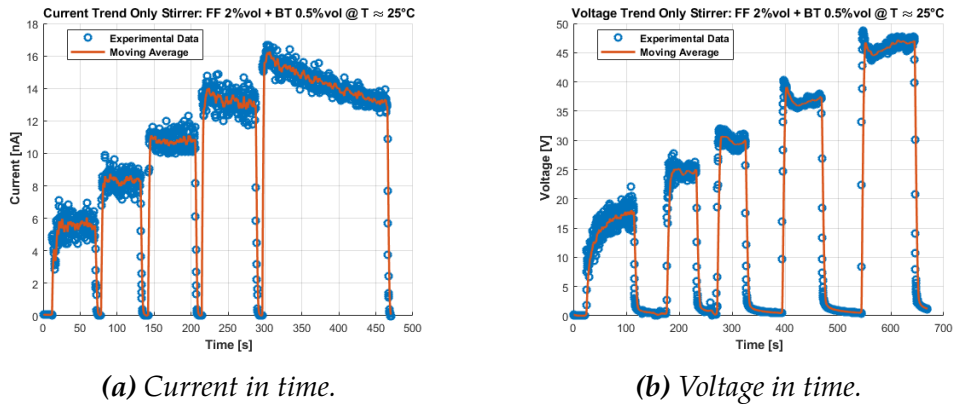


Figure 44: Trend of the figures of merit of the system filled with ferrofluid, having 2%vol of volume concentration of magnetite and 0.5%vol of barium titanate, at different flowing rates. The data have been acquired using the magnetic stirrer as only source of heat, i.e. around a temperature $T \approx 25^\circ\text{C}$

An overall increase of the current and voltage production is observed which means that the barium titanate act as a voltage generator as observed in the equivalent circuit of previous section. To prove their dependence on temperature the becher containing the solution has been heated up and the measurement have been repeated without varying concentration. The results have been plotted in Fig. 45 where again a clear increase in both the figure of merits occurs.

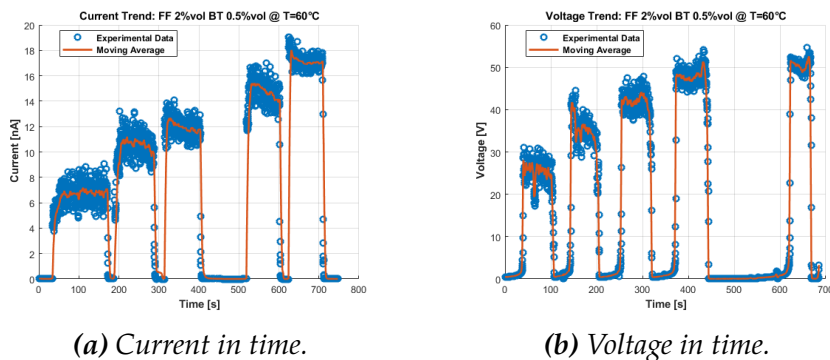


Figure 45: Trend of the figure of merits of the system filled with ferrofluid, having 2%vol of volume concentration of magnetite and 0.5%vol of barium titanate, heated up to 60°C at different flowing rates.

To summarize all the results obtained so far, the current I and voltage difference ΔV , obtained by fitting the values measured during steady-state conditions for all the velocities of previous graphs, are reported schematically in Tab. 8 where the errors have been obtained by means of the standard deviation method using the *std* tool of ®MATLAB software.

Fluid	FoM	Pump Rate				
		1cm/s	2cm/s	3cm/s	5cm/s	10cm/s
Kerosene	ΔV [V]	-	0.031 ± 0.001	0.092 ± 0.001	0.141 ± 0.001	0.181 ± 0.001
	I [nA]	-	-	-0.023 ± 0.001	-0.050 ± 0.001	-0.085 ± 0.001
Ferrofluid (FF)	ΔV [V]	9.7 ± 0.3	14.9 ± 0.4	17.2 ± 0.3	20.7 ± 0.1	23.0 ± 0.1
	I [nA]	-3.3 ± 0.1	-5.0 ± 0.1	-6.2 ± 0.1	-7.5 ± 0.1	-8.8 ± 0.1
BaTiO ₃ and FF Only Stirrer	ΔV [V]	17.5 ± 0.2	24.5 ± 0.3	29.5 ± 0.2	36.8 ± 0.2	46.7 ± 0.2
	I [nA]	-5.6 ± 0.2	-8.3 ± 0.2	-10.7 ± 0.1	-12.1 ± 0.2	-13.3 ± 0.2
BaTiO ₃ and FF at $T = 60^\circ\text{C}$	ΔV [V]	25.5 ± 0.7	34.9 ± 0.4	41.9 ± 0.6	47.7 ± 0.5	50.2 ± 0.4
	I [nA]	-6.8 ± 0.2	-10.7 ± 0.2	-11.7 ± 0.1	-14.8 ± 0.3	-17.0 ± 0.1

Table 8: Mean values of current and voltage obtained by fit operator in MATLAB software. The errors have been computed using the standard deviation method.

In order to show the performances of this system, the output power produced during the motion of Kerosene (K), Ferrofluid at 2% vol concentration ($FF2\%$) and a colloidal mixture of FF and barium titanate (BT) in 0.5% vol concentration (FFBT) in both low and high heating conditions, $T = 25^\circ\text{C}$ and $T = 60^\circ\text{C}$ respectively, have been reported in Fig. 46.

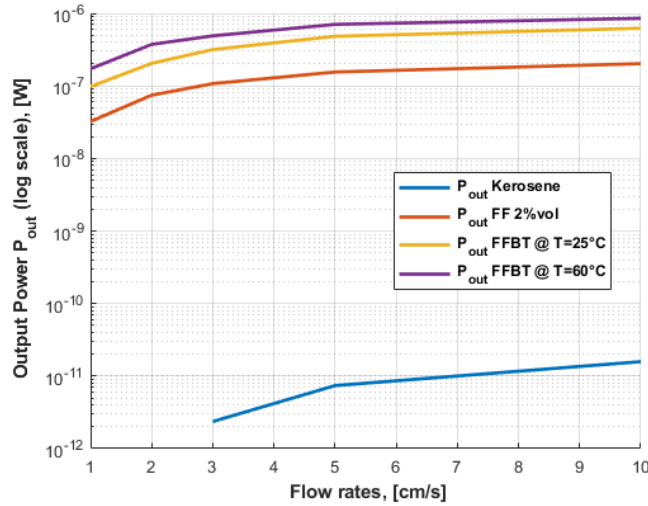


Figure 46: Power output ($P_{out,i}$) computed for the i -th fluids fluxed namely: Kerosene (K), Ferrofluid at 2% vol concentration ($FF2\%$) and a colloidal mixture of FF and barium titanate (BT) in 0.5% vol concentration (FFBT) in both low and high heating conditions, $T = 25^\circ\text{C}$ and $T = 60^\circ\text{C}$ respectively

The saturation trend that can be observed is typically representative of a triboelectric contribution to the current/voltage generation. However, the viscous effects cannot be neglected in principle: a link among the power saturation and the flow rate increase could be found in the effect observed during the experiment with titania where the shallower layer of fluid is observed to decrease its velocity. This phenomenon will be investigated more accurately also thanks the ultrasonic velocity profile method (UVP) implemented in the cell (see subsection 4.1.3) which will allow to follow the fluid motion in detail.

5.2.1 Pyroelectric Coefficient Evaluation

From the data reported in Tab. 8, it can be appreciated the contribution given by barium titanate. However, to associate the increase in the figure of merits to the pyroelectric current, the pyroelectric coefficient must be evaluated using the **electric contact** method.[53] This is a static approach, i.e. a method where the temperature gradient is maintained constant, in which it is possible to extract a compact formula for the primary pyroelectric coefficient p_I . It doesn't allow the evaluation of the other components of p since there is neither uniform or spatially varying viscous stress applied, which is needed to evaluate the secondary and tertiary components as can be seen in Eq. 46, nor electric field applied, which would enable the measurement of the field induce component of p (fourth term of Eq. 46).

In order to estimate the charge developed by each NP, experiencing an infinitesimal temperature variation dT , it can be used the expression:

$$dQ_k = p_I A_k dT \quad (144)$$

where A_s identifies the NP surface and the subscript k the k -th NP. To perform this estimation, the temperature variation in time can be assumed to be linear and thus can be evaluated accounting the time t_{NP} needed by the particle to reach the first electrode, where it is assumed to have the largest charge release. The experimental apparatus under analysis is composed by different pipes:

1. The first is connected to the pump having inner diameter $d_1 = 2$ mm and length $l_1 = 50 \pm 0.1$ cm;
2. The second has $d_2 = 4$ mm and a length of $l_2 = 40 \pm 0.1$ cm;
3. The third $d_3 = 7$ mm and $l_3 = 8 \pm 0.1$ cm;
4. The fourth, where are place the electrodes, has an internal diameter $d_4 = 10$ mm

and the length traveled by the particles until the electrode 1 is $l_4 = 2 \pm 0.1$ cm.

For a better understanding of the structure a schematic reproduction of the apparatus with quotes is reported in Fig. 47.

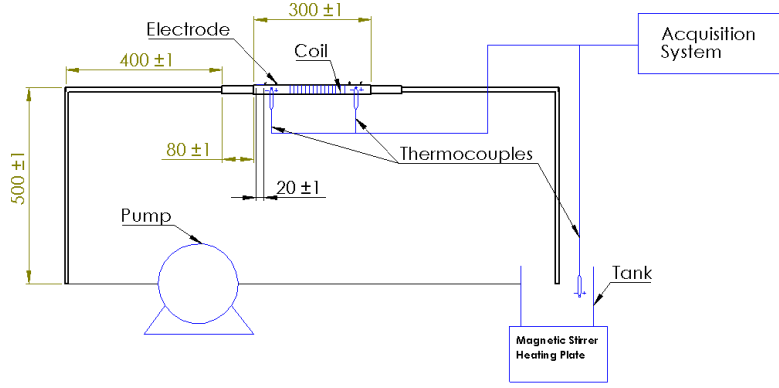


Figure 47: Scheme of the experimental apparatus under analysis with quotes obtained by ©SolidWorks

Knowing these dimensions, the continuity equation for the volumetric flow can be applied, thus the time of travel becomes:

$$t_{NP} = \sum_{i=1}^4 \frac{l_i}{v_i} \quad (145)$$

where the subscript i is an integer number identifying each tube section and v_i is the corresponding velocity calculated according to the flux continuity:

$$v_i = \frac{d_1^2}{d_i^2} v_1 \quad (146)$$

where v_1 indicates the velocity in the first time that is equal to the flow rate set by the pump.

Being interested in the volume of fluid in contact with the electrode, the attention is focused on a column of fluid V with height equal to the electrode's length $l_e = 3 \pm 0.1$ cm and radius equal to $r = d_4/2$ ²³. The overall infinitesimal charge contained

²³Notice that the electrode is placed in the fourth tube

in this volume will be given by:

$$dQ = \sum_{i=1}^N dQ_s \quad (147)$$

with N indicating the number of particles in V which can be simply estimated from the ratio among the BT volume contained in the column, which is the 0.5% of V , and the volume of each BT NPs having a spherical shape with diameter $D = 500$ nm. Accounting for all the travel from the becher to the first electrode, the overall temperature change experienced by the barium titanate NPs will be equal to the one measured (see Tab. 6 and 7). The charge accumulated in V , using Eq. 144, will be:

$$Q = \int_0^{\Delta T} N p_I A_s dT \quad (148)$$

where it has been assumed that each particle develops the same amount of charge dQ_s . Now that we have obtained the amount of charge Q contained in the volume of fluid V , the spatial distribution of NPs has to be taken into account. In other words, since the electrode is placed on a small region of pipe's surface only a portion of the BT particles will be able to reach it and, consequently, transfer their charges. In particular, if homogeneous distribution is considered, only the particles contained in a small parallelepiped of volume V_c , having area equal to the electrode's one ($A_E = 3 \times 0.5 \text{ cm}^2$) and a thickness equal to D , will be able to touch the electrode. Thus, the nanoparticles in contact with the electrode will be

$$N_c = \frac{V_c}{V_{BT}}$$

where V_{BT} is the volume of one BT nanoparticle. According to the work of Jachalke *et al.*[53], the pyroelectric coefficient can be expressed as:

$$p_I = \frac{I_p C_M}{A_e F_h} \quad (149)$$

where I_p represents the pyroelectric current, C_M the heat capacity of barium titanate, A_e the effective electrodes area and F_h the heat flux. This latter can be defined using the Fourier's law in one dimension, assuming x to be the direction parallel to the electrode's area, as:

$$F_h = -\kappa \frac{dT(x)}{dx} \quad (150)$$

where the temperature spatial distribution is known, since the decreasing form becher to the electrode has been assumed to be linear, and κ is the BT thermal conductivity.

Concerning the effective contact area A_e , which indicates the portion of electrode surface in contact with the nanoparticles, the deformation of the particle needs to be accounted. One of the first models proposed to estimate the contact area among a flat surface and a nanoparticle incident onto it has been proposed by Abbott and Firestone[82, 83] where plastic deformation was assumed. They assumed to consider the sphere, representing the NP, as truncated, because of the impact, of a quantity ω (see Fig. 48) which, in this case, can be estimated, according to the accuracy of the instrument, around 1 nm.²⁴

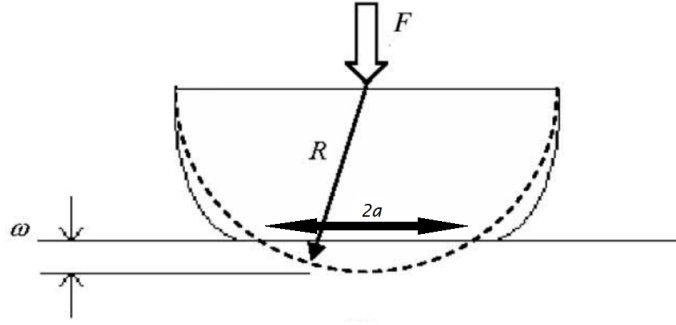


Figure 48: Particle deformation during the contact with the electrode.[85]

Thus the force F acting on it could be estimated according to:

$$F = 2\pi R\omega H \quad (151)$$

with $R = D/2$ indicating the sphere radius and H representing the material hardness. However, this formula has been proven to overestimate the force because of the assumption of plastic deformation.[86] In the work of Greenwood and Williamson (GW) [87] it has been proved that, for a correct estimation of the contact radius of a rigid nanoparticle, as in the case of perovskite structure, for a deformation lower than 40% of the particle radius the Jackson and Green[85] formula for elastic-plastic contact can be used:

$$\frac{a}{R} = \sqrt{\frac{\omega}{R}} \left(\frac{\omega}{1.9\omega_c} \right)^{\frac{B}{2}} \quad (152)$$

where a is the radius of the deformed region, B is a material parameter that accounts the relation among the yield strength S_y , i.e. the strain the material can support still maintaining an elastic behaviour, and the young modulus E according to the

²⁴From the datasheet [84] it is known that the sizes have been estimated by means of scanning electron microscopy (SEM). Being the accuracy of such technique estimated around few nm, depending on the beam size used, this assumption provokes no lack of consistency with the experimental situation.

expression

$$B = 0.14 \exp \left[23 \left(\frac{S_y}{E} \right) \right] \quad (153)$$

and ω_c is the critical indentation which can be expressed according to [86]

$$\omega_c = \left(\frac{\pi c S_y}{2E} \right)^2 R \quad (154)$$

with $c = 1.295 \exp(0.736\nu)$ being ν the Poisson ratio. In [88] different barium titanate powder of different size have been investigated in order to determine their mechanical properties. One of the samples investigated has particles diameter of $\approx 0.55\mu\text{m}$ which is comparable with the one used in these experiments. Thus, the values for these parameter can be found to be $S_y = 486.2\text{MPa}$ and $E = 116\text{GPa}$ respectively. However, it has been proven in [89] that the Young modulus is a function of temperature passing from 116GPa at a working temperature $T = 340\text{K}$ (corresponding to the second experimental condition) to 85GPa at $T = 300\text{K}$ meaning that a larger deformation will take place at higher temperatures. Finally, the Poisson ratio, defined as the ratio among the axial stress applied and the transverse section reduction, of the BaTiO_3 was proven to lie around $\nu = 0.35$.

Substituting these values in the above formulas and solving Eq. 152 for the contact surface radius a of the single nanoparticle we get:

$$a_c = 1.31 \text{ nm}$$

$$a_h = 1.38 \text{ nm}$$

where the subscript c and h have been introduced to distinguish the two experimental conditions, only stirrer and with heating plate respectively. Thus, the overall contact area, i.e. the effective electrode area can be estimated to be:

$$A_{e,c} = N\pi a_c^2 = 0.0031 \text{ cm}^2$$

$$A_{e,h} = N\pi a_h^2 = 0.0034 \text{ cm}^2$$

Finally, the pyroelectric current is assumed to be the difference between the measured one measured in presence of barium titanate, in both heating conditions, and the one obtained fluxing only ferrofluid in the pipe (see Tab. 8). This operation is needed to avoid other effects as contribution to the current production, like tribocharging provoked by magnetite nanoparticles crawling on teflon. Thanks to the previous assumption and by the fact that the current is nothing but the amount of charge

flowing per unit time, I_p can be expressed as:

$$I_p = \frac{Q}{t_{NP}} \quad (155)$$

and the primary pyroelectric coefficient can be estimated by means of Eq. 149. The results are reported in Tab. 9.

	$v_p = 1\text{cm/s}$	$v_p = 2\text{cm/s}$	$v_p = 3\text{cm/s}$	$v_p = 5\text{cm/s}$	$v_p = 10\text{cm/s}$
$p_I^c [\mu\text{C m}^{-2} \text{K}^{-1}]$	2.52	2.49	2.85	2.76	2.28
$p_I^h [\mu\text{C m}^{-2} \text{K}^{-1}]$	3.98	3.14	2.68	2.10	1.55

Table 9: Primary Pyroelectric coefficients calculated when the magnetic stirrer is the only heating source (label c) and also when the sample is heated at 60°C (label h)

From this it can be noticed that the p_I^c remains almost constant which is coherent with the temperature measurement of Tab. 6 where the temperature difference among becher and electrode is observed to remain approximately constant at all the velocities. In Fig. 49 is reported a representation of the pyroelectric coefficient of barium titanate as a function of temperature.[90] The experimental value obtained in this condition is comparable to the one reported in literature for the a temperature lying around $T = 300\text{K}$. Thus, barium titanate effectively enhance the performances of current production thanks to the pyroelectric charge released on the electrode. Moreover, the increase in p_I^h at low pump rates is coherent with the increase observed in Fig. 49 passing from ≈ 2.2 to $3.7 \mu\text{C m}^{-2}\text{K}^{-1}$.

For what concerns the strong decrease in p_I^h observed at high pump rate, it can be associate to different contributions like the decrease with velocity in temperature difference measured when the fluid is heated up to $T = 60^\circ\text{C}$ (see Tab. 7) or an effect observed in an experiment where the shallower layer of fluid, i.e. the layer in contact with the tube, decreased its velocity at $v_p = 5 \text{ cm/s}$ and $v_p = 10 \text{ cm/s}$ provoking a decreasing in the number of particles able to reach the electrode and discharge. This phenomenon can also be observed for p_I^c where the very same effect, even though less evident, occurs. A further reason could be found in the ferrofluid contribution. In fact, data with only ferrofluid fluxed in the apparatus at $T = 60^\circ\text{C}$ have not being acquired and thus a contribution brought by the heating of magnetite nanoparticles and surfactants cannot be excluded a priory. Besides, in later experiments, whose data are not comparable in magnitude with these²⁵, a net contribution coming from

²⁵The data cannot be compared with these reported here since they have been acquired

hot ferrofluid was proven meaning that further acquisition needs to be done before clarify the role of pyroelectricity in this frame.

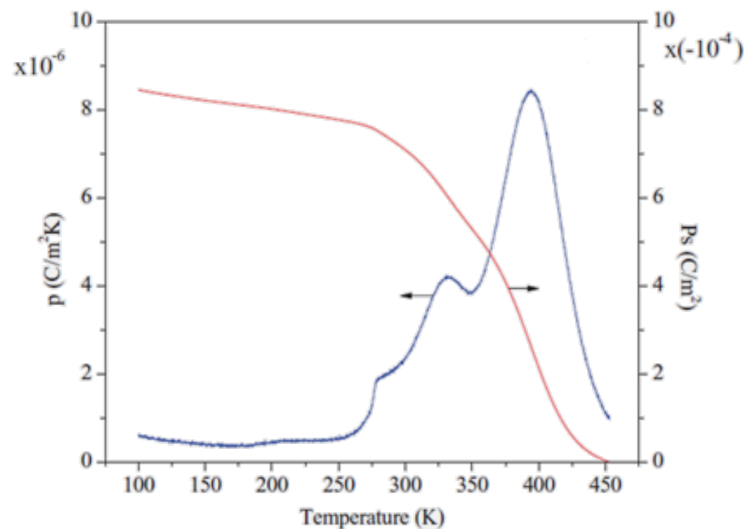


Figure 49: Barium Titanate pyroelectric coefficient as a function of temperature.[90]

The next steps would probably be:

- Synthesize barium titanate NPs with the procedure presented in [91] or buy a finer powder in order to suspend it in a carrier liquid;
- Investigate the possibility to change carrier fluid from kerosene to water in order to move toward a greener approach;
- Analyse different procedure to suspend the PE NPs without the use of surfactants, which would reduce the charge transfer by electrostatic contact, or investigate the electroactive surfactants as possible solution to this issue.[92];
- Reduce the noise in the measurements decoupling mechanically the pump from the system of measurement;
- Characterize the pyroelectric powder by means of others methods in order to have a comparison with the estimation provided by means of the method reported here;
- Investigate the possibility to dope barium titanate to enhance its pyroelectric coefficient;
- Characterize the current and voltage generation as a function of the nanoparticle concentration;
- Perform temperature cycles with different rate of variation in order to measure also the secondary pyroelectric coefficient;

after having reconstructed the whole system.

- Introduce different kind of powders to exploit more effects simultaneously, like the titania investigated for triboelectric effect;
- Test different magnet configurations to find the best coupling with the temperature gradient established;
- Test different temperature range to find the best region of operation;
- Reduce the error introduced by the long path the particle needs to travel before releasing the charge on the electrode: the idea is to place an electrode directly on the heat source in order to make effective the temperature gradient experienced by the nanoparticle;
- Place the second electrode to ground potential: in this experiment both the electrodes were immersed in the fluid so a differential acquisition has been performed while it could be interesting to measure the overall charge released on one single electrode. Moreover this allows another method of p_I estimation called *charge compensation method*.
- Reduce the losses during the measurements: in these experiments the loss of kerosene mass were not negligible. Kerosene is a volatile substance and consequently a continuous evaporation during the whole analysis were present, caused by the not perfect sealing of the apparatus, varying the experimental conditions in a sensible way.
- Find a way to make the measurements more repeatable: the NPs sedimentation in the tube made impossible to compare the measurements performed with different setups;
- Investigate the contribution of hot ferrofluid: in the last part of this treatise the influence of hot and cold ferrofluid on the impedance measurements of both coil and electrodes will be shown. However, it would be better to perform a current voltage acquisition as the one presented here for the ferrofluid only slightly heated since it cannot be excluded a priori a further contribution introduced only by the thermal expansion of the magnetite NPs or by the magnetization reduction due to temperature increase.

Some of these problems will be solved by the cell presented in Fig. ?? which will allow reproducible measurements, no evaporation of the carrier fluid so more affordable analysis and, consequently, the possibility to investigate different magnetic field and temperature gradient combinations. It has to be mentioned that such cell has been designed for different purposes besides those named before, e.g. the possibility to perform visual observations of the ferrofluid thermo-magnetic motion. However, the working principle differ deeply with the one presented here. In fact, the idea was to create a self-sustained device able to work as single unit with no need of

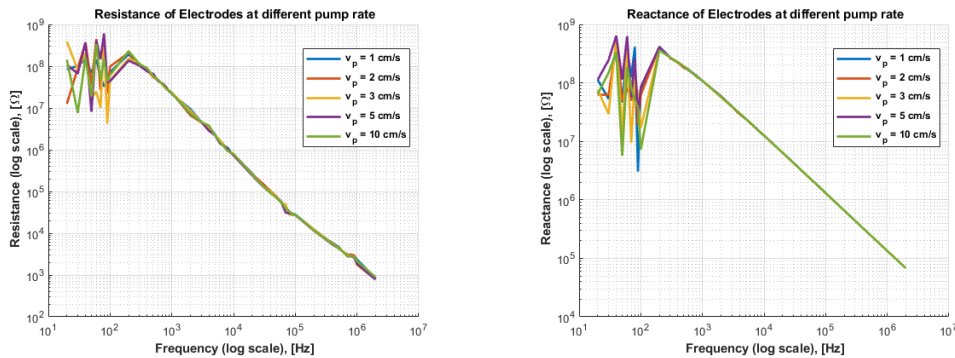
supply. The pump will be used just to fill the chamber but then the only source of energy it will be coupled is a thermal sink. This, because of the effects reported in section 2, will interact with the external magnetic field generated by the permanent magnets moving the fluid. The barium titanate nanoparticles will follow the ferrofluid streamlines because of their low Stokes number displacing them from the hot to the cold side allowing the harvesting of pyroelectric charge by means of some electrodes placed in the cell walls. Moreover, a wall dividing the chamber in two identical parts, in contact just by means of the holes reported on it, has been added in order to investigate the possibility to exploit a surface tension gradient which will introduce a further contribution to the motion: this coupled with an intelligent heat distribution on the cell wall could provide a preferential direction of convection.

5.3 Generated Power

The last part of the experiment regards the acquisition of the electrodes and coil impedance during the fluid motion. The results in this section have been obtained by filling the pipe with ferrofluid only at 2% vol of magnetite concentration, thus the capacitive measurement on the titanium electrodes will return a power not comparable with the one obtained by voltage and current measurements in previous section since barium titanate is not present. However, they enable to provide a quantitative estimation of the overall performances of the device and to make an estimate of the barium contribution. Moreover, in order to study the influence of heat on the ferrofluid, the analysis is performed in two conditions: room temperature (no source of heat is applied) and working temperature $T = 60^\circ\text{C}$ meaning that before turning the pump ON the ferrofluid is left warm up using a heating plate.

Electrodes

Starting from the capacitive acquisition, the resistance and reactance, at the same velocities treated so far, are acquired three times for each curve and then average to reduce random fluctuation. In Fig. 50 are reported these quantities in room temperature condition.

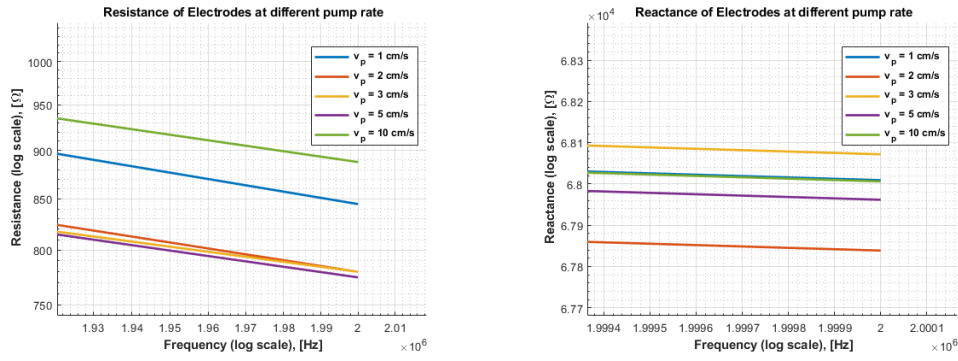


(a) Resistance of the titanium electrodes.

(b) Reactance of the titanium electrodes.

Figure 50: Bode plot of titanium electrodes, used for electrostatic charge recovery, figure of merits. The legend report the pump rate velocity for each curve.

The first thing that has to be noticed is an increase in the noise at low frequencies with respect to the previous measurement. This was expected since in the case, the presence of a moving fluid and also the rotation of the pump contribute to it. Moreover, from these graphs is not possible to appreciate the differences among the different curves which appear overlapped because of the very small variation in R and X . For this reason, they have been reported zoomed in Fig. 51.



(a) Resistance of the titanium electrodes. (b) Reactance of the titanium electrodes.

Figure 51: Detail of Fig. 50. The image is zoomed in order to appreciate the differences among the curves obtained for different pump rates.

To make the things even clearer, fit of the curves have been performed by means of $\text{\textcircled{R}}\text{MATLAB}$ software allowing a precise estimation of both these parameters, which have been reported in Tab. 10. It has been decided to report directly the capacitance instead of the reactance because will be more useful in the following.

	$v_p = 1\text{cm/s}$	$v_p = 2\text{cm/s}$	$v_p = 3\text{cm/s}$	$v_p = 5\text{cm/s}$	$v_p = 10\text{cm/s}$
Resistance [$M\Omega$]	93 ± 5	154 ± 4	175 ± 13	195 ± 15	131 ± 13
Capacitance [pF]	1.30 ± 0.05	1.31 ± 0.05	1.30 ± 0.04	1.29 ± 0.05	1.30 ± 0.05
Power Produced [nW]	10.7 ± 0.5	6.5 ± 0.4	5.7 ± 0.05	5.1 ± 0.3	7.6 ± 0.6

Table 10: Resistance and Capacitance at different flow rate velocities of the capacitive titanium electrodes.

These data have been computed using the very same approach exploited in subsection 5.1. It can be noticed that an increase is present in the resistance until $v_p = 5\text{cm/s}$ whereas at the last one, an abrupt decrease is registered. This indicates a dependence on the velocity and that, above a certain threshold, an increase in the drag force is probably present. In other words, until a certain pump rate the flow is mainly laminar and the slip on the pipe wall is gentle, meaning that the drag force imposed on the particles is negligible. Above this threshold instead, this force increases making the flow turbulent and, as been observed in other experiments, creates a slowly moving layer of particles attached to the wall. This implies that, since the electrodes are placed in direct contact with the teflon, less particles will be able to reach it in order to transfer their charge, which explains in part the abrupt decrease observed in pyroelectric coefficient at higher pump rates. Furthermore, the layer of slow particles creates a shield which avoid partially the triboelectric contribution. The situation changes for the capacitance where no dependence on velocity is shown. It could be

interesting to notice that, assuming the two electrodes to work as a parallel plate capacitor, the capacitance obtained taking $l = 15 \pm 0.1$ cm as distance among the metal plates, $A = 1.5 \pm 0.2$ cm² as their area, $\epsilon_r = 25$ as relative dielectric constant of ferrofluid, according to the data provided by the NASA contractor report [?] for a FF with 2% vol of magnetite, and $\epsilon_0 = 8,854$ pF/m as vacuum dielectric constant, the value obtained for the capacitance is

$$C = \frac{\epsilon_0 \epsilon_r A}{l} = 0.2 \text{ pF}$$

which means that a further contribution to the capacitance is present and is probably represented by the titanium oxide TiO₂ layer formed on top of metal electrodes since the titanium is shown to oxidize very rapidly in air.

The influence of heat is now investigated by heating the ferrofluid at $T = 60^\circ\text{C}$ and then fluxing it into the pipe. The parameters of interest have been reported in Fig. 52 where once again it can be appreciated the noise at low frequencies. A filtering is again applied before the estimation of resistance and capacitance.

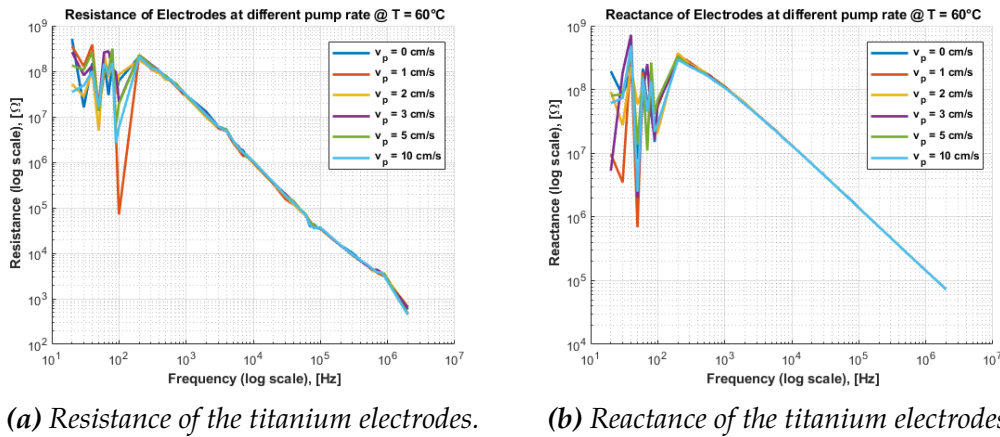
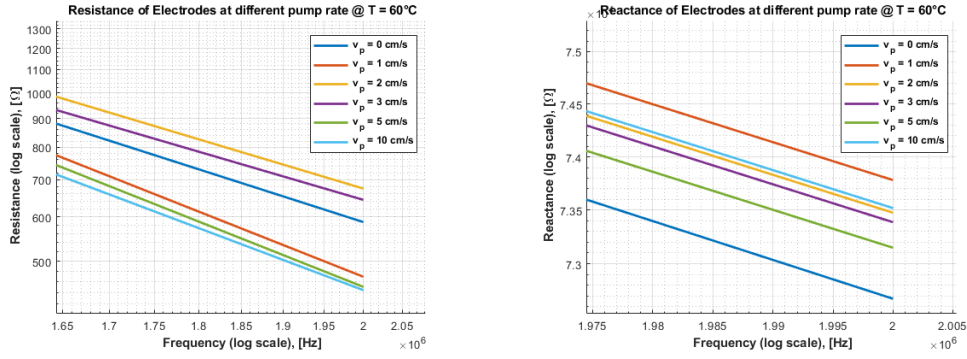


Figure 52: Bode plot of titanium electrodes, used for electrostatic charge recovery performed fluxing the fluid heated at $T = 60^\circ\text{C}$. The legend reports the pump rate velocity for each curve.

In Fig. 53 the magnified image are reported where it can be noticed immediately an overall increase in resistance²⁶ which is compatible with the theory. In fact, according to thermodynamics, once a metal is heated its resistance increases because of thermal agitation and an increase in phonon energy.

²⁶Remember that, as discussed in subsection 5.1 the resistance is negative even though it has been reported in dB scale which is by definition positive.



(a) Resistance of the titanium electrodes. (b) Reactance of the titanium electrodes.

Figure 53: Detail of Fig. 52. The image is zoomed in order to appreciate the differences among the curves obtained for different pump rates.

The decrease observed at $v_p = 5\text{cm/s}$ is probably linked to the thermal expansion suffered by the particles and the surfactants which cause an increase in their overall volume and consequently the drag force suffered is greater. A slight decrease in the capacitance is evident from the data reported in Tab. 11 which is compatible with the fact that the ferrofluids decrease their dielectric permittivity with temperature[93].

	$v_p = 1\text{cm/s}$	$v_p = 2\text{cm/s}$	$v_p = 3\text{cm/s}$	$v_p = 5\text{cm/s}$	$v_p = 10\text{cm/s}$
Resistance [MΩ]	91 ± 15	132 ± 19	166 ± 22	129 ± 16	101 ± 24
Capacitance [pF]	1.24 ± 0.06	1.24 ± 0.05	1.25 ± 0.06	1.26 ± 0.05	1.26 ± 0.07
Power Produced [nW]	11.0 ± 0.5	7.6 ± 0.5	6.0 ± 0.3	7.8 ± 0.4	9.9 ± 0.5

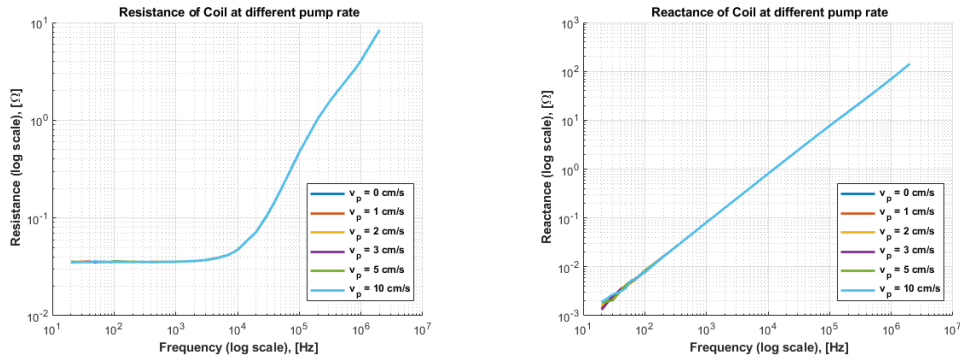
Table 11: Resistance and Capacitance at different flow rate velocities of the capacitive titanium electrodes. The measurements are performed fluxing the fluid at $T = 60^\circ\text{C}$

In Tab. 10 and 11 are also reported the overall power, computed applying the approach presented in subsection 5.1, in the two situations. It is evident that an overall increase in the efficiency has taken place once the ferrofluid has been heated. This is linked to the thermal agitation which provoke an easier hopping of charges increasing the transfer efficiency. Moreover, the electrical resistivity of the magnetite is shown to decrease with temperature[94] explaining the higher power produced in this frame.

Coil

The last component to analyse is the inductive coil of wire tightly wrapped onto the tube. It is composed by two layers of coils with $N/2 = 40$ windings each for a total length of $l = 14 \pm 0.1\text{ cm}$. Starting from the acquisition at room temperature, Fig.

54 has been obtained by reporting in a Bode plot the resistance and reactance as a function of frequency. The amplitude of the signal set on the LCR-meter during the acquisition is $V_{r.m.s} = 0.1$ V.

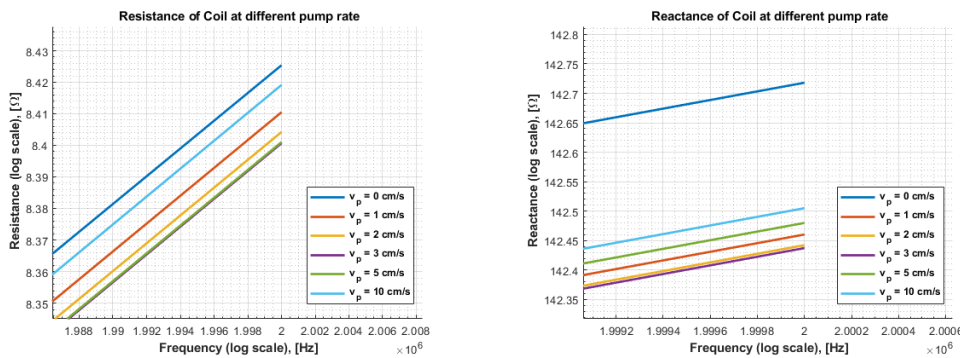


(a) Resistance of the coil plotted as a function of the frequency.

(b) Reactance of the coil plotted as a function of the frequency.

Figure 54: Bode plot of inductive coil of wire as a function of different flow velocity. The legend reports the pump rate for each curve.

The magnified Fig. 55 shows the difference in the curve trend at different flow velocities. In these graphs the curves acquired with no fluid motion is also reported showing how the motion affects the magnitude of these parameters.



(a) Resistance of the coil plotted as a function of the frequency.

(b) Reactance of the coil plotted as a function of the frequency.

Figure 55: Detail of Fig. 54. The image is zoomed in order to appreciate the differences among the curves obtained for different pump rates.

It can be noticed from the above figure that the same trend results from the flow rate increase. In fact, until the third velocity, a decrease in both the resistance and reactance occur as expected from the theory since the particle motion is creating a magnetic flux variation within the inductor. However, at $v_p = 5$ cm/s an increase occurs meaning that the energy harvesting is becoming less efficient. This trend can

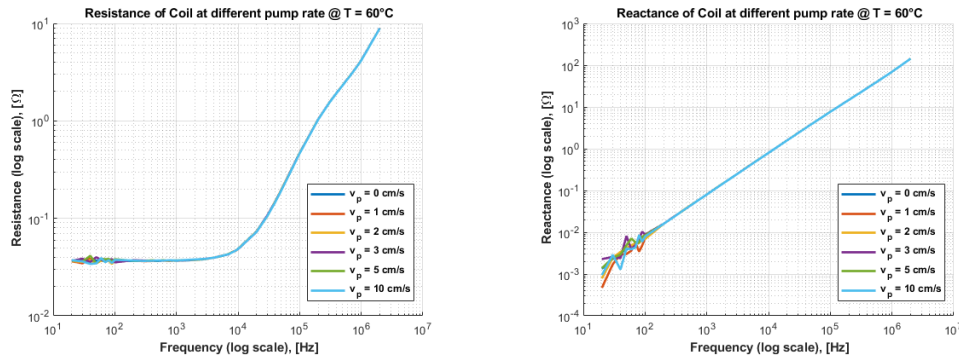
be linked to the observation mentioned in the electrodes analysis: when the speed of the particles increase above a certain threshold, a deceleration of the particles in contact with the pipe's wall occur. It can be due to a increase of drag force caused by the higher kinetic energy of the particles which allows them to fit into the roughness of the tube itself. This and the fact that the shallower layer is the one contributing mostly to electromotive force induced in the coil produces a diminishing of the overall power extracted. The results obtained from the previous graphs are reported in Tab. 12 where the output power, computing according to E.q 143, has been estimated. It has to be noticed that the power V_{rms} that has to be used is not the one set on the instrument but is the real voltage drop across the coil. For this reason the voltage divider rule needs to be applied and the real voltage V_r to be used during the estimation is

$$V_r = V_{rms} \frac{X_L}{X_L + R}$$

Flow Rate [cm/s]	$v_p = 0$	$v_p = 1$	$v_p = 2$	$v_p = 3$	$v_p = 5$	$v_p = 10$
Resistance [mΩ]	35.6 ± 0.2	35.5 ± 0.1	35.4 ± 0.1	35.4 ± 0.2	35.5 ± 0.1	35.5 ± 0.1
Inductance [μ H]	12.6 ± 0.6	12.6 ± 0.5	12.5 ± 0.5	12.5 ± 0.5	12.6 ± 0.5	12.6 ± 0.5
Power Produced [μ W]	-	70.38 ± 0.01	78.13 ± 0.01	75.05 ± 0.01	36.35 ± 0.01	61.37 ± 0.01

Table 12: Resistance and Capacitance at different flow rate velocities of the coil of wires. The measurements are performed fluxing the fluid at RT.

According to the approach followed so far, the fluid has been heated and all the measurements have been repeated. In Fig. 56 are reported once again the reactance and resistance followed by its magnification showing the overall trend of the different curves (see Fig. 57).



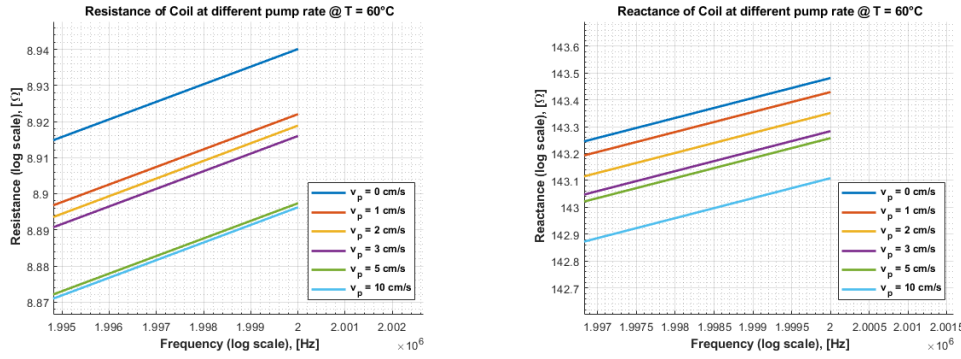
(a) Resistance of the coil plotted as a function of the frequency.

(b) Reactance of the coil plotted as a function of the frequency.

Figure 56: Bode plot of inductive coil of wire as a function of different flow velocity. The legend reports the pump rate for each curve.

Besides an overall increasing in the resistance, which suggest that the coil of wire has experienced the heating released by the fluid, it is interesting to notice that the proportionality between R or X and the flow rate is maintained at all the velocities. This can be due to two main contributions:

- The viscosity of the fluid is reduced because of the heating and the drag force developed onto the tube wall is consequently lower avoiding the nanoparticles trapping;
- Being the magnetization a function of the temperature, the heating provokes a reduction of its magnitude. This provokes a decrease in the magnetic force provoked by the external permanent magnets onto the particle and, consequently, it undergoes a smaller deceleration.



(a) Resistance of the coil plotted as a function of the frequency.

(b) Reactance of the coil plotted as a function of the frequency.

Figure 57: Detail of Fig. 56. The image is zoomed in order to appreciate the differences among the curves obtained for different pump rates when the fluid is heated up to $T = 60^\circ\text{C}$.

The data extracted from these graphs are summarized in Tab. 13.

Flow Rate [cm/s]	$v_p = 0$	$v_p = 1$	$v_p = 2$	$v_p = 3$	$v_p = 5$	$v_p = 10$
Resistance [$\text{m}\Omega$]	35.6 ± 0.1	37.0 ± 0.2	36.4 ± 0.2	37.0 ± 0.1	37.6 ± 0.2	37.8 ± 0.2
Inductance [μH]	12.5 ± 0.5	12.5 ± 0.5	12.5 ± 0.5	12.5 ± 0.5	12.4 ± 0.5	12.4 ± 0.5
Power Produced [mW]	-	0.25 ± 0.01	0.63 ± 0.02	0.92 ± 0.01	1.3 ± 0.3	1.9 ± 0.1

Table 13: Resistance and Capacitance at different flow rate velocities of the inductive coil. The measurements are performed fluxing the fluid at $T = 60^\circ\text{C}$

6 Conclusions

Climate change requires to find new way for clean energy production and also smart methods to limit the introduction of heat in atmosphere. Both the C.E.R.E.S. prototypes have been designed for this goal and in particular, to exploit low grade waste heat in order to produce useful energy by means of thermo-magnetic convection occurring in ferrofluid, a magnetic colloid composed by superparamagnetic nanoparticles (like magnetite). In previous works of thesis the idea was to use ferrofluid only to fill the reactor's chamber and thus recover energy only by means of electromotive force harvested using a coil. However, this is a limiting approach since it exploit only one method for electric energy production. For this reason, new element have been investigated in order to increase the harvesting efficiency of the system.

Among many different effects, pyroelectricity was chosen to be implemented because of its direct link with the thermal gradient applied to the system. Thus, a new colloidal mixture, formed by barium titanate nanoparticles at 0.5% vol and ferrofluid EFH3 at 2% vol, has been synthesized. To prove the effective contribution to current and voltage generation by means of BT, the experimental setup proposed in 4.5 has been created allowing the characterization of all the component of the mixture and the observation of an effective increase in the extracted power, as it can be noticed from the capacitive analysis. However, because of some problem of liquid losses, this apparatus needed to be rebuild almost every day thus the measurements performed in two different days were not comparable. To solve this issue, the cell proposed in subsection 4.1.3 has been designed. It will provide good sealing avoiding liquid losses and, consequently, the comparison among different magnets and thermal gradient combinations. Moreover, it will allow to perform visual observation of the thermo-magnetic motion and to introduce different powders in ferrofluid to observe the behaviour and find a mixture able to exploit also other physical effect, like triboelectricity, for energy recovery. Some future experiments, besides the steps proposed in section 5.2, will be:

- Analysis of pyroelectric effect using different methods, also dynamic or indirect, to confirm the results obtained here;
- Change the BT concentration to provide an analysis of the current/voltage produced with respect to its solid phase;
- Investigate the fluid profile during the motion thanks to the ultrasonic velocity profiler (UVP);
- Investigate the influence of the chamber thickness on the thermo-magnetic

motion thanks to the possibility to change the lateral frames;

- Investigate the influence of surface tension gradient, thanks to the wall dividing the chamber, on the magnetite distribution;

Moreover, barium titanate is one of the possible powder that can be used for pyroelectricity, thus different other materials needs to be tested also to analysed the interaction with magnetite and kerosene. Concerning this latter, the idea is to displace the attention toward water based ferrofluids in order to create a greener system which could be also used in wearable application.

References

- [1] Giuseppe Fortunato. *Thermofluidynamics of colloidal systems*. PhD thesis, 2019.
- [2] Fabio Mattiussi. *A Thermomagnetic Energy Harvester*. PhD thesis, 2018.
- [3] David C. Frank, Jan Esper, Christoph C. Raible, Ulf Büntgen, Valerie Trouet, Benjamin Stocker, and Fortunat Joos. Ensemble reconstruction constraints on the global carbon cycle sensitivity to climate. *Nature*, 463(7280):527–530, 2010.
- [4] Thomas R. Karl, Anthony Arguez, Boyin Huang, Jay H. Lawrimore, James R. McMahon, Matthew J. Menne, Thomas C. Peterson, Russell S. Vose, and Huai Min Zhang. Possible artifacts of data biases in the recent global surface warming hiatus. Technical Report 6242, 2015.
- [5] National Aeronautics and Space Administration, 2019.
- [6] National Oceanic and Atmospheric Administration (NOAA) Earth System Research Laboratory. Full record of CO₂ concentration, 2019.
- [7] FAO. *Agriculture and Climate Change - Challenges and Opportunities at the Global and Local Level - Collaboration on Climate-Smart Agriculture*. 2019.
- [8] Quinn E. Barber, Marc André Parisien, Ellen Whitman, Diana Stralberg, Chris J. Johnson, Martin Hugues St-Laurent, Evan R. DeLancey, David T. Price, Dominique Arseneault, Xianli Wang, and Mike D. Flannigan. Potential impacts of climate change on the habitat of boreal woodland caribou. *Ecosphere*, 9(10), 2018.
- [9] National Aeronautics and Space Administration Goddard Institute for Space Studies (GISS), 2019.
- [10] D. Ehhalt and M. Prather. Atmospheric Chemistry and Greenhouse Gases. *Climate Change 2001: The Scientific Basis*, pages 239–287, 2001.
- [11] J. T. Houghton, G. J. Jenkins, and J. J. Ephraums. *Climate change: the IPCC scientific assessment*. 1990.
- [12] Gunnar Myhre, Drew Shindell, Francois-Marie Bréon, and William Collins. Anthropogenic and natural radiative forcing. *Climate Change 2013 the Physical Science Basis: Working Group I Contribution to the Fifth Assessment Report of the Intergovernmental Panel on Climate Change*, pages 659–740, 2013.

REFERENCES

- [13] Graeme L Stephens and Stephen A Tjemkes. Water Vapour and Its Role in the Earth's Greenhouse. *Australian Journal of Physics*, 46(1):149, 1993.
- [14] National Climatic Data Center, 2019.
- [15] C. D. Keeling. Climate change and carbon dioxide: An introduction. *Proceedings of the National Academy of Sciences of the United States of America*, 94(16):8273–8274, 1997.
- [16] Hervé Le Treut, Ulrich Cubasch, and Myles Allen. Historical Overview of Climate Change Science. *Notes*, 16, 2005.
- [17] United States Environmental Protection Agency, 2019.
- [18] Olivier Juvyns, Ricardo Fernandez, Elisabeth Rigler, and Mandl Nicole. Annual European Union greenhouse gas inventory 1990–2017 and inventory report 2019. Technical Report 6, 2019.
- [19] National Oceanic and Atmospheric Administration (NOAA), 2019.
- [20] Rajendra K. Pachauri, Leo Meyer, Vicente R. Barros, and Qin Dahe (China) Broome, John, Wolfgang Cramer (Germany/France), Renate Christ (Austria/WMO), John A. Church (Australia), Leon Clarke (USA). Topotactical growth of indium sulfide by evaporation of metal onto molybdenite. Technical Report 2, 2015.
- [21] Michael M. Watkins, David N. Wiese, Dah Ning Yuan, Carmen Boening, and Felix W. Landerer. Improved methods for observing Earth's time variable mass distribution with GRACE using spherical cap mascons. *Journal of Geophysical Research: Solid Earth*, 120(4):2648–2671, 2015.
- [22] B. D. Beckley, P. S. Callahan, D. W. Hancock, G. T. Mitchum, and R. D. Ray. On the “Cal-Mode” Correction to TOPEX Satellite Altimetry and Its Effect on the Global Mean Sea Level Time Series. *Journal of Geophysical Research: Oceans*, 122(11):8371–8384, 2017.
- [23] International Energy Agency. 2018 World Energy Outlook: Executive Summary. *Oecd/Iea*, page 11, 2018.
- [24] Energy Information Administration. International Energy Outlook. *Outlook*, 0484(July):70–99, 2019.
- [25] U.S. Energy Information Administration, 2019.

- [26] Vaclav Smil. *Energy Transitions - History, Requirements, Prospects*. PRAEGER - An Imprint of ABC-CLIO, LLC, 1 edition, 2010.
- [27] Global Energy Statistical Yearbook Enerdata, 2019.
- [28] Ilona Johnson, William T. Choate, and Amber Davidson. Waste Heat Recovery: Technology Opportunities in the US Industry. *US Department of Energy - Industrial Technologies Program*, pages 1–112, 2008.
- [29] Zhiwei Ma Janie Ling-Chin, Huashan Bao, Zhiwei Ma Janie Ling-Chin, Huashan Bao, Wendy Taylor Roskilly, and Anthony Paul. State-of-the-Art Technologies on Low-Grade Heat Recovery and Utilization in Industry. *IntechOpen*, pages 57–74, 2018.
- [30] Vladimir Leonov, Tom Torfs, Paolo Fiorini, and Chris Van Hoof. Thermoelectric converters of human warmth for self-powered wireless sensor nodes. *IEEE Sensors Journal*, 7(5):650–656, 2007.
- [31] Vladimir Leonov. Simulation of maximum power in the wearable thermoelectric generator with a small thermopile. *Microsystem Technologies*, 17(4):495–504, 2011.
- [32] Vladimir Leonov. Thermoelectric energy harvesting of human body heat for wearable sensors. *IEEE Sensors Journal*, 13(6):2284–2291, 2013.
- [33] Tom Torfs, Vladimir Leonov, and Ruud J.M. Vullers. Pulse Oximeter Fully Powered by Human Body Heat. *Sensors & Transducers Journal*, 80(6):1230 – 1238, 2007.
- [34] Ashkan Entezari, Ali Manizadeh, and Rouhollah Ahmadi. Energetical, exergetical and economical optimization analysis of combined power generation system of gas turbine and Stirling engine. *Energy Conversion and Management*, 159(January):189–203, 2018.
- [35] Mingyu Hou, Zhanghua Wu, Guoyao Yu, Jianying Hu, and Ercang Luo. A thermoacoustic Stirling electrical generator for cold exergy recovery of liquefied nature gas. *Applied Energy*, 226(May):389–396, 2018.
- [36] A. H. Bademlioglu, A. S. Canbolat, N. Yamankaradeniz, and O. Kaynakli. Investigation of parameters affecting Organic Rankine Cycle efficiency by using Taguchi and ANOVA methods. *Applied Thermal Engineering*, 145:221–228, 2018.
- [37] Alessandro Chiolerio and Marco B. Quadrelli. Colloidal Energetic Systems. *Energy Technology*, 7(5), 2019.

- [38] S S Papell. Low viscosity magnetic fluid obtained by the colloidal suspension of magnetic particles, 1965.
- [39] Stefan Odenbach. Ferrofluids- Magnetisable Liquids and Their Application in Density Separation. *Magnetic and Electrical Separation*, 9:1–25, 1998.
- [40] Ferrotec Company, 2019.
- [41] K. Büscher, C. A. Helm, C. Gross, G. Glöckl, E. Romanus, and W. Weitschies. Nanoparticle Composition of a Ferrofluid and Its Effects on the Magnetic Properties. *Langmuir*, 20(6):2435–2444, 2004.
- [42] Alexey O. Ivanov and Valentin S. Mendeleev. Ferrofluid aggregation in chains under the influence of a magnetic field. *Journal of Magnetism and Magnetic Materials - Elsevier*, (5):10, 2005.
- [43] A. F. Pshenichnikov, V. V. Mekhonoshin, and A. V. Lebedev. Magneto-granulometric analysis of concentrated ferrocolloids. *Journal of Magnetism and Magnetic Materials*, 161:94–102, 1996.
- [44] Herbert B. Callen. *Thermodynamics And An Introduction To Thermostatistics*. John Wiley & Sons, 1985.
- [45] B. A. Finlayson. Convective instability of ferromagnetic fluids. *Journal of Fluid Mechanics*, 40:753–767, 1970.
- [46] Jean K. Platten. The Soret effect: A review of recent experimental results. *Journal of Applied Mechanics, Transactions ASME*, 73(1):5–15, 2006.
- [47] Antônio M. Figueiredo Neto and Silvio R.A. Salinas. *The Physics of Lyotropic Liquid Crystals: Phase Transitions and Structural Properties*, volume 9780198525. 2010.
- [48] Yuki Kishikawa, Simone Wiegand, and Rio Kita. Temperature dependence of soret coefficient in aqueous and nonaqueous solutions of pullulan. *Biomacromolecules*, 11(3):740–747, 2010.
- [49] E. Bringuier and A. Bourdon. Colloid transport in nonuniform temperature. *Physical Review E - Statistical Physics, Plasmas, Fluids, and Related Interdisciplinary Topics*, 67(1):6, 2003.
- [50] Sidney B. Lang. *Sourcebook of pyroelectricity*. Routledge, 1974.
- [51] Louis Carlioz, Jérôme Delamare, Skandar BASROUR, and Guylaine Poulin-Vittrant. Hybridization of magnetism and piezoelectricity for an energy scavenger based on temporal variation of temperature. pages 311 – 313, 05 2008.

- [52] M R SRINIVASAN. Pyroelectric materials. *Bulletin of Material Science*, 6(2):317–325, 1984.
- [53] S. Jachalke, E. Mehner, H. Stöcker, J. Hanzig, M. Sonntag, T. Weigel, T. Leisegang, and D. C. Meyer. How to measure the pyroelectric coefficient. *Applied Physics Reviews*, 4(2), 2017.
- [54] Nicola A. Spaldin. *Magnetic Materials: Fundamentals and Applications*, volume 1. Cambridge University Press, 2010.
- [55] Alexey O. Ivanov, Sofia S. Kantorovich, Evgeniy N. Reznikov, Christian Holm, Alexander F. Pshenichnikov, Alexander V. Lebedev, Alexandros Chremos, and Philip J. Camp. Magnetic properties of polydisperse ferrofluids: A critical comparison between experiment, theory, and computer simulation. *Physical Review E - Statistical, Nonlinear, and Soft Matter Physics*, 75(6):1–12, 2007.
- [56] Aleksandra A Bozhko and Sergey A Suslov. *Convection in Experiments and Theory*.
- [57] Alexey O. Ivanov and Olga B. Kuznetsova. Magnetic properties of dense ferrofluids: An influence of interparticle correlations. *Physical Review E - Statistical Physics, Plasmas, Fluids, and Related Interdisciplinary Topics*, 64(4):12, 2001.
- [58] Stefan Odenbach and Mario Liu. Invalidation of the Kelvin force in ferrofluids. *Physical Review Letters*, 86(2):328–331, 2001.
- [59] Thermomagnetic convection in a vertical layer of ferromagnetic fluid. *Physics of Fluids*, 20(8), 2008.
- [60] Stefan Odenbach. *Magnetoviscous Effects in Ferrofluids*, volume 781. Springer, 2002.
- [61] John G. Webster, Maciej Zborowski, and Jeffrey J. Chalmers. Magnetophoresis: Fundamentals and Applications. *Wiley Encyclopedia of Electrical and Electronics Engineering*, pages 1–23, 2015.
- [62] V. M. Buzmakov and A. F. Pshenichnikov. On the structure of microaggregates in magnetite colloids. *Journal of Colloid and Interface Science*, 182(1):63–70, 1996.
- [63] A. F. Pshenichnikov and A. S. Ivanov. Magnetophoresis of particles and aggregates in concentrated magnetic fluids. *Physical Review E - Statistical, Nonlinear, and Soft Matter Physics*, 86(5):1–11, 2012.
- [64] A. S. Ivanov and A. F. Pshenichnikov. Dynamics of magnetophoresis in dilute magnetic fluids. *Physics Procedia*, 9:96–100, 2010.

- [65] Alexander F. Pshenichnikov, Ekaterina A. Elfimova, and Alexey O. Ivanov. Magnetophoresis, sedimentation, and diffusion of particles in concentrated magnetic fluids. *Journal of Chemical Physics*, 134(18), 2011.
- [66] Bertrand Faure, German Salazar-Alvarez, and Lennart Bergström. Hamaker constants of iron oxide nanoparticles. *Langmuir*, 27(14):8659–8664, 2011.
- [67] Anwar Gavili, Fatemeh Zabihi, Taghi Dallali Isfahani, and Jamshid Sabbaghzadeh. The thermal conductivity of water base ferrofluids under magnetic field. *Experimental Thermal and Fluid Science*, 41:94–98, 2012.
- [68] Carlo Marangoni. Sul principio della viscosita' superficiale dei liquidi stabilito dal sig. J. Plateau. *Il Nuovo Cimento Series 2*, 5-6(1):239–273, 1871.
- [69] S. D. Kemkar, Milind Vaidya, Dipak Pinjari, Chandrakant Holkar, Sanjana Kemkar, Siddhesh Nanaware, and Sanjukta Kemkar. Energy Conversion on Differential Magnetization of Fe₃O₄ Ferrofluid. *International Journal of Engineering Research and Applications*, 7(1):01–10, 2017.
- [70] Francisco J. Arias and Salvador A. De Las Heras. Ferrohydrodynamic capillary convection. *Journal of Thermal Science and Engineering Applications*, 11(2), 2019.
- [71] A. I. Fedosov. THERMOCAPILLARY MOTION. *Zhurnal Fizicheskoi Khimii* 30 (1956), 30:366–373, 2013.
- [72] Myoungwoo Lee and Youn Jea Kim. Thermomagnetic convection of ferrofluid in an enclosure channel with an internal magnetic field. *MDPI: micromachines*, 10(9):2–9, 2019.
- [73] Habibur Rahman and Sergey A. Suslov. Thermomagnetic convection in a layer of ferrofluid placed in a uniform oblique external magnetic field. *Journal of Fluid Mechanics*, 764:316–348, 2015.
- [74] Clayton T. Crowe, John D. Schwarkopf, Martin Sommerfeld, and Yutaka Tsuji. *Multiphase Flows with Droplets and Particles*. 2009.
- [75] Jie-Zhi Wu, Ye Zhou, and Jian-Ming Wu. Reduced Stress Tensor And Dissipation And the Transport of Lamb Vector. *Langley Research Center - Institute for Computer Applications in Science and Engeneering*, 1996.
- [76] C.M.Tchen. *Mean value and correlation problems connected with the motion of small particles suspended in a turbulent fluid*. PhD thesis, Delft, 1947.
- [77] Adrian Stoica, Michel D. Ingham, Leslie Tamppari, Karl Mitchell, and Marco B. Quadrelli. Transformers for Extreme Environments. (May):72, 2014.

- [78] H. T. Langhammer, T. Müller, T. Walther, R. Böttcher, D. Hesse, E. Pippel, and S. G. Ebbinghaus. Ferromagnetic properties of barium titanate ceramics doped with cobalt, iron, and nickel. *Journal of Materials Science*, 51(23):10429–10441, 2016.
- [79] Essam Hussein and Khalid Khairou. Cheminform abstract: Sonochemistry: Synthesis of bioactive heterocycles. *Synthetic Communications*, 44, 07 2014.
- [80] Tahsin Onur Dizdar, Gizem Kocausta, Ergin Gülcan, and Özcan Y. Gülsoy. A new method to produce high voltage static electric load for electrostatic separation – Triboelectric charging. *Powder Technology, Elsevier*, 327:89–95, 2018.
- [81] US Research Nanomaterial Inc., 2019.
- [82] E.J. Abbott and F.A. Firestone. Specifying Surface Quality—A Method on Accurate Measurement and Comparison. *Mechanical Engineering ASME*, 55:569–572, 1933.
- [83] J.A. Greenwood and J.H. Tripp. THE CONTACT OF TWO NOMINALLY FLAT ROUGH SURFACES. *Proc Instn Mech Engrs*, 185:48–71, 1981.
- [84] Inframath Advanced Materials, 2019.
- [85] S. S. Wadwalkar, R. L. Jackson, and L. Kogut. A study of the elastic-plastic deformation of heavily deformed spherical contacts. *Journal of Engineering Tribology*, 224(10):1091–1102, 2010, and therein references.
- [86] Robert L. Jackson and Itzhak Green. A finite element study of elasto-plastic hemispherical contact against a rigid flat. *Journal of Tribology*, 127(2):343–354, 2005.
- [87] Hamed Ghaednia and Robert L. Jackson. The effect of nanoparticles on the real area of contact, friction, and wear. *Journal of Tribology*, 135(4):1–10, 2013.
- [88] Tomasz Trzepiecinski and Magdalena Gromada. Characterization of mechanical properties of barium titanate ceramics with different grain sizes. *Materials Science- Poland*, 36(1):151–156, 2018.
- [89] B. L. Cheng, M. Gabbay, W. Duffy, and G. Fantozzi. Mechanical loss and Young’s modulus associated with phase transitions in barium titanate based ceramics. *Journal of Materials Science*, 31(18):4951–4955, 1996.
- [90] Burcu Ertuğ. The Overview of The Electrical Properties of Barium Titanate. *American Journal of Engineering Research*, 2(08):1–7, 2013.

REFERENCES

- [91] T. Fujita and I. J. Lin. Dielectric fluid preparation by dispersing ultrafine barium titanate particles in kerosene. *Powder Technology*, 68(3):235–242, 1991.
- [92] Delia J Milliron, A Paul Alivisatos, Claire Pitois, Carine Edder, and Jean M J Fréchet. Electroactive surfactant designed to mediate. *Advanced Materials*, 15(1):58–61, 2003.
- [93] Puja Goel, Gautam Singh, Rajendra P. Pant, and Ashok M. Biradar. Investigation of dielectric behaviour in ferrofluid-ferroelectric liquid crystal nanocomposites. *Liquid Crystals*, 39(8):927–932, 2012.
- [94] Vladimir V. Shchennikov and Sergey V. Ovsyannikov. Is the Verwey transition in Fe₃O₄ magnetite driven by a Peierls distortion? *Journal of Physics Condensed Matter*, 21(27):2–6, 2009.